

Contents

1	Introduction	2
1.1	Background	3
1.2	Scaling	4
1.2.1	Elastic Scattering	4
1.3	Inelastic Scattering	9
1.3.1	Resonances	13
1.3.2	EMC Effect	14
1.3.3	Quasielastic Scattering	17
1.4	Experiment E02-019	20
2	Theoretical Overview	23
2.1	Quasi-elastic Cross Section	23
2.1.1	y-scaling	32
2.1.2	Other Scaling functions - Superscaling	39
2.1.3	Other Scaling variables - y_{cw}	42

2.2	Inelastic Cross section	44
2.2.1	ξ -scaling	46
2.2.2	Final State Interactions	49
2.2.3	Short Range Correlations	52
3	Experimental Details	54
3.1	Overview	54
3.2	Accelerator	55
3.3	Hall C Beamline	56
3.3.1	Beam Energy Measurement	56
3.3.2	Beam Position Monitors	58
3.3.3	Beam Current Monitors	60
3.3.4	Beam Raster System	64
3.4	Targets	65
3.4.1	Cryogenic Targets	66
3.5	High Momentum Spectrometer	73
3.6	Detector Package	76
3.6.1	Drift Chambers	76
3.6.2	Drift Chamber Calibration	79
3.6.3	Hodoscopes	81
3.6.4	Gas Čerenkov	83
3.6.5	Lead Glass Calorimeter	84

3.7 Trigger	89
3.7.1 Data Acquisition System	92
4 Data Analysis	95
4.1 Spectrometer Optics/Coordinates	96
4.2 Event Reconstruction	97
4.3 Particle Identification and Electron Selection	100
4.3.1 Charge Symmetric Background	102
4.3.2 Pion Contamination	105
4.3.3 Cryogenic Target Aluminum Cell	108
4.3.4 Boiling of the Cryogenic Targets	110
4.4 Extracting Cross Sections	115
4.4.1 Approaches to obtaining σ	115
4.4.2 Obtaining Yields	117
4.4.3 Electronic Dead Time	119
4.4.4 Computer Dead Time	121
4.4.5 Trigger Efficiency	121
4.4.6 Tracking Efficiency	124
4.4.7 Detector Cut efficiencies	125
4.4.8 Energy Loss Corrections	126
4.4.9 Monte Carlo Yield	128
4.4.10 Bin-Centering	133

4.4.11 Radiative Corrections	135
4.4.12 Corrected Cross Section	138
4.4.13 Coulomb Corrections	139
4.4.14 Cross Section Model	142
5 Results	146
5.1 Cross Sections	146
5.2 $F(y, \mathbf{q})$ Scaling Function	150
5.3 Superscaling	158
5.4 Other Scaling Variables - y_{cw}	161
5.5 Short Range Correlations - Ratios	163
5.6 Inelastic Response	167
5.7 A-dependence of F_2	175
5.8 Systematic Uncertainties	179
5.8.1 Kinematic Uncertainties	179
6 Conclusion and Outlook	182

List of Figures

1.1	$\mu_p G_E/G_M$ vs Q^2 , world data.	9
1.2	F_2^p as a function of Q^2	11
1.3	Nucleon Resonances	13
1.4	νW_2^A data compared to the scaling curve.	15
1.5	The EMC Effect in Fe, Cu.	16
1.6	Spectral Function for Be.	19
1.7	Inclusive Deuterium Cross section	20
1.8	Kinematic coverage for JLab experiment E02-019.	21
2.1	Diagram of the quasielastic reaction	24
2.2	$F(\mathbf{q} , y)$ region of integration for ^{12}C	30
2.3	Theoretical calculation for the ^3He spectral function.	31
2.4	$F(y, \mathbf{q})$ for ^2H and ^{12}C from Jlab experiment E89-008.	33
2.5	Approach to scaling for ^{12}C	35
2.6	$F(\mathbf{q} , y)$ as a function of $1/q$ for ^{12}C	36

2.7 Momentum Distribution for ^3He , extracted from the asymptotic limit of $F(\mathbf{q} , y)$	37
2.8 Transverse component of the superscaling function, f_T	41
2.9 $F(\mathbf{q} , y)$ as a function of y_{cw} for several targets.	43
2.10 F_2 vs ξ for H, ^2H , and ^{56}Fe along with the MRST fit.	48
2.11 Relative contributions to F_2 for ^{197}Au as a function of ξ	49
2.12 Ratios of ^4He , ^{12}C , and ^{56}Fe to ^3He	51
3.1 Overhead Schematic of the Accelerator and the experimental halls . .	56
3.2 Hall C Beamline and Hardware. See text for details.	57
3.3 Sieve Slit Pattern.	60
3.4 BCM Calibration Run.	61
3.5 BCM Calibration Residuals	63
3.6 Beam Profile with the fast raster turned on.	64
3.7 Hall C Target ladder.	66
3.8 Cryogenic Target	68
3.9 Beam Offset.	71
3.10 Pressure, Temperature, and density for each ^3He run.	72
3.11 HMS: Side view.	74
3.12 HMS Collimators: Sieve and Pion	76
3.13 HMS Detector Stack.	77
3.14 HMS Drift Chamber.	78

3.15	Drift time and drift distance Spectra.	80
3.16	ADC spectra for the HMS Čerenkov PMTs	85
3.17	Typical Spectrum of the HMS Čerenkov.	85
3.18	Shifts in HMS shower counter spectrum.	88
3.19	HMS shower counter spectrum.	89
3.20	HMS single arm electronics	91
3.21	Schematic of Hall C data acquisition system	94
4.1	Target Coordinate system.	97
4.2	Typical “hourglass” distribution of electrons in the HMS.	98
4.3	Charge symmetric background for all targets at 40 °.	103
4.4	Size of the charge symmetric background for copper.	106
4.5	Pion Contamination in the HMS.	107
4.6	Relative contribution from Al end-cap to the cryotarget cross section.	109
4.7	External Radiative correction from end-caps of the cryogenic target.	111
4.8	Yields from the fourth luminosity scan.	112
4.9	Carbon yield for the fourth luminosity scan, corrected for BCM offset.	113
4.10	^3He yield for the third luminosity scan, corrected for BCM offset.	114
4.11	’SCIN’ efficiency in the S2Y HMS plane.	122
4.12	HMS Tracking Efficiency.	124
4.13	HMS Čerenkov efficiency.	127
4.14	HMS Acceptance.	132

4.15 Data/MC vs. δ	133
4.16 Systematic uncertainty due to BC model.	134
4.17 Radiative Processes.	135
4.18 Radiative Corrections for ^2H and ^{197}Au	137
4.19 Data and MC yields for Carbon, 40° , $p_{HMS}=1.14 \text{ GeV}/c$	139
4.20 Coulomb Corrections at 18°	142
4.21 Data and model cross sections for ^2H , ^{12}C , and ^{197}Au at 18° and 32° . . .	145
5.1 ^2H and ^3He cross sections: experimental results and Born model. . . .	147
5.2 ^4He and ^{12}C cross sections: experimental results and Born model. . . .	148
5.3 ^{63}Cu and ^{197}Au cross sections: experimental results and Born model. . . .	148
5.4 Carbon cross section at $\theta_{HMS} = 32^\circ$, data and theory calculation. . . .	150
5.5 $F(y, q)$ for deuterium, model and experiment.	151
5.6 ^2H and ^3He scaling functions: experimental result and fit.	152
5.7 ^4He and ^{12}C scaling functions: experimental result and fit.	153
5.8 ^{63}Cu and ^{197}Au scaling functions: experimental result and fit.	154
5.9 Approach to scaling for ^{12}C as a function of Q^2	155
5.10 Approach to scaling for ^2H as a function of Q^2	156
5.11 Approach to scaling for ^{12}C as a function of $1/q$	157
5.12 Superscaling function $f(\psi')$ for $A > 3$	158
5.13 $F(\mathbf{q} , y)$ and $f(\psi')$ for $A > 3$ at 18°	159
5.14 $F(\mathbf{q} , y)$ and $f(\psi')$ for $A > 3$ at 40°	160

5.15 $F(y, \mathbf{q})$ for ^2H and ^4He as a function of y , y_{cw} : data and a theoretical calculation.	162
5.16 $F(y, \mathbf{q})$ for ^{12}C as a function of y , y_{cw} : data and a theoretical calculation.	162
5.17 Cross section ratios of ^{12}C (right) and ^{63}Cu (left) to ^2H	164
5.18 Cross section ratios of ^{12}C (right) and ^{63}Cu (left) to ^3He	165
5.19 Cross section ratios of ^{12}C (right) and ^{63}Cu (left) to ^4He	165
5.20 F_2 structure function for ^2H and ^3He as a function of x	168
5.21 F_2 structure function for ^{12}C and ^{197}Au as a function of x	168
5.22 Q^2 behavior of the F_2 structure function for ^4He at fixed x	169
5.23 Q^2 behavior of the F_2 structure function for ^{12}C at fixed x	170
5.24 Kinematic coverage in W^2	171
5.25 F_2 structure function for ^2H and ^3He as a function of ξ	172
5.26 F_2 structure function for ^{12}C and ^{197}Au as a function of ξ	172
5.27 Q^2 behavior of the F_2 structure function for ^4He at fixed ξ	173
5.28 Q^2 behavior of the F_2 structure function for ^{12}C at fixed ξ	174
5.29 F_2 structure function for $A > 3$ as a function of ξ	177
5.30 A -dependence of the F_2 structure function for fixed ξ and θ_{HMS}	178

Inclusive electron scattering from nuclei at $x > 1$

and high Q^2 with a 5.75 GeV beam

Nadia Fomin

December 11, 2008

Abstract

Experiment E02-019, performed in Hall C at the Thomas Jefferson National Accelerator Facility (TJNAF), was a measurement of inclusive electron cross sections for several nuclei (^2H , ^3He , ^4He , ^9Be , ^{12}C , ^{63}Cu , and ^{197}Au) in the quasielastic region at high momentum transfer.

In the region of low energy transfer, the cross sections were analyzed in terms of the reduced response, $F(y)$, by examining its y -scaling behavior. The data were also examined in terms of the nuclear structure function νW_2^A and its behavior in x and the Nachtmann variable ξ . The data show approximate scaling of νW_2^A in ξ for all targets at all kinematics, unlike scaling in x , which is confined to the DIS regime. However, y -scaling observations are limited to the kinematic region dominated by the quasielastic response ($y < 0$), where some scaling violations arising from FSIs are observed.

Chapter 1

Introduction

The first scattering experiments were performed by Hans Geiger (1882-1945) and Ernest Marsden (1889-1970), under the guidance of Ernest Rutherford (1871-1937) and serve as the foundation for the nuclear model of the atom [1]. These experiments verified that the nuclear charge is a multiple of e , the electron charge, specifically, Ze and that it is concentrated near the center of the atom. This was determined by observing the angular distribution of the scattered particles.

Experimental technology has advanced greatly since Rutherford's time, but the principles behind the experiments are still the same: particles are scattered off a target, detected after the interaction and their energy and scattering angle are measured.

1.1 Background

Quantum Electrodynamics (QED) is the theory that describes the interaction between charged particles via the exchange of photons. It has been very successful in making accurate predictions of many quantities such as the anomalous magnetic moment of the electron. The interaction of the electron with the charge of the nucleus is well understood in QED, which along with the fact that it's a weak probe and does not disturb the target, makes the electron ideal for studying nuclear structure. This was first understood more than 50 years ago when electron scattering experiments from nuclear targets were performed by Lyman [2].

The nucleus receives energy ν and momentum \mathbf{q} from the electron through the exchange of a single virtual photon. The resolution of the electron probe is determined by the wavelength of the virtual photon, $\lambda = \frac{h}{\sqrt{Q^2}}$, which is in turn of a function of the 4-momentum transfer, Q^2 . The larger wavelengths, given by the lower values of Q^2 , probe the bulk properties of the nucleus and give us information about its structure. Increasing Q^2 and decreasing the wavelength of the probe allows for study of the nucleons inside the nucleus. As the Q^2 is increased further, the resolution becomes finer, and we are able to probe the fundamental building blocks of matter, i.e. quarks.

1.2 Scaling

Scaling refers to the regime where the measured cross-section becomes independent of Q^2 and ν , the traditional variables, and can instead be expressed as a function of just one kinematic variable, which is itself a function of Q^2 and ν . The appeal of the scaling approach lies in the fact that when we observe scaling, it usually means that a simple reaction mechanism dominates the process and structural information can be extracted in a model-independent way [3]. In different kinematic regimes (deep inelastic, quasi-elastic), scaling in different variables is observed and reflects the different dominant processes.

1.2.1 Elastic Scattering

In Rutherford's experiment alpha particles were scattered elastically by the Coulomb field of a gold nucleus. For this case, a quantum mechanical formulation of the cross section yields the same result as a classical one. Treating this cross section in the Born approximation (ingoing and outgoing particle is each described by a plane wave), Rutherford's scattering formula is given by:

$$\left(\frac{d\sigma}{d\Omega} \right)_R = \frac{4m^2(Z_1Ze^2)^2}{q^4} \quad (1.1)$$

where Z_1e and m are the charge and mass of the incoming particle, Ze is that of the nucleus, and q^4 is the 4th power of the 3-momentum transfer, \mathbf{q} . In this formula,

the incoming and target particles are both taken to be structureless objects of spin 0. Additionally, the target is treated as being infinitely massive and does not recoil.

However, in the case of electron scattering, its spin has to be taken into account and the cross section expression is modified to give:

$$\left(\frac{d\sigma}{d\Omega} \right)_{Mott} = 4(Ze^2)^2 \frac{E^2}{q^4} (1 - \beta^2 \sin^2(\theta/2)), \quad (1.2)$$

where E, β are the energy and velocity (fraction of c) of the incident electron. This expression is known as the Mott cross section. So far, the recoil motion of the target has been ignored with the assumption that the target is very massive and therefore the recoil will be negligible. To properly account for this recoil motion, the Mott cross section is corrected by $1/(1 + 2E/M \sin^2(\theta/2))$.

The Mott cross section needs to be further modified when the target is an extended object (has internal structure). This is done through the use of *form factors*, which depend on the square of the momentum transfer, and modify the cross section:

$$\frac{d\sigma}{d\Omega} = \left(\frac{d\sigma}{d\Omega} \right)_{Mott}^R |F(\mathbf{q}^2)|^2, \quad (1.3)$$

where the superscript R refers to the recoil factor in the Mott cross section. Eq. 1.3 shows that the form factor can be determined experimentally by measuring the cross section at any scattering angle and dividing by the Mott cross section at the same kinematics. To relate it to theoretical calculations, the nuclear form factor can be

written down as the Fourier transform of the probability density. For a spin 0 target, the form factor in Eq. 1.3 describes the distribution of electric charge. Elastic electron scattering has been used to accurately map out the nuclear charge distribution of many nuclei [4]. If the target has spin 1/2 (for example, a nucleon), then an additional factor is needed to describe the distribution of the magnetization over the target volume.

In the case of a nucleon, incorporating both distributions into the cross section, yields the following expression, referred to as the *Rosenbluth* cross section:

$$\frac{d\sigma^{(p,n)}}{d\Omega} = \left(\frac{d\sigma}{d\Omega} \right)_{Mott} \left[\frac{G_{E(p,n)}^2 + \tau G_{M(p,n)}^2}{1 + \tau} + 2\tau G_{M(p,n)}^2 \tan^2(\theta/2) \right] \quad (1.4)$$

with $\tau = Q^2/4m^2$ and G_E and G_M being the electric and magnetic form factors, which depend only on Q^2 . Note that we have adopted the relativistic definition of 4-momentum transfer, where $Q^2 = 4EE' \sin^2(\theta/2)$. The electron and magnetic form factors are named as such because in the limit of $Q^2 = 0$, they take on the values of q_N/e (charge) and μ/μ_N (magnetic moment) for G_E and G_M , respectively, with e being the positive unit of charge and μ_N the nuclear magneton.

One can see from Eq. 1.4 that the form factors can be separated by performing scattering experiments at fixed Q^2 and different scattering angles. This is known as Rosenbluth separation.

The so-called “dipole” fit, given by

$$G_D(Q^2) = \frac{1}{1 + Q^2/0.71} \quad (1.5)$$

describes the separated form factors well and arises from an exponential charge distribution. The other form factors, G_E^n , G_M^p , G_M^n , can be expressed in terms of it for a reasonable approximation:

$$\begin{aligned} G_E^p(q^2) &\approx \frac{G_M^p(q^2)}{(\mu_p/\mu_N)} \approx \frac{G_M^n(q^2)}{(\mu_n/\mu_N)} = G_D(Q^2) \\ G_E^n &= -\frac{\mu_N}{1 + 5.6\tau} G_E^p \end{aligned} \quad (1.6)$$

The electric form factor of the neutron, G_E^n , given in Eq. 1.6 follows a modified dipole behavior, due to Galster [5]. Of the 4 form factors, G_E^n has been the most difficult to measure as no free neutron targets exist and the form factor is very small.

There are two experimental methods used to separate the elastic form factors: polarization transfer and Rosenbluth separation. The latter method involves measuring the cross section at several values of beam energy and scattering angles for a constant Q^2 . The information about form factors can then be extracted from the reduced cross section via:

$$\left(\frac{d\sigma}{d\Omega} \right)_{reduced} = \frac{\epsilon(1 + \tau)}{\tau} \left(\frac{d\sigma}{d\Omega} \right)_{exp} / \left(\frac{d\sigma}{d\Omega} \right)_{Mott} = G_M^2 + \frac{\epsilon}{\tau} G_E^2, \quad (1.7)$$

where $\epsilon = (1 + 2(1 + \tau) \tan^2 \theta/2)^{-1}$ is the polarization of the virtual photon. G_E and G_M are obtained from the slope and intercept when the Eq. 1.7 is fit for a range of ϵ values for a given Q^2 . The linear dependence of the reduced cross section on ϵ is a direct consequence of the one-photon approximation.

The polarization transfer method involves scattering longitudinally polarized electrons and measuring the polarization of the recoil proton, which will have two non-zero polarization components, P_z (from G_M) and P_x (from the G_M and G_E interference term). The ratio of the form factors then gives [6]:

$$\frac{G_E}{G_M} = -\frac{P_x}{P_z} \frac{E + E'}{2M} \tan\left(\frac{\theta}{2}\right) \quad (1.8)$$

where E , E' , and θ refer to the energy of the beam and the energy and angle of the scattered electron.

Results from experiments using the two techniques are not in agreement with each other, as can be seen in Fig. 1.1. After the possibility of experimental errors had been ruled out, the proposed explanation of the discrepancy between the two measurements is a two-photon exchange (TPE) [7, 8] contribution to the scattering, which is a more significant effect in the Rosenbluth results. No existing model can completely reconcile the two measurements and more data are needed.

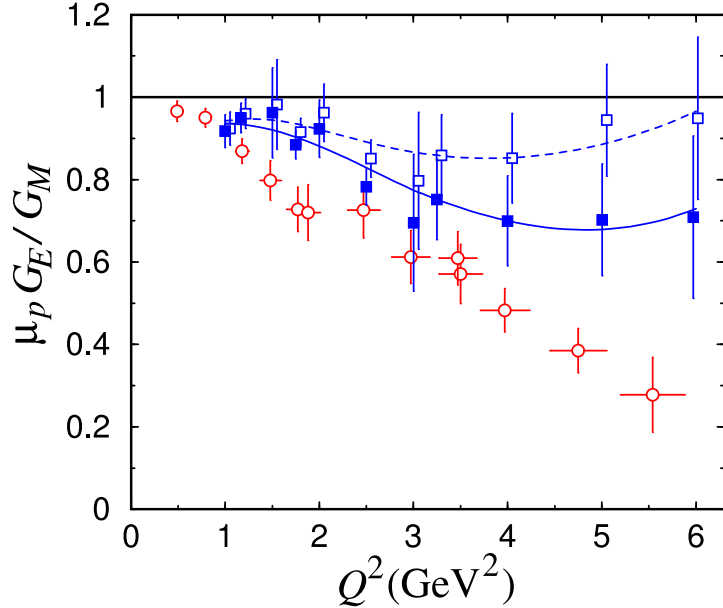


Figure 1.1: $\mu_p G_E / G_M$ vs Q^2 from [8]. Results from polarization transfer experiments [9, 10] are given by the hollow circles. Rosenbluth separation results [11, 12] are given by hollow squares. The filled squares show the effect on the Rosenbluth data when TPE corrections are included. The dashed and solid lines represent a global fit [13], and the size of the effect on it due to TPE.

1.3 Inelastic Scattering

While the initial and final state of the target are the same for elastic scattering, this is not true for inelastic scattering. In this case, the final hadronic state has no limitations: the target can be excited, or broken up, with multiple particles in the final state. It is convenient to define the different kinematic regions in terms of W and Q^2 , where W^2 is the invariant mass of the final hadronic state and Q^2 is the

4-momentum transfer squared. These are given by:

$$Q^2 = -q^2 = \vec{q}^2 - \nu^2 = 4EE' \sin^2(\theta/2) \quad (1.9)$$

$$W^2 = 2M\nu + M^2 - Q^2$$

where E and E' are the energies of the incoming and scattered electron, M is the nucleon mass, and θ is the scattering angle.

Experiments done in the *deep inelastic* regime, defined by kinematics where $W > 2\text{GeV}$ and $Q^2 > 1\text{GeV}^2$, found that inelastic cross sections were only weakly Q^2 dependent, signaling that electrons were scattering from the point-like components of the nucleon. These point-like objects were later identified with quarks [14], but were at first referred to simply as *partons*.

Follow-up experiments to study nucleon structure have been carried out, establishing that quarks are spin 1/2 objects. In fact, the differential cross section for deep inelastic scattering is written in a form similar to Eq. 1.4, in terms of two form factors, W_1 and W_2 , referred to as the inelastic *structure functions*:

$$\frac{d\sigma}{d\Omega dE'} = \frac{\alpha^2 \cos^2(\theta/2)}{4E^2 \sin^4(\theta/2)} [W_2(Q^2, \nu) + 2W_1(Q^2, \nu) \tan^2(\theta/2)] \quad (1.10)$$

Not that the expression in Eq. 1.10 that multiplies the structure functions is the Mott cross section. For inelastic scattering, Bjorken [16] put forth the idea that in the limit of infinite momentum and energy transfers, these structure functions should become

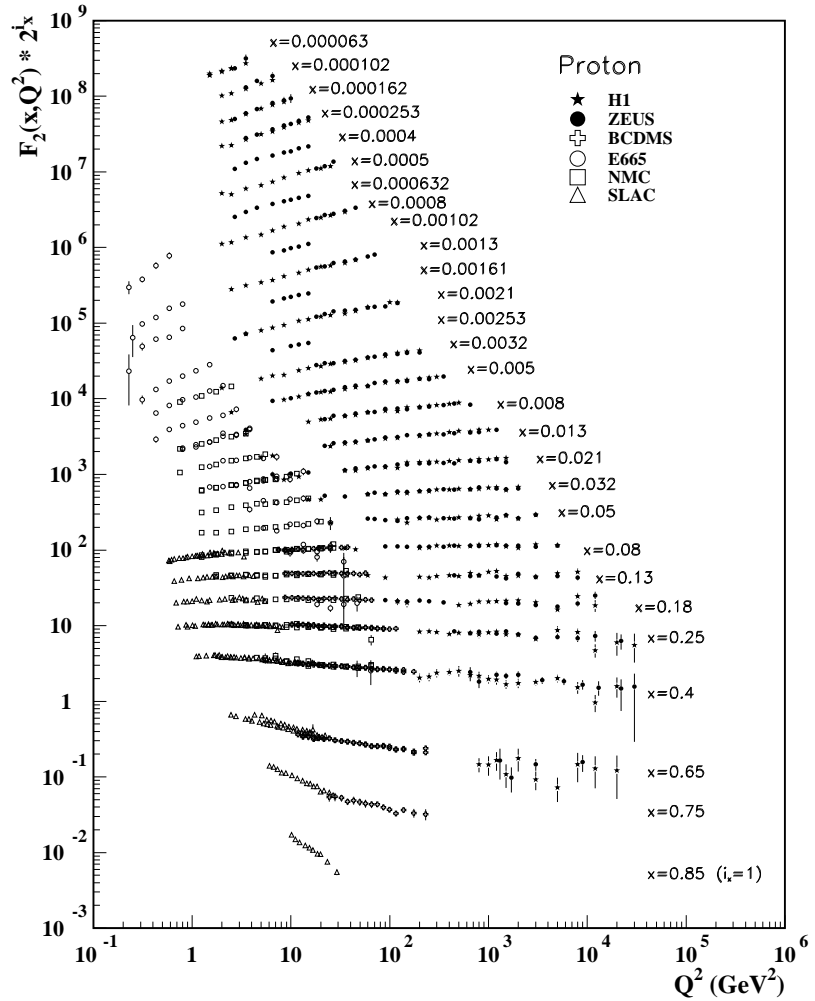


Figure 1.2: A representative, but not complete sample of the measurements of the F_2^p structure function for a range of x values taken from [15]. The points have been scaled by 2^{i_x} , where i_x indicates the number of the x bin (1-28). The structure function appears to be Q^2 -independent for $0.1 < x < 0.4$. The scale breaking seen at lower values of x is known to be the result of a large contribution from gluons, which dominate at low x and high Q^2 .

dependent on only one variable, x , rather than both Q^2 and ν . This turned out to be the case [17], and the structure functions have been found to *scale* in the limit of high energy and momentum transfers and are usually redefined as:

$$F_1(x) = mW_1(x) \quad \text{and} \quad F_2(x) = \nu W_2(x) \quad (1.11)$$

In this limit, the two structure functions are related to each other through the Callan-Gross relation [18], $F_2(x) = 2xF_1(x)$, based on the interpretation of structure functions as linear combinations of quark distribution functions. Note that the new variable that the structure functions depend on is x , or *Bjorken* x , given by $x = \frac{Q^2}{2m\nu}$. A representative plot of F_2^p measurements is seen in Fig. 1.2. Scaling behavior can be seen for $0.1 < x < 0.4$ and $\ln Q^2$ behavior is seen for low values of x .

Outside of the scaling regime, structure functions are most often presented in terms of the cross sections for absorption of transverse and longitudinal virtual photons. The inelastic cross section is related to these through:

$$\frac{d\sigma}{d\Omega dE} = \Gamma [\sigma_T(W^2, Q^2) + \epsilon\sigma_L(W^2, Q^2)] \quad (1.12)$$

The ratio of the two contributions defines $R = \sigma_L/\sigma_T$, which is related to the structure functions through:

$$R \equiv \frac{\sigma_L}{\sigma_T} = \frac{W_2}{W_1} \left(1 + \frac{\nu^2}{Q^2} \right) - 1 \quad (1.13)$$

The individual structure functions can be determined if the cross section is measured

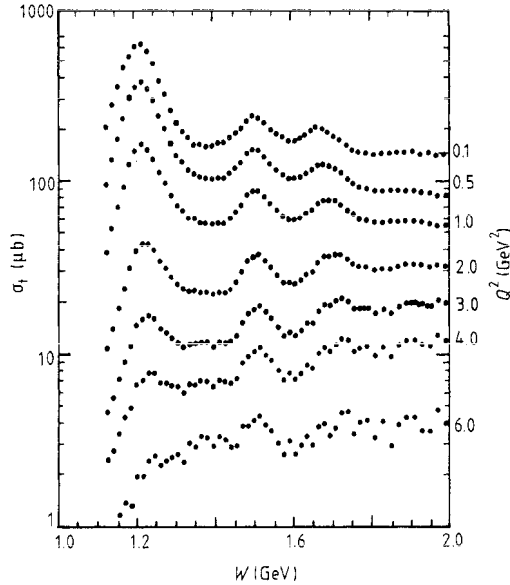


Figure 1.3: Electron-Proton cross sections measured at several sets of kinematics, plotted as a function of the invariant mass W [19]. The Δ resonance is well defined at $W = 1232$ MeV, and the second and third resonance regions are also seen.

at several angles for a fixed ν and Q^2 , in the same way that the form factors are separated. In the deep-inelastic region, R is known to be small [20] and zero or small constant values have been used in some analyses.

1.3.1 Resonances

Inclusive measurements of electron scattering have revealed the existence of several resonances in the inelastic region. These resonances correspond to excited nucleon states. In Fig. 1.3, the three resonance regions are clearly seen with $1 \text{ GeV} < W < 2 \text{ GeV}$. The resonance transition form factors differ from elastic ones and the ability to measure them depends on the knowledge of the relative contributions of longitudinal and transverse cross sections, discussed above. Many early studies of the resonance form

factors relied on assumptions about the behavior of $R = \sigma_L/\sigma_T$ in this region. Prior to Jefferson Lab experiment E94-110 [21], no high precision Rosenbluth-separated data was available to allow for a detailed study of the resonance structure. The longitudinal contribution was found to be significant, which was contrary to the existing assumptions.

Comparisons of the Q^2 -dependence of the resonance form factors to elastic ones require them to be defined in terms of σ_T . The transition form factors [22, 23] can then be written as

$$F^2(Q^2) = \frac{1}{4\pi\alpha} \frac{\Gamma_R W_R}{Q^2} (W_R^2 - M^2) \sigma_T \quad (1.14)$$

with W_R being the energy of the resonance and Γ_R , its width. In a famous observation [24], it was noted that the structure function νW_2^A , when examined in terms of the dimensionless variable $w' = 1/x + M^2/Q^2$, has the same Q^2 behavior as the resonance form factors. In fact, averaging over the resonance peaks produces the scaling curve for the structure functions, which is seen in Fig. 1.4. The resonance peaks do not disappear with increasing values of Q^2 , but decrease in strength and move to lower values of w' , following the magnitude of the scaling limit curve. This is known as the Bloom-Gilman duality and continues to be a subject of great interest.

1.3.2 EMC Effect

An experiment carried out at CERN by the European Muon Collaboration (EMC) [26], made the unexpected and surprising discovery that the deep inelastic structure

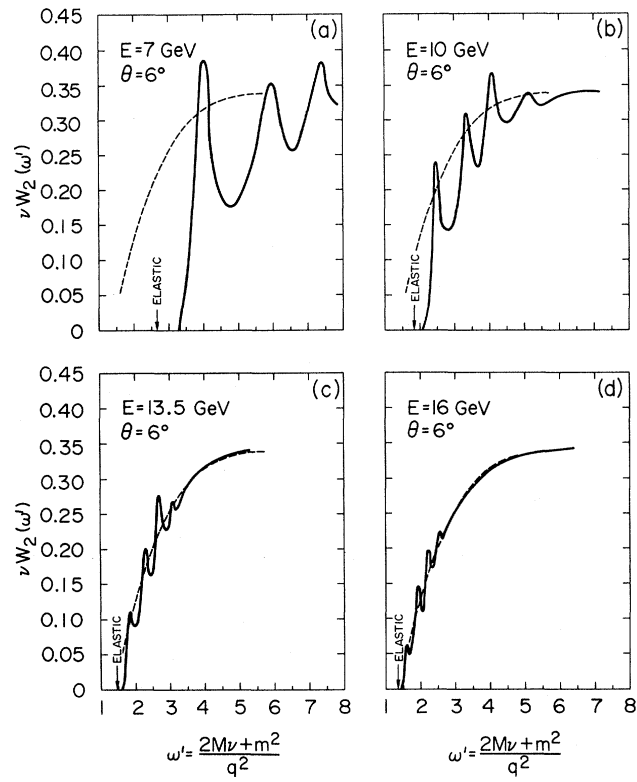


Figure 1.4: The structure function νW_2^A plotted as a function of $w' = 1/x + M^2/Q^2$ for increasing values of Q^2 . Dashed line corresponds to the scaling curve. Figure from [24] with data from [25].

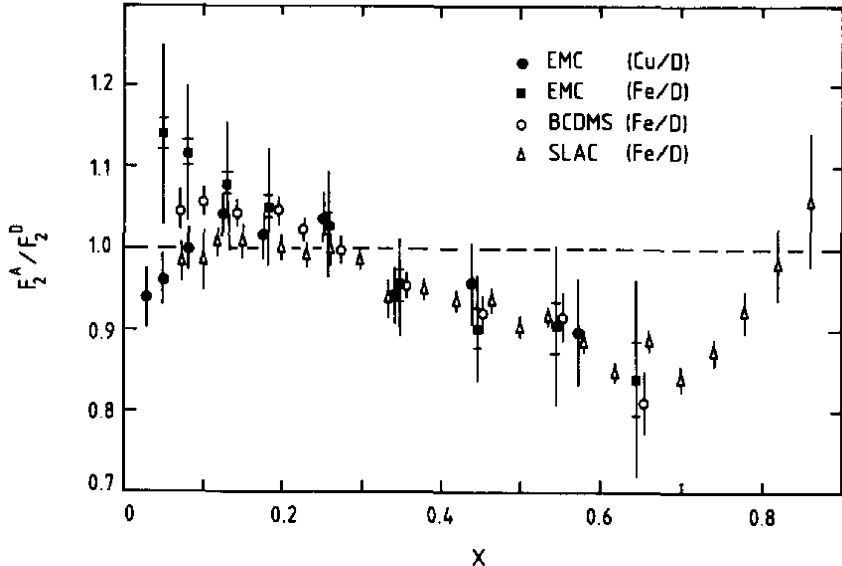


Figure 1.5: Ratio of the F_2 structure functions for copper and iron to that for deuterium. Data collected by the EMC collaboration as well as earlier data from SLAC is shown [26].

function, F_2 , for heavy targets (e.g. iron, copper) was not the same as that for deuterium. This indicated modification by the nuclear medium - a bound nucleon behaved differently from a free one. Given the fact that the binding energies (a few MeV) are extremely small when compared to the experimental energy transfer (on the order of GeV), no noticeable effect was expected. Fig. 1.5 shows the ratio of the F_2 structure functions from heavy nuclei to those of deuterium. The shape at low x ($x < 0.1$) is thought to be the result of nuclear “shadowing”[27], where the virtual photon interacts with the neighbors of the struck nucleon. The shape of the curve at higher x (up to $x \approx 0.7$) is considered to be due to the binding of the struck nucleon in the nucleus and for x higher than 0.7, the result of the motion of the

bound nucleons [28]. Measurements of the EMC effect for different nuclei and over a wide kinematic range have been performed since the original discovery. Jefferson Lab experiment E03-103 [29] was one such effort and it was complementary to the experiment described here. E03-103 ran concurrently and examined the cross sections at the low end of the x -coverage.

1.3.3 Quasielastic Scattering

The quasielastic kinematic region is defined by energy and momentum transfers where single nucleon knockout is the dominant process. In quasielastic scattering, the virtual photon is absorbed on a single nucleon. In electron-nucleus scattering, the quasielastic contribution is dominant at momentum transfers between 500 MeV/c and 2 GeV/c, although inelastic contributions can be significant at large Q^2 . The dominant feature in the inclusive spectrum is a broad peak that is a result of scattering from a moving bound nucleon in the nucleus. A more detailed description of the reaction follows in Sec. 2.1 and a comprehensive review can be found in [30].

The information about the nuclear response is encapsulated inside the *Spectral Function*, which is not an experimental observable. It describes the energy and momentum distributions of the nucleons inside nuclei and can most easily be introduced by considering the $(e, e' p)$ reaction in the quasielastic region. Here, an electron ejects a proton from the target nucleus and the final state system consists of A-1 nucleons, which can be bound or not. In the Independent Particle Shell Model, the spectral

function for A and A-1 is given by:

$$S(\vec{p}_0, E_0) = \sum_{\alpha} N_{\alpha} |\Psi_{\alpha}(p_0)|^2 \delta(E_0 + \Sigma_{\alpha}) \quad (1.15)$$

where $\Psi_{\alpha}(p_0)$ is the single proton wave function in a ground state α , in the momentum-space representation, p_0 is the initial momentum of the nucleon, Σ_{α} is the energy eigenvalue, and N_{α} is the occupancy. An experimentally determined beryllium spectral function is shown in Fig. 1.6, where several peaks in energy can be seen. These peaks are identified with holes in the orbitals - i.e. the knocked out nucleons from different ground state orbitals. In this model, the nucleons are assumed to occupy single particle states and move independently of each other. The IPSM predicts that the spectroscopic factor, obtained by integrating the momentum distribution of a given shell, is equal to the number of nucleons that can occupy that shell.

However, experiments (see, for example [32]) yielded a spectroscopic factor that was $\approx 70\%$ of the prediction for a wide range of nuclei. This deficiency is thought to be largely due to Short Range Correlations that are not included in IPSM and which produce high momentum nucleons as a result of the strong repulsive $N - N$ force at short distances. SRCs will be discussed in more detail in Sec. 2.2.3.

On the low energy loss side of the quasielastic peak (see Fig. 1.7), we will examine the quasielastic response function $F(|\mathbf{q}|, y)$, which is an energy and momentum integral of the spectral function. $F(|\mathbf{q}|, y)$ is expected to scale in y , the minimum momentum of the struck particle in the direction of momentum transfer in the kinematic

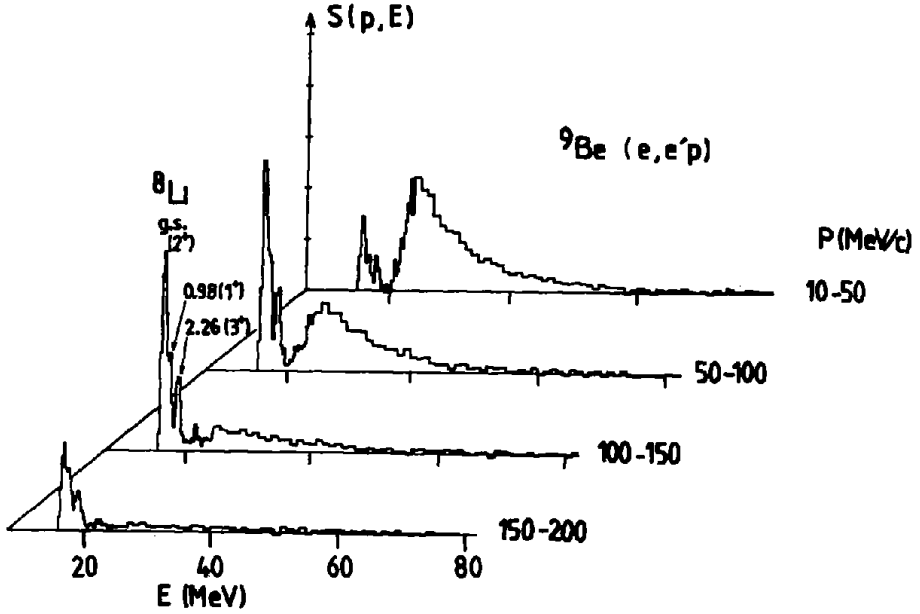


Figure 1.6: Spectral function for Be is shown from [31], where the binding energy spectra can be seen for several bins of recoil momentum. The peaks in the binding energy spectra correspond to holes in the $1-p$ state. See Sec. 1.3.3 for details.

regime where inelastic contributions and Final State Interactions are minimal. On the side of the quasielastic peak where the energy loss is higher, inelastic scattering begins to dominate quickly, and it is more appropriate to examine the data through the study of the inelastic structure function, F_2^A . The superscript A , in this case, signals that this is a nuclear structure function, which differs from the nucleon structure function discussed earlier in Sec. 1.3 due to medium modification. The nuclear structure function is expected to scale in the same way as those of free nucleons. When scattering from a nucleus, momentum is shared between the constituents of the nucleus, and x can vary between 0 and $\approx A$, rather than 0 and 1, as for a free nucleon.

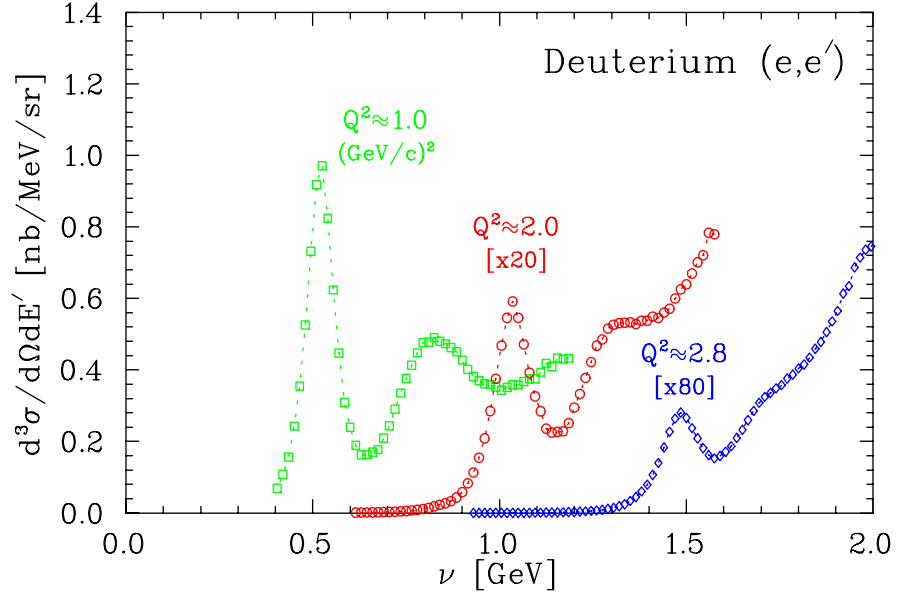


Figure 1.7: The differential cross section for deuterium is shown as a function of energy loss ν for three sets of kinematics. The Q^2 values shown are those at the quasielastic peak. Data shown is that from JLab experiment E89-008. [33]

This nuclear structure function, νW_2^A , has been observed to scale in x in the deep inelastic region and over a wider kinematic range if examined [34] in the Nachtmann variable $\xi = \frac{2x}{1 + \sqrt{1 + 4M^2x^2/Q^2}}$, which represents the fractional quark lightcone momentum, and which reduces to x for very large values of Q^2 .

1.4 Experiment E02-019

Experiment E02-019 ran in the fall of 2004 at the Thomas Jefferson National Accelerator Facility in experimental Hall C. It was an extension of a previous experiment, E89-008, with a higher beam energy, which allows measurements at high Q^2 values with a wide range of targets from very light (^2H) to very heavy (^{197}Au). The kinematic

coverage of E02-019 is shown in Fig. 1.8.

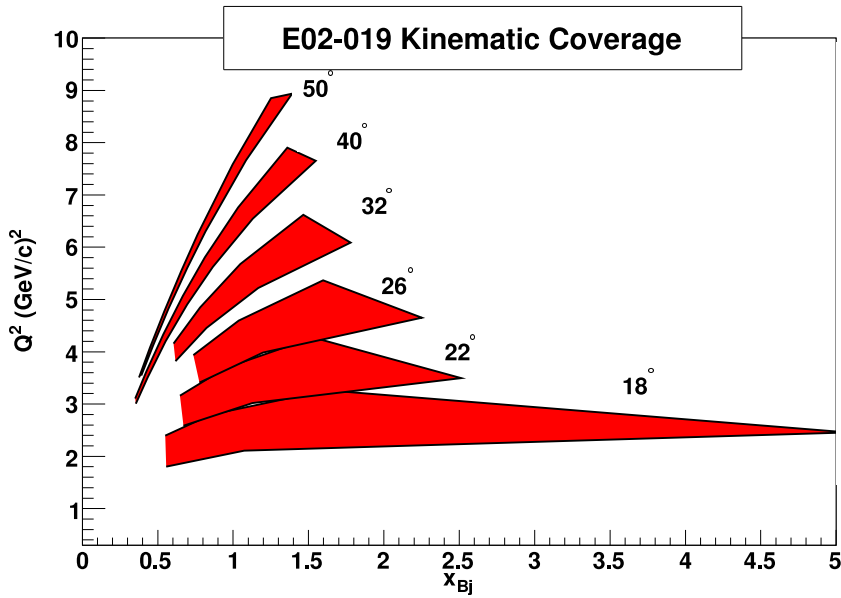


Figure 1.8: Kinematic Coverage for JLab experiment E02-019. The highest x values are not accessible to the light targets.

In the next chapter, we will examine the physics motivation for the experiment in much more detail. Several different interpretations for the data will be presented. In Chapter 3, the experimental setup will be discussed, including beam line, target, and spectrometer. In Chapter 4, a detailed discussion of the analysis procedure will follow. It will include the steps for extracting experimental cross sections as well as descriptions of all the corrections that were applied to the data. Finally, in Chapter 5, results will be presented, including cross sections, structure and scaling functions. Comparisons with theoretical calculations will be done, where possible. Implications

of the data as well as prospects for further measurements will be discussed.

Chapter 2

Theoretical Overview

The quasielastic scattering process will be presented in the Plane Wave Impulse Approximation (PWIA) which will allow us to develop the scaling of a reduced cross section in terms of y and $F(y, |\mathbf{q}|)$, where y is the longitudinal momentum of the struck nucleon. We will examine the approach to scaling with increasing momentum transfer and discuss the assumptions implicit in the presentation.

The scaling limit of the inelastic nuclear structure function $\nu W_2^A(x, Q^2)$ will also be examined in both x and ξ .

2.1 Quasi-elastic Cross Section

Quasi-elastic scattering describes the knock-out of a nucleon from the nucleus by an electron. The final state is made up of the scattered electron, the ejected nucleon, and the remainder of the nucleus, (A-1), which can possibly be in an excited state

(see Fig. 2.1).

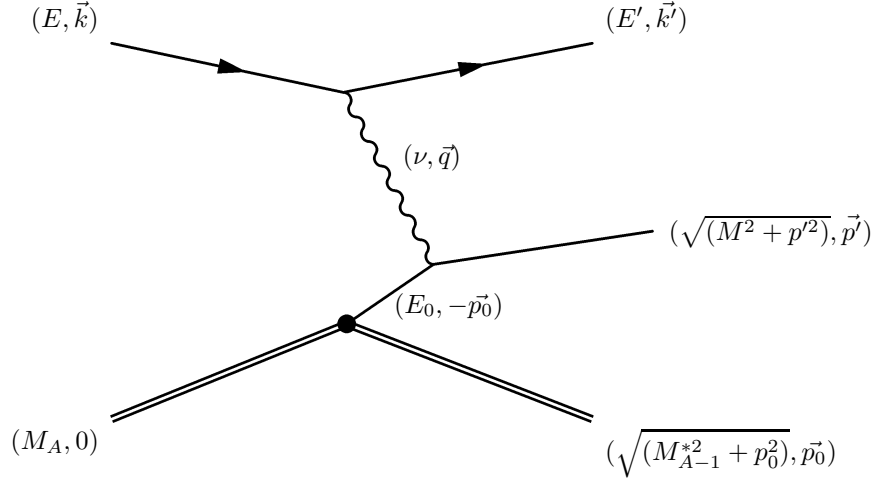


Figure 2.1: The quasi-elastic reaction. E, \vec{k} and E, \vec{k}' are the energies and momenta of the incoming and scattered electron. The virtual photon of energy and momentum (ν, \vec{q}) interacts with the nucleus M_A , at rest in the laboratory. The result is a knocked out nucleon with energy and momentum $\sqrt{M^2 + p'^2}, \vec{p}'$ and the recoil nucleus with energy and momentum $\sqrt{M_{A-1}^{*2} + p_0^2}, -\vec{p}_0$.

The most general expression for electron scattering in the one-photon exchange approximation is [35]

$$\frac{d^4\sigma}{(d\Omega dE)_N (d\Omega dE')_e} = \frac{2\alpha^2}{Q^4} \frac{E'_e}{E_e} |p_N| L^{\mu\nu} W_{\mu\nu}^A \quad (2.1)$$

where the subscripts e and N denote the electron and the ejected particle, respectively, Q is the 4-momentum transfer and $L^{\mu\nu}$ and $W_{\mu\nu}^A$ are the leptonic and nuclear response tensors. While the leptonic tensor is completely determined by kinematics, in order to calculate the nuclear response tensor for the case of multi-GeV incident electrons, one must make several simplifying assumptions.

One prescription for this is the Impulse Approximation (IA), where the dominant process is taken to be scattering from individual nucleons and only the motion of the struck nucleon must be treated relativistically. In the IA, the cross section is written down in terms of the nuclear spectral function $S'(E_0, p_0)$, which represents the probability of finding a nucleon of energy E_0 and momentum \vec{p}_0 in the nucleus. The Plane Wave Impulse Approximation (PWIA) is the simplest implementation of this scheme and includes the additional assumption that one neglects the final state interactions of the knocked out nucleon with the residual nucleus. These interactions are small and should decrease with increased values of Q^2 , corresponding to shorter interaction times.

This allows the nuclear response tensor to be written as [36]

$$W_{\mu\nu}^A(q) = \int d^3p dE S'(E_0, p_0) \tilde{W}_{\mu\nu}(p_0, q) \quad (2.2)$$

where $\tilde{W}_{\mu\nu}(p_0, q)$ is the electromagnetic tensor for a bound nucleon. Within the IA, binding effects can be accounted for, and one can use the free nucleon tensor ($\tilde{W}_{\mu\nu}(p_0, q) \rightarrow W_{\mu\nu}(p_0, \tilde{q})$) written in terms of $\tilde{q} \equiv (\tilde{\nu}, \vec{q})$ where the energy loss is redefined in the following way, accounting for partial transfer of energy to the spectator system [37]:

$$\tilde{\nu} = \nu + M_A + E_{A-1} + \sqrt{|\vec{p}_0|^2 + m^2} \quad (2.3)$$

The terms describing the electromagnetic interaction can be factorized from the spec-

tral function and the total cross section can be written as a sum of the off-shell electron-nucleon cross sections weighted by the spectral function:

$$\frac{d^5\sigma}{dE'd\Omega d^3\vec{p}} = \sum_{nucleons} \sigma_{eN} \cdot S'_N(E_0, p_0) \quad (2.4)$$

With an unpolarized target, S'_N can be taken to be spherically symmetric, with the following normalization condition:

$$4\pi \int_0^\infty dE \int_0^\infty p^2 S'_N(E_0, p_0) dp = 1. \quad (2.5)$$

To get the inclusive cross section, we separate the proton and neutron contributions and integrate over the final state of the unobserved nucleon:

$$\frac{d^2\sigma}{dE'd\Omega} = \int (Z\sigma_{ep}S'_p(E_0, p_0) + N\sigma_{en}S'_n(E_0, p_0)) d^3\vec{p} \quad (2.6)$$

By neglecting any differences in the spectral functions for protons and neutrons, we can replace the nucleon-specific spectral functions with the more general $S'(E_0, p_0)$, and then factor it out. The 3-momentum transfer, \vec{q} , is fixed by measuring the incoming and scattering electrons, giving $\vec{p} = \vec{p}_0 + \vec{q}$ and $d^3\vec{p} = d^3\vec{p}_0$. Using spherical coordinates, where θ is the angle between \vec{p}_0 and \vec{q} and ϕ is the angle between the electron scattering plane and the (\vec{p}_0, \vec{q}) scattering plane and noting that S' has no ϕ dependence, we can rewrite the inclusive cross section as:

$$\frac{d^2\sigma}{dE'd\Omega} = 2\pi \int \tilde{\sigma}_0 \cdot S'(E_0, p_0) \cdot p_0^2 dp_0 d(\cos\theta) \quad (2.7)$$

where $\tilde{\sigma}_0$ is defined as

$$\tilde{\sigma}_0 = \frac{1}{2\pi} \int_0^{2\pi} (Z\sigma_{ep} + N\sigma_{en}) d\phi \quad (2.8)$$

The initial and final state particles must be on mass-shell, which when combined with energy and momentum conservation, gives the constraints:

$$(M_A - E_0)^2 = M_{A-1}^{*2} + p_0^2 \quad (2.9)$$

as well as

$$M_A + \nu = \sqrt{M^2 + (\vec{p}_0 + \vec{q})^2} + \sqrt{M_{A-1}^{*2} + \vec{p}_0^2} \quad (2.10)$$

where we define the following:

$$\begin{aligned}
 M_A &= \text{mass of the target nucleus} \\
 M_{A-1}^* &= \text{mass of the recoiling (A - 1) nucleus} \\
 M &= \text{mass of the ejected nucleon} \\
 E_s \equiv M_{A-1}^* + M - M_A &= \text{separation energy (see Table. 2.1).} \quad (2.11)
 \end{aligned}$$

Using Eq. 2.9, solving for M_A and substituting that expression into Eq. 2.10, we get

a simplified expression:

$$E_0 + \nu - \sqrt{M_{A-1}^{*2} + p_0^2 + q^2 + 2pq \cos \theta} = 0. \quad (2.12)$$

Table 2.1: Separation Energies used in $F(y, |\mathbf{q}|)$ extraction [38]. Each of these is the minimum energy to remove a nucleon from the given nucleus.

Target	E_s^{min} (MeV)
^2H	2.2
^3He	5.5
^4He	20
^9Be	16.9
^{12}C	16
^{63}Cu	6.1
^{197}Au	5.8

For any given set of p_0 , \vec{q} , and ν values, we can determine E_0 . This allows us to rewrite the expression in 2.7 as follows:

$$\frac{d^2\sigma}{dE'd\Omega} = 2\pi \int \tilde{\sigma}_0 \cdot S'(E_0, p_0) \cdot \delta(\text{Arg}) \cdot p_0^2 dp_0 d(\cos \theta) dE \quad (2.13)$$

where the argument of the delta function is the left-hand side of Eq. 2.12. Next, we can use the δ -function to perform the integral over $\cos \theta$, the result of which is:

$$\frac{d^2\sigma}{dE'd\Omega} = 2\pi \int \tilde{\sigma}_0 \cdot \frac{E_N}{|p_0||q|} \cdot S'(E_0, p_0) \cdot p_0^2 dp_0 dE_0 \quad (2.14)$$

where the energy of the final state nucleon is $E_N = \sqrt{M^2 + (\vec{p} + \vec{q})^2}$.

It is more convenient to rewrite the spectral function in terms of E_s , the separation energy, rather than E_0 , the nucleon's initial energy. The spectral function becomes:

$$S(E_s, p_0) dE_s = -S'(E_0, p_0) dE_0 \quad (2.15)$$

where the Jacobian from the $E_0 \rightarrow E_s$ transformation has been absorbed into the new definition of S . Next, we define $\tilde{\sigma} = \tilde{\sigma}_0 \cdot K$, where $K = E_N/|q|$, and the cross section becomes:

$$\frac{d^2\sigma}{dE'd\Omega} = 2\pi \int_{E_s^{min}}^{E_s^{max}} \int_{p_0^{min}(E_s)}^{p_0^{max}(E_s)} \tilde{\sigma} \cdot S(E_s, p_0) \cdot p_0 dp_0 dE_s \quad (2.16)$$

The limits of the p_0 integral are given by $|y_1|$ and $|y_2|$, the solutions of p_0 to Eq. 2.10, for the case where \vec{p}_0 and \vec{q} are parallel. An example of the integration region of Eq. 2.16 is shown in Fig. 2.2. The $E_s = E_s^{max} = \sqrt{(M_A + \nu)^2 - q^2} - M_A$ limit (for which $p_0^{max} = p_0^{min}$) occurs when the struck nucleon is at rest in its final state and $E_s = E_s^{min}$ occurs when the recoiling nucleus is in its ground state. In the latter case, the minimal longitudinal momentum also defines the y scaling variable.

$$y = \frac{\vec{q}(\vec{q}^2 - W') + \sqrt{\vec{q}^2(W' - \vec{q}^2)^2 - (W^2 - \vec{q}^2) \cdot (4W^2M_{A-1}^2 - \vec{q}^4 + 2W'\vec{q}^2 - W'^2)}}{2(W^2 - \vec{q}^2)} \quad (2.17)$$

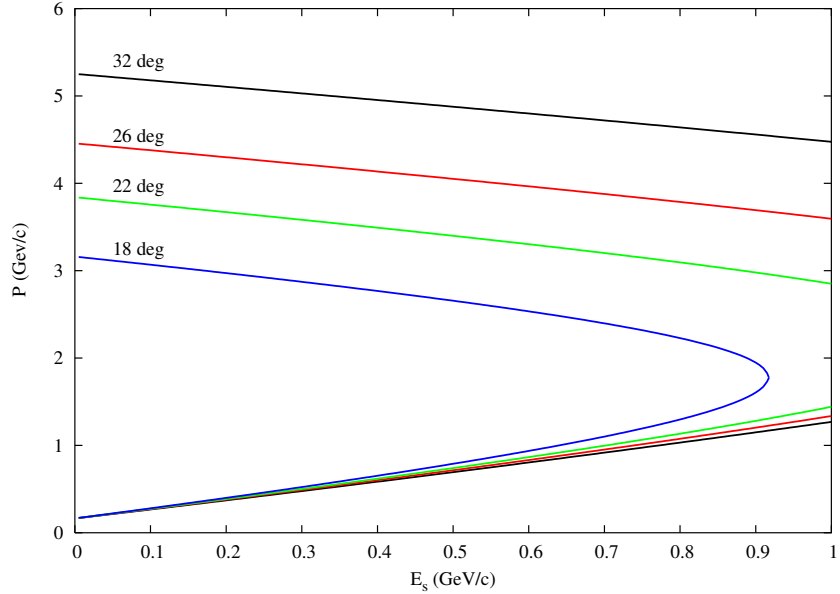


Figure 2.2: The region of integration (to the left of each curve) for Eq. 2.16 shown for selected angle settings, ^{12}C target. The E' value for each angle was calculated with $y_1=-0.2$ GeV/c, E_s^{\min} of 0.016 GeV, and initial energy of 5.766 GeV.

where W and W' are defined as:

$$W = M_A + E - E' - E_s$$

$$W' = W^2 + M_{A-1}^2 - M^2$$

The expression in Eq. 2.16 can be further simplified. Since $\tilde{\sigma}$ varies slowly over the breadth of the spectral function, we can remove it from the integral and evaluate it at the kinematics corresponding to the lower integration limits, when the spectral function is at maximum within the limits. It is useful to be able to visualize a nuclear spectral function, an example of which is seen in Fig. 2.3 for ^3He , and the curve corresponding to single nucleon knockout is clearly visible along with a continuum

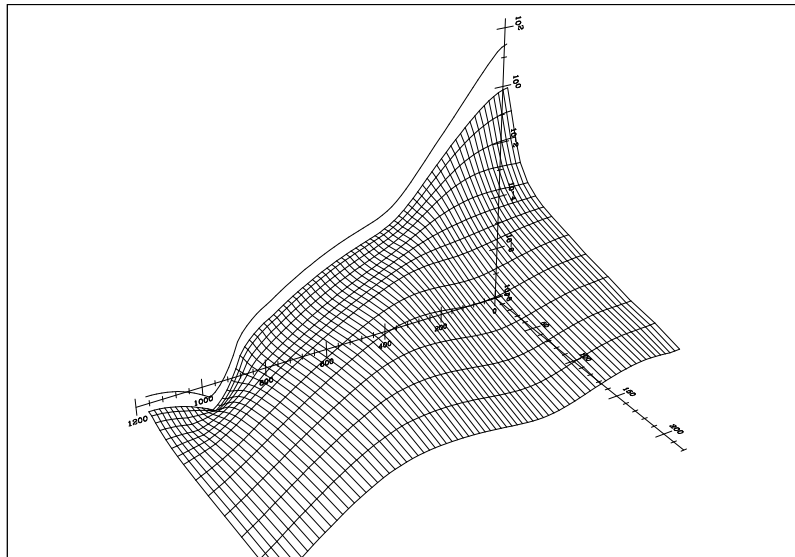


Figure 2.3: Theoretical calculation by the Hanover group of the spectral function for ${}^3\text{He}$, with separation energy (GeV) on the right-hand axis and momentum (GeV/c) on the left-hand axis. The calculation was performed using the Fadeev method and the Paris potential. Contributions from correlated nucleon pairs with isospin=0 in the final state are included [39].

corresponding to higher removal energies. The rapid decrease of the spectral function with energy and momentum also lets us extend the upper limits of the integrals to infinity. The error associated with this decreases quickly with increasing values of Q^2 . Finally, since the spectral function is peaked around $E_s = E_s^{min}$ for all momenta, we can also approximate the lower limit of the momentum integral with a constant value, $|y_1(E_s^{min})| = |y|$. These simplifications yield:

$$\frac{d^2\sigma}{dE'd\Omega} = 2\pi \tilde{\sigma}_0 K \int_{E_s^{min}}^{\infty} \int_{|y|}^{\infty} S(E_s, p_0) \cdot p_0 dp_0 dE_s \quad (2.18)$$

2.1.1 y-scaling

Having reduced the nuclear quasielastic cross section to the form given by Eq. 2.18, it's now possible to examine its scaling behavior and the approach to it as a function of Q^2 . Scaling is the name given to the reduced cross section when its behavior becomes independent of Q^2 [3]. The double integral over the spectral function in Eq. 2.18 defines the nuclear scaling function $F(y, |\mathbf{q}|)$:

$$F(y, |\mathbf{q}|) = 2\pi \int_{E_s^{min}}^{\infty} \int_{|y|}^{\infty} S(E_s, p_0) \cdot p_0 dp_0 dE_s \quad (2.19)$$

Note that the energy integral over the spectral function alone yields a momentum distribution of the nucleons inside the nucleus. This simplified expression is a common

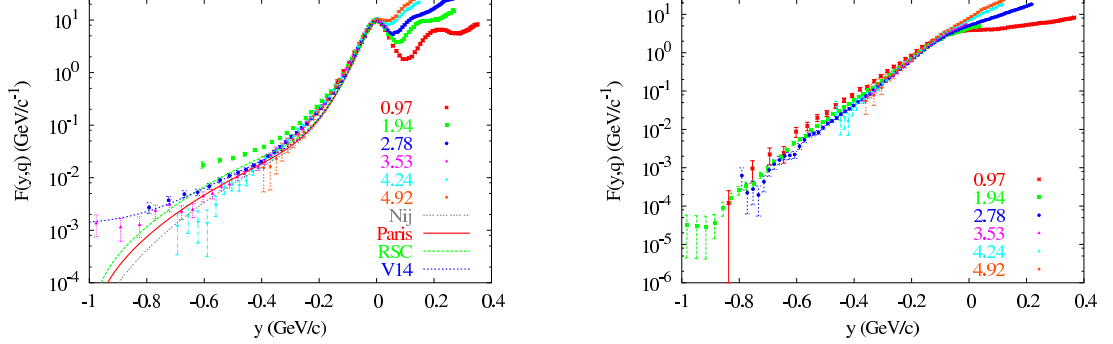


Figure 2.4: $F(y, |\mathbf{q}|)$ extracted from deuterium cross sections for E89-008. [40]. The numbers indicate the Q^2 values of the different data sets at the quasielastic peak. The inelastic contribution has not been subtracted, but should be small for $y < 0$.

definition of $F(y, |\mathbf{q}|)$ and is written as:

$$F(y, |\mathbf{q}|) = 2\pi \int_{|y|}^{\infty} n(p_0) \cdot p_0 \, dp_0 \quad (2.20)$$

This scaling function can be extracted from experimental data provided that the assumptions that went into its derivation apply: the remainder nucleus is in its ground state, there's no contribution from inelastic processes or Final State Interactions, and there's no effect from the nuclear medium modification. Scaling functions for ^2H and ^{12}C extracted from previous data [40] can be seen in Fig. 2.4.

It should be noted that the spectral function can be broken into 2 parts, with one, $S_{gr}(E_s, p_0)$ corresponding to the probability distribution of having the recoil nucleus in the ground state, and the other, $S^*(E_s, p_0)$ corresponding to an excited state [41].

The scaling function is then rewritten to reflect this:

$$F(y, |\mathbf{q}|) = 2\pi \int_{|y|}^{\infty} n_{gr}(p_0) p_0 dp_0 - B(y) \quad (2.21)$$

where $B(y)$ is the contribution given by the integral over $S^*(E_s, p_0)$ and is referred to as the *binding correction* to the scaling function. This contribution has a Q^2 -dependence for small momentum transfers and breaks the direct relationship between $F(y)$ and $n(p_0)$. When the binding correction is absent, as in the case of deuterium, then the simplified relationship of Eq. 2.20 between the scaling function and the momentum distribution holds.

A more serious roadblock to extracting momentum distributions is the contribution from Final State Interactions between the struck nucleon and the remainder nucleus, within a distance of $1/|\mathbf{q}|$. In the presence FSIs, one can still extract nucleon momentum distributions from the data if the asymptotic value of the scaling function can be determined from data taken at finite momentum transfer. This is done by examining the Q^2 limit of the scaling function for constant y -values as shown in Fig. 2.5.

However, while the fall off at low values of Q^2 is steep, it continues for high values of Q^2 as well, but at a slower rate. The fast fall off at low Q^2 is due to the effects of FSIs, whereas the further falloff has been theorized to be the result of the near cancellation of contributions from FSIs and the high removal energy tail of the spectral function [43].

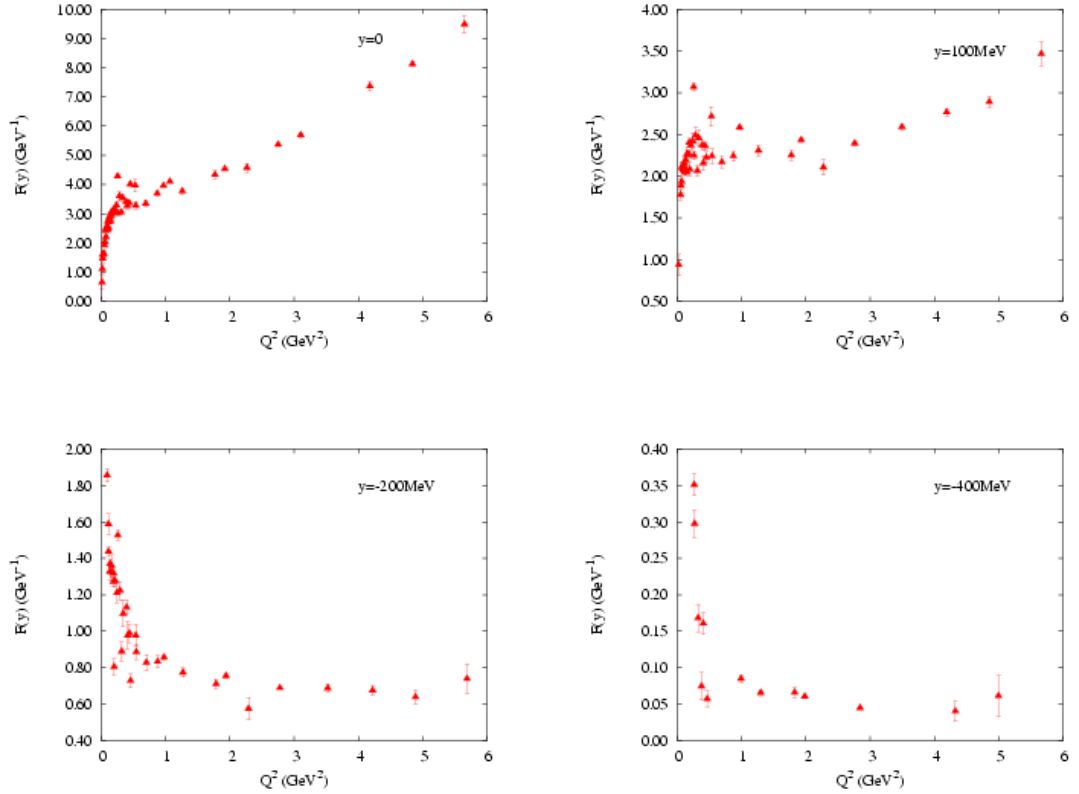


Figure 2.5: Approach to scaling of $F(y, |\mathbf{q}|)$ for ^{12}C . $F(y, |\mathbf{q}|)$ was extracted from available inclusive data [42] for a variety of y values. As y becomes more negative, the inelastic contribution, which is largest at high Q^2 , decreases rapidly and the data appear to approach an asymptotic limit. The steep fall-off with Q^2 reflects the fact that FSIs also fall with Q^2 .

In order to get the asymptotic limit of the scaling function from the experimental data in the presence of FSIs, one can follow the approach described in [44] and rewrite $F(|\mathbf{q}|, y)$ as a power series of $1/q$. This expansion in $1/q$ yields:

$$F(y, |\mathbf{q}|) = F(y) + \frac{F_{(-1)}(y)}{q} + \frac{F_{(-2)}(y)}{q^2} + \frac{F_{(-3)}(y)}{q^3} + \dots \quad (2.22)$$

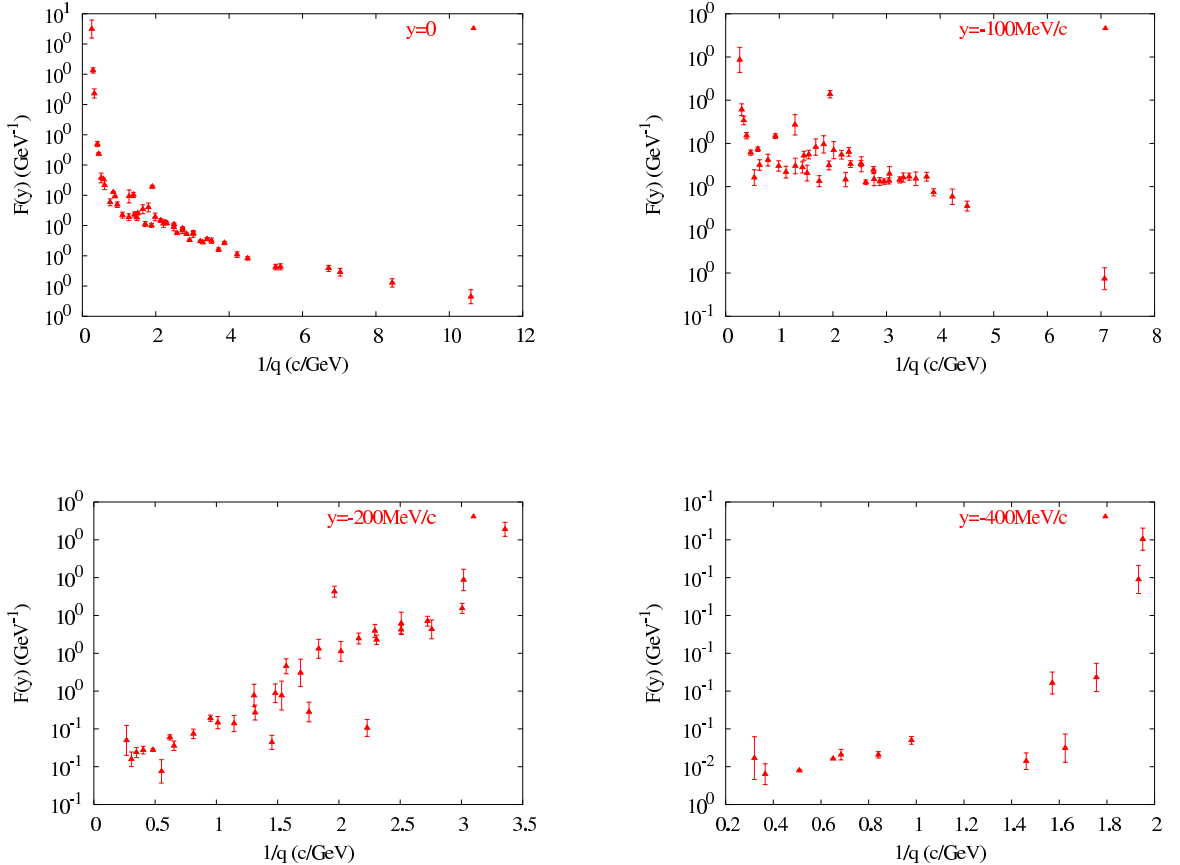


Figure 2.6: Experimental scaling function, $F(y, |\mathbf{q}|)$ for ^{12}C as a function of the inverse of momentum transfer for a variety of y values. For the low y values, the inelastic contribution is not negligible.

For large values of q , the scaling function can be approximated by the first two terms on the right hand side, with the first term being the asymptotic limit of the scaling function and the second term representing the effects of FSIs (as do the other q -dependent terms, which can be neglected in this limit). If we now plot the experimental scaling function versus $1/q$ for fixed values of y (Fig. 2.6), the extrapolated y -intercept should represent the asymptotic scaling function for that y value.

Finally, with the asymptotic value of the scaling function in hand, one can go on

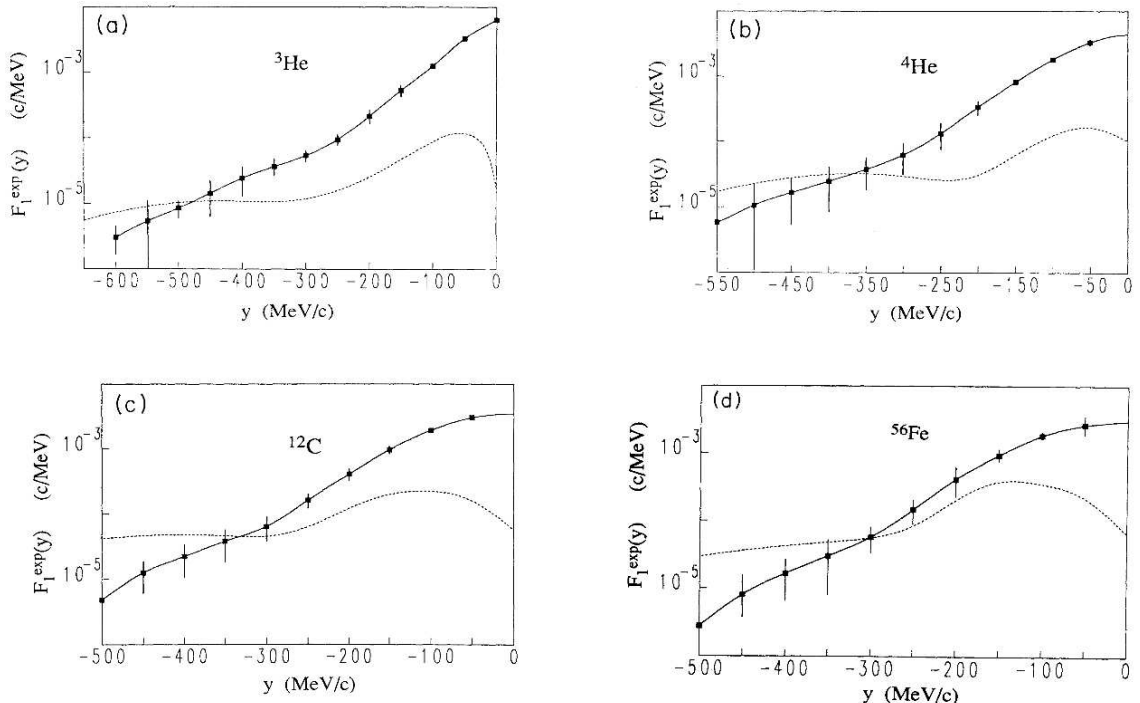


Figure 2.7: Momentum Distribution for ^3He , extracted from the asymptotic limit of $F(|\mathbf{q}|,y)$ [44]. The data were analyzed ignoring binding effects. See reference for more details.

to extract the momentum distributions provided that the binding correction, can be calculated or at least, estimated. A calculation of the spectral function is needed, the accuracy of which decreases with the increasing complexity and size of the nuclei [44].

Extracting Scaling Functions from Data To extract the scaling function $F(y, |\mathbf{q}|)$ from the measured data cross sections, we need a model of off-shell electron-nucleon cross sections. For this analysis, the we used the σ_1^{cc} formalism described by DeForest in [45]. In this prescription, the contribution to the cross section from a single bound and moving nucleon is given by:

$$\begin{aligned} \sigma_{(ep|en)} = & \frac{\sigma_{mott}}{\bar{E}E_N} \left\{ (F_1 + F_2) \cdot \left[\frac{\bar{Q}^2}{2} \tan^2 \frac{\theta}{2} + \frac{Q^2}{4q^2} (\bar{Q}^2 - Q^2) \right] + \right. \\ & \left. (F_1 + \frac{\bar{Q}^2}{4M^2} F_2) \cdot \left[\frac{Q^4}{4q^4} (\bar{E} + E_N)^2 + \left(\frac{Q^2}{q^2} + \tan^2 \frac{\theta}{2} \right) p'^2 \sin^2 \theta \right] \right\} \end{aligned} \quad (2.23)$$

where $\bar{E} = \sqrt{(\vec{p} - \vec{q})^2 + M^2}$, $Q^2 = q^2 - \nu^2$, $\bar{Q}^2 = Q^2 - (E' - \bar{E})^2$, and the Mott cross section is given by:

$$\sigma_{mott} = \frac{\alpha^2 (\hbar c)^2 \cos^2 \frac{\theta}{2}}{4E^2 \sin^4 \frac{\theta}{2}} \quad (2.24)$$

and F_1 and F_2 , the Pauli and Dirac form factors, are related to the Sachs nucleon form factors through the following relationships:

$$F_1^{(p|n)} = \frac{G_e^{(p|n)} + \tau G_m^{(p|n)}}{1 + \tau} \quad (2.25)$$

$$F_2^{(p|n)} = \frac{G_m^{(p|n)} - G_e^{(p|n)}}{1 + \tau} \quad (2.25)$$

$$\tau = \frac{Q^2}{4M^2} \quad (2.26)$$

To extract scaling functions from data, we use Eq. 2.18 and solve for $F(y, |\mathbf{q}|)$:

$$F(y, |\mathbf{q}|) = \frac{d^2\sigma}{dE'd\Omega} \cdot \frac{1}{Z\sigma_{ep} + N\sigma_{en}} \frac{|\mathbf{q}|}{\sqrt{M^2 + (\vec{p} + |\mathbf{q}|)^2}} \quad (2.27)$$

Table 2.1 lists the separation energies used in this data analysis for the various targets. This derivation of y -scaling using the PWIA demands the use of the minimum, rather than the average separation energies [46], which have been used in past analyses.

2.1.2 Other Scaling functions - Superscaling

The y -scaling described above has been called scaling of the first kind in literature [47]. This refers to the q -independence of the reduced response (in this case, the scaling function $F(y, |\mathbf{q}|)$, obtained from the measured cross section). To observe scaling of the second kind, it is necessary to incorporate the momentum scale of a given nucleus into the definition of the scaling variable and into the reduced response. Subsequently, the scaling that is observed is independent of the target nucleus - i.e.

all nuclei lie on the same scaling curve. Observation of both kinds of scaling is referred to as *superscaling*. Two superscaling variables are defined in Ref. [48], ψ and ψ' . The first variable, ψ , is equivalent to $y(E_s = 0)/k_F$ when the separation energy (Table 2.1) is not included in the calculation. On the other hand, ψ' does take the shift in energy (adjusted E_s value), which is chosen “empirically” (Table 2.2) by the authors of [48], into account and is then defined as:

$$\psi' = \frac{1}{\sqrt{\xi_F}} \frac{\lambda' - \tau'}{\sqrt{(1 + \lambda)\tau' + \kappa\sqrt{\tau'(\tau' + 1)}}} \quad (2.28)$$

with

$$\begin{aligned} \xi_F &= \sqrt{1 + \eta_F^2} - 1, \quad \eta_F \equiv \frac{k_F}{m_N} \\ \lambda' &\equiv \frac{\nu - E_{shift}}{2m_N} \\ \vec{\kappa} &\equiv \frac{\vec{q}}{2m_N} \\ \tau' &\equiv \kappa^2 - \lambda'^2 \end{aligned}$$

where the primed quantities have had the energy shift applied to them and ξ_F is a dimensionless scale of the fermi momentum relative to the nucleon mass, m_N . Similar to the y -scaling analysis, the superscaling function $F(\kappa, \psi)$ is extracted by taking the measured differential cross section and dividing out the single-nucleon elastic cross section (see Eq.13 in [48]).

It is then also possible to extract additional superscaling functions, $f_T(\psi')$ and $f_L(\psi')$, when the separated transverse and longitudinal contributions to the cross

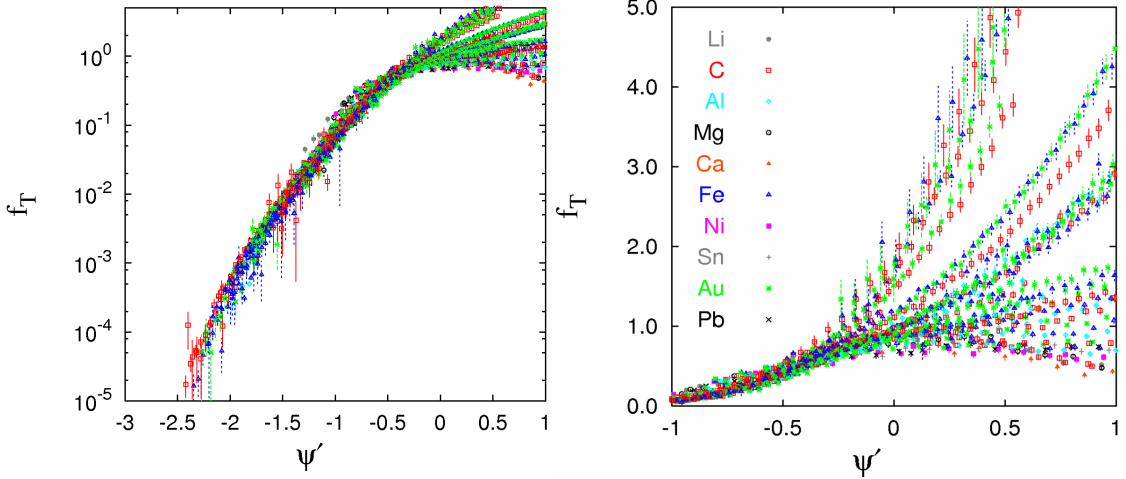


Figure 2.8: Transverse Scaling function, f_T for a variety of nuclei and kinematics extracted here [48]. The longitudinal contribution has been subtracted using a superscaling model discussed in the same publication.

section are available. Fig. 2.8 shows the transverse superscaling function extracted for data from a variety of experiments [48]. For the kinematic coverage of E02-

Table 2.2: Adjusted Separation Energies and Fermi momenta used in the extraction of superscaling functions [48]. The answers are especially sensitive to k_f^{adj} .

Target	$E_s^{adjusted}$ (MeV)	$k_f^{adjusted}$ (MeV/c)
^4He	15	200
^{12}C	20	228
^{63}Cu	23	241
^{197}Au	25	245

019, the longitudinal contribution is negligible, so the entire response is taken to be transverse. It is important to note that the extracted superscaling functions are extremely sensitive to the input values of k_F and the use of conventional values, which differ by as little as 10 MeV from the values given in Ref. [48] will prevent superscaling

from being observed.

2.1.3 Other Scaling variables - y_{cw}

As was discussed in Sec. 2.1.1, the (A-1) nucleus can be left in an excited state and therefore a non-zero binding correction exists. This means that y , which is the longitudinal momentum, is quite different for weakly bound nucleons than for strongly bound ones. As a result, the scaling function is not necessarily related to the longitudinal momentum for large negative values of y , where the response is dominated by the electron scattering from strongly bound, correlated nucleons. An alternate scaling variable, y_{cw} , was introduced by Ciofi degli Atti and Faralli [49] with the hope of being able to represent the longitudinal momenta of weakly and strongly bound nucleons equally well. This definition includes the excitation energy of the daughter nucleus (A-1), which is a function of the relative momentum of the correlated pair and its momentum in the CM frame and is given by [49]:

$$\langle E_{A-1}^*(k) \rangle \simeq \left(\frac{A-2}{A-1} \right) \frac{\mathbf{k}^2}{2M} + b_A - c_A |\mathbf{k}| \quad (2.29)$$

where the parameters b_A and c_A describe the CM motion of the correlated pair. Additionally, this energy is shifted by the average shell-model removal energy, $\langle E_{gr} \rangle$, which is obtained using the Koltun [50] sum rule. The new scaling variable, y_{cw} , is

then

$$y_{cw} = \frac{\tilde{q}}{2} + \sqrt{\frac{\tilde{q}^2}{4} - \frac{4\nu_A^2 M^2 - W_A^4}{4W_A^2}} \quad (2.30)$$

where $\nu_A = \nu + 2M - E_{th}^{(2)} - b_A + \langle E_{gr} \rangle$, $E_{th}^{(2)}$ is the two-body break-up energy, $W_A^2 \equiv \nu_A^2 - q^2$, and $\tilde{q} = q + c_a \nu_A$. At low values, y_{cw} approximately reduces to the usual scaling variable, y .

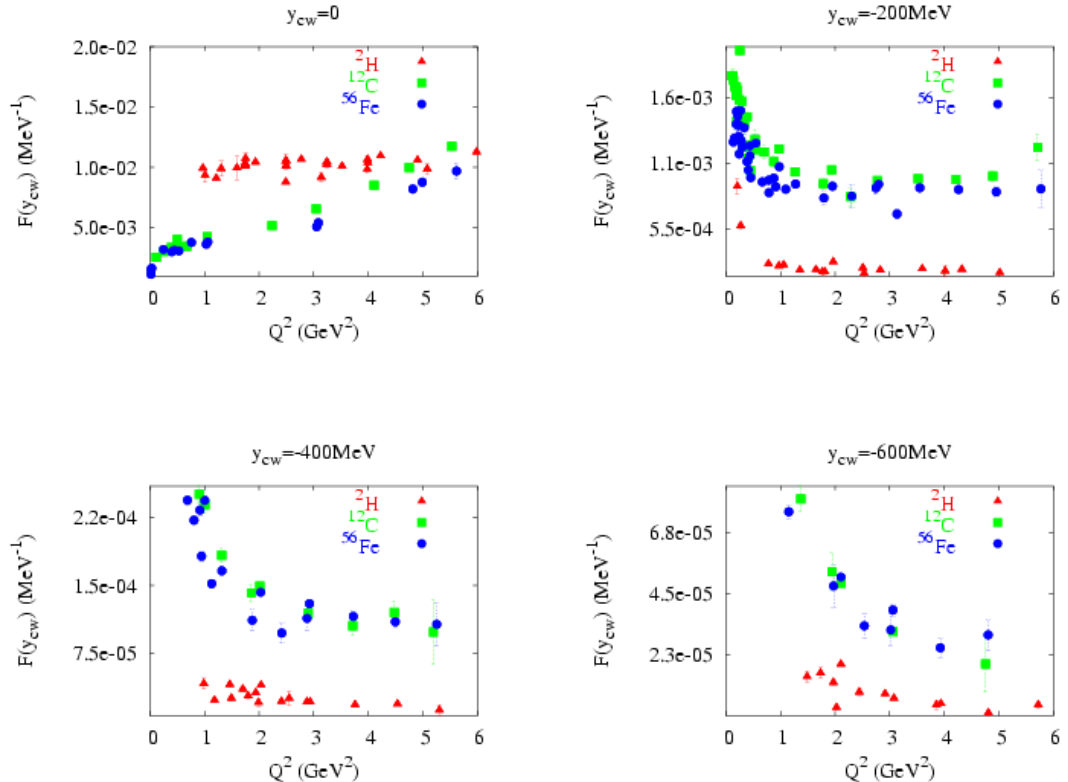


Figure 2.9: The scaling functions of ^2H , ^{12}C , and ^{56}Fe for existing quasi-elastic world data plotted for fixed values of y_{cw} as a function of Q^2 . Scaling is approached from above (decreasing $F(|\mathbf{q}|, y)$ with increasing Q^2), which is also the case with y , suggesting that the main scale-breaking mechanism is FSIs.

Using y_{cw} allows us to establish a more direct link between the scaling function

and the nucleon momentum distributions as well as to disentangle the contributions from binding effects and FSIs. The binding effects are taken into account in the definition of the new scaling variable, y_{cw} , rather than as an additional calculated correction to the scaling function.

Another useful feature of this scaling variable is that it allows one to obtain scaling functions for heavier nuclei by scaling up the deuteron's $F(|\mathbf{q}|, y_{cw})$ by a target-specific constant, C_A [49].

The data, when analyzed using y_{cw} , Fig. 2.9, clearly shows the approach to scaling from above, indicating the fall-off of FSI effects with increasing values of Q^2 , as is the case with y .

2.2 Inelastic Cross section

In inclusive inelastic electron nucleus scattering, the only information available about the final state is its invariant mass,

$$W^2 = M^2 + 2M\nu - Q^2. \quad (2.31)$$

The most general expression for an inclusive cross section is:

$$\frac{d^2\sigma}{dE'd\Omega} = \frac{\alpha^2}{Q^4} \frac{E'}{E} L_{\mu\nu} W^{\mu\nu}, \quad (2.32)$$

where $L_{\mu\nu}$ and $W^{\mu\nu}$ are the leptonic and hadronic tensors, respectively. Using the target tensor as given in [51], it can be shown that the unpolarized cross section for electron scattering from a nuclear target is then:

$$\frac{d^2\sigma}{dE'd\Omega} = \frac{d\sigma}{d\Omega_{Mott}} \left[W_2^A(\nu, Q^2) + 2W_1^A(\nu, Q^2) \tan^2 \frac{\theta}{2} \right] \quad (2.33)$$

Thus, the inelastic cross section is characterized by two structure functions, W_1^A and W_2^A , which are functions of momentum and energy transfers:

$$\begin{aligned} \nu &= E - E' = \frac{\vec{q} \cdot \vec{p}}{M} \\ Q^2 &= -q^2 = 4EE' \sin^2 \frac{\theta}{2}, \end{aligned} \quad (2.34)$$

both of which are evaluated in the lab frame.

The nuclear structure functions can be related to the spectral function and the nucleon structure functions in the following way: [52]

$$\begin{aligned} W_1^A(Q^2, \nu) &= \int d^4p_0 S'(E_0, p_0) \left(\frac{M}{\tilde{p}_0} \right) \left[W_1^N + \frac{W_2^N}{2M^2} \frac{|\mathbf{p}_0 \times \mathbf{q}|^2}{|\mathbf{p}_0|^2} \right] \\ W_2^A(Q^2, \nu) &= \int d^4p_0 S'(E_0, p_0) \\ &\times \left\{ W_1^N \frac{q^2}{|\mathbf{q}|^2} \left(\frac{q^2}{\tilde{q}^2} - 1 \right) + \frac{W_2^N}{M^2} \left[\frac{q^4}{|\mathbf{q}|^4} \left(\tilde{E}_0 - \tilde{\nu} \frac{\tilde{q} \cdot \tilde{p}_0}{\tilde{q}^2} \right) - \frac{q^2}{|\mathbf{q}|^2} \frac{|\mathbf{p}_0 \times \mathbf{q}|^2}{|\mathbf{p}_0|^2} \right] \right\} \end{aligned} \quad (2.35)$$

The quantities denoted with tilde refer to the free nucleon, rather than the bound one. For a detailed explanation, refer to [52]. In the limit of high energy and

momentum transfers, the nucleon structure functions are reduced to being functions of $x = \frac{Q^2}{2M\nu}$, which is the fraction of the total momentum of the nucleon that is carried by the struck quark. In this limit, the structure function is related to the momentum distribution of the quarks, which is different than that of quarks in a free nucleon due to presence of other nucleons.

Our analysis of the inelastic electron-nucleon cross section is done through the study of the F_2 structure function, which can be extracted from the data provided that the ratio, R , of the longitudinal cross section to the transverse cross section is known. Using a simple parametrization of $R = 0.32\text{GeV}^2/\text{Q}^2$ [53], we can extract F_2^A :

$$F_2^A = \frac{d^2\sigma}{d\Omega dE'} \cdot \frac{\nu}{\sigma_{mott}[1 + 2 \tan^2(\frac{\theta}{2}) \frac{1+\nu^2/Q^2}{1+R}]} \quad (2.36)$$

Scaling of F_2^A has been observed as a function of x in the deep inelastic region, as discussed previously (see Sec. 1.3).

2.2.1 ξ -scaling

Inclusive electron nucleus data can also be analyzed in terms of the Nachtman variable, $\xi = \frac{2x}{1+\sqrt{1+4M^2x^2/Q^2}}$, which is analogous to x in that it is the fraction of the nucleon momentum carried by the struck quark, but target mass effects are not neglected [54]. In the $Q^2 \rightarrow \infty$ limit, ξ reduces to x . This means that the scaling of the structure functions that is observed in x in the deep inelastic region should also be observed in ξ in the same kinematic region. When the data were examined

in this way [34], approximate ξ -scaling was observed for all values of ξ , including the quasielastic region where it was not expected. One explanation [55] of this scaling in ξ was through the observation that ξ can be expanded as a function of y at high values of Q^2 , so data can be expected to show the same kind of scaling in ξ as it does in y in a purely quasi-elastic kinematic region. The authors suggest that the relationship between the two scaling variables masks the presence of Final State Interactions at high x and the observed ξ scaling is an accident. This explanation is not very satisfying, as the reduced responses ($F(|\mathbf{q}|, y)$ and F_2^A) are obtained in different ways and do not represent the same quantity, so the fact that the variables in which they scale can be related to each other is not very illuminating. Local duality [58, 59] has been suggested as another explanation for the observation of ξ scaling. When the structure function νW_2 is examined in terms of the dimensionless variable $w' = 1/x + M_N^2/q^2$ or ξ , it is found to have the same Q^2 behavior as the resonance form factors. In fact, averaging over the resonance peaks produces the scaling curve for the structure functions. The resonance peaks do not disappear with increasing values of Q^2 , but decrease in strength and move to lower values of w' (higher ξ), following the magnitude of the scaling limit curve. For ξ -scaling, this means that the scaling curve observed at large values of ξ is due to the local averaging of the resonances by the momentum distributions of the nucleons in the nucleus. Recall that Bloom and Gilman proposed that the resonances are not a separate entity, but are an intrinsic part of the scaling behavior and there's a common origin for both phenomena.

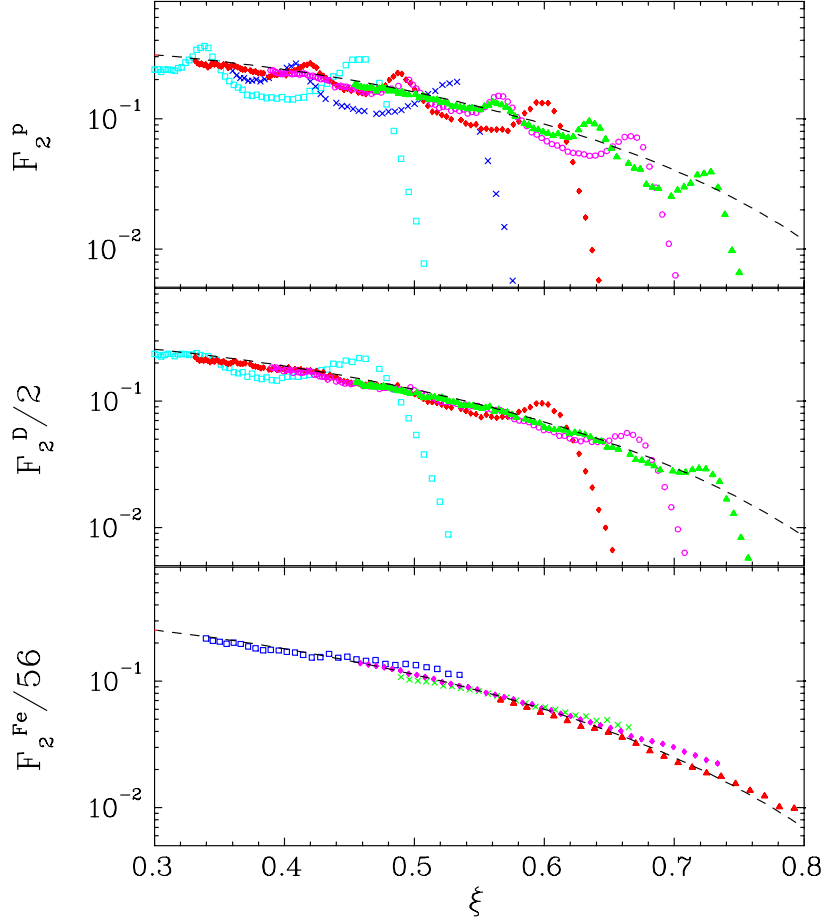


Figure 2.10: F_2/A vs ξ for H (top), ^2H (middle), and ^{56}Fe (bottom) along with the MRST [56] parametrization of the structure functions. For ^{56}Fe , the quasielastic peak was removed with a $W^2 > 1.2 \text{ GeV}^2$ cut. Figure from [57]

And, the final explanation for the observed ξ -scaling [60] proposes that it's purely accidental. At high ξ and low Q^2 , the DIS and resonance contributions fall at approximately the same rate as the quasielastic contribution grows and as a result, scaling is observed over the whole range of ξ . At high values of ξ , the growing contribution from DIS and the resonances compensates for the fall-off of the quasielastic contribution, which has a strong Q^2 -dependence coming from the form factors. These are unrelated

reaction mechanisms and, when their contributions are examined separately, they do not scale over the entire range of ξ , as can be seen in Fig 2.11.

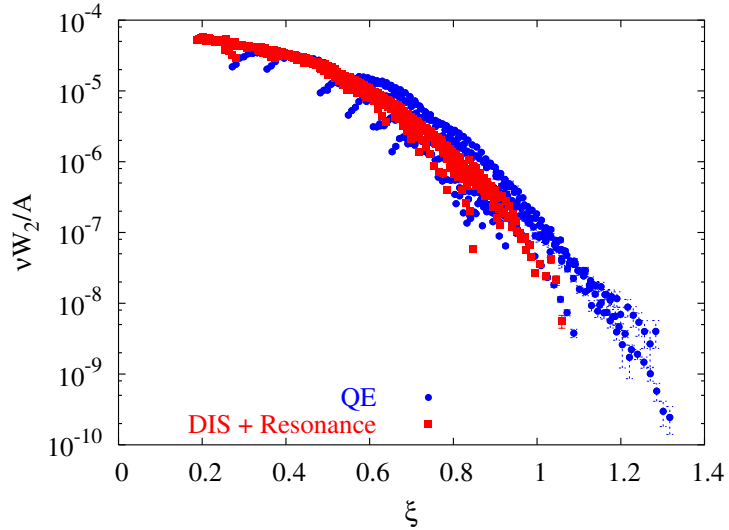


Figure 2.11: νW_2^A per nucleon for ^{197}Au as a function of ξ with the quasielastic contribution subtracted (red squares) and with the DIS/resonance contribution subtracted (blue circles). $0.5 < Q^2 < 5.75$ (GeV^2) at the quasielastic peak. Note that neither contribution scales over the whole range in ξ . Data shown is from SLAC experiment NE3 and from JLab experiment E89-008 [42].

2.2.2 Final State Interactions

In the limit of large energy and momentum transfers, the reduced cross section is expected to scale in both the quasi-elastic and inelastic regimes, although in different variables. This expectation is partly based on the assumption that the reaction is well described by the exchange of a single virtual photon with a single nucleon that does not react with the A-1 nucleus. However, final state interaction contributions to the cross section can arise from the interaction between the struck object and the

remainder nucleus. It is thought that the inclusive cross section is only sensitive to these FSIs taken place within a distance of $\approx 1/|\mathbf{q}|$, implying that the inclusive cross sections at large momentum transfer should have little effect from FSIs. The data tell a different story.

Existing data show y -scaling violations for heavy targets, which suggests that the PWIA regime has not been reached. Previous analyses [61] have suggested that most of the strength in the $x > 1.4$ region is due to the electron scattering from a low-momentum nucleon and that nucleon's FSIs with the A-1 nucleus. O.Benhar's calculations [62] show that the contributions from FSIs decrease and approach a limit with increasing Q^2 values, but never vanish.

Another school of thought [63] states that since scattering in the $x > 1.4$ region takes place from correlated nucleons, the FSIs are confined to the correlation: i.e. the struck nucleon interacts only with the other nucleon(s) in the correlation. This means that while FSIs exist, they will cancel out in the cross section ratios of heavy nuclei to light ones.

Consensus has not been reached on the Q^2 - and A -dependence of the FSIs. While E02-019 will not resolve this issue, its vast data set will contribute greatly to the discussion.

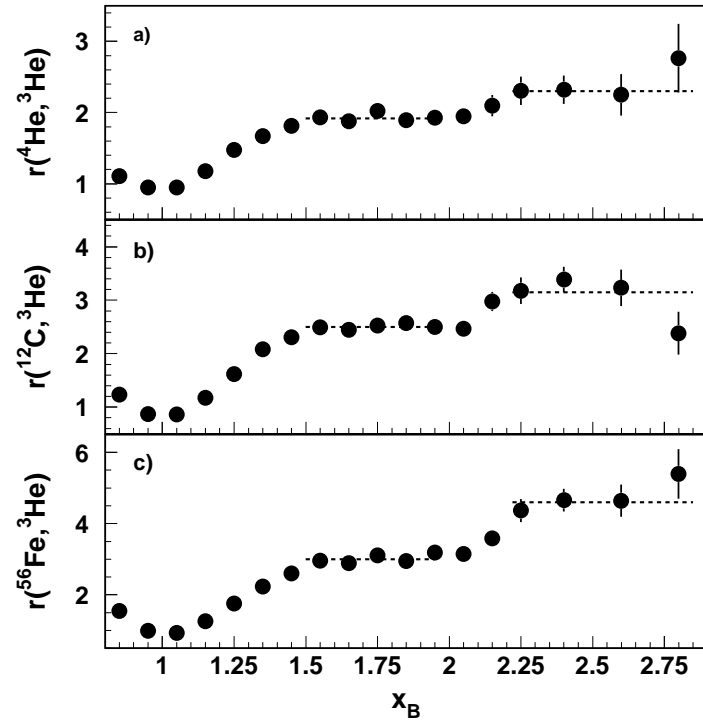


Figure 2.12: Ratios of ^4He , ^{12}C , and ^{56}Fe to ^3He , respectively [64]. The plateaus at $1.5 < x < 2$ and $2.25 < x < 3$ correspond to scattering from 2N- and 3N- correlations, respectively.

2.2.3 Short Range Correlations

A large contribution to the cross section at $x > 1$ comes from the interaction of the virtual photon with a nucleon in a correlated pair. When the interaction distance between the nucleons becomes smaller than the average inter-nucleon spacing, the repulsive NN force imparts high momenta on these nucleons. The ideal regime for studying SRCs is one in which scattering from low momentum nucleons is suppressed and the energy transfer is higher than the kinetic energies of correlated nucleons, i.e. at $x > 1$ and $Q^2 > 1$. At the high momentum kinematics, where the mean field contribution is negligible, the inclusive cross section can be approximated with terms that describe scattering from nucleons in multi-nucleon correlations:

$$\sigma_A(x, Q^2) = \sum_{j=2}^A \frac{a_j(A)}{j} \sigma_j(x, Q^2) \quad (2.37)$$

where $\sigma_A(x, Q^2)$ is the electron-nucleus cross section and $\sigma_j(x, Q^2)$ is the electron- j -nucleon-correlation cross section ($\sigma_j(x, Q^2) = 0$ for $x > j$), and $a_j(A)$ is proportional to the probability of finding a nucleon in a j -nucleon correlation [63]. For normalization purposes, σ_2 and σ_3 are taken to be the cross sections for electron scattering from deuterium and ^3He , respectively and are expected to be closely related to the number of 2- and 3- nucleon pairs in nuclei. Cross section ratios of heavy nuclei to light nuclei are expected to scale (show no dependence on Q^2 or x in a given x -range) if the process is dominated by scattering from j -nucleon correlations and the j -nucleon

correlations in $A > j$ nuclei are similar to those in the $A = j$ nuclei.

Previous measurements have shown the presence of both 2- and 3-nucleon correlations at low values of Q^2 as is shown in Fig. 2.12.

Chapter 3

Experimental Details

3.1 Overview

Experiment E02-019, “Inclusive Electron Scattering from Nuclei at $x > 1$ and High Q^2 with a 6 GeV beam”, was performed in experimental Hall C of the Thomas Jefferson National Accelerator Facility (TJNAF) in the fall of 2004. All three experimental halls were operational during the running of E02-019. Inclusive scattering of 5.767 GeV electrons from Deuterium, 3 Helium, 4 Helium, Beryllium, Carbon, Copper, and Gold was measured in the High Momentum Spectrometer (HMS) at 6 scattering angles and several HMS momentum settings. Hydrogen data was taken for the purposes of calibration and normalization.

3.2 Accelerator

For E02-019, CEBAF supplied Hall C with a continuous wave (CW) electron beam of 5.767 GeV (highest energy available) at currents as high as $80\mu\text{A}$. The accelerator complex (Fig. 3.1) consists of an injector, two superconducting linacs, 9 recirculation arcs, a Beam Switch Yard (BSY) and the three experimental halls (A, B, and C). The electrons are injected into the North Linac at 67 MeV, where they're accelerated 570 MeV by superconducting radio frequency cavities, bent through the east arc, and accelerated an additional 570 MeV in the South Linac. At this point, the electron beam can be extracted to any one of the three experimental halls through the BSY or be sent back through the west arc for as many as 5 total acceleration passes and a maximum beam energy of 5.767 GeV. The electrons can be extracted at the end of any pass, providing a beam energy equal to the injector energy plus a multiple of the linac energy.

As mentioned above, the electrons are accelerated in the linacs using superconducting radio frequency cavities tuned to 1497 MHz. The cavities, which are phased for maximum acceleration, are kept at 2 Kelvin using liquid helium from the Central Helium Liquefier (CHL). The beam has a structure that consists of 1.67 ps pulses coming at 1497 MHz, meaning that each hall receives a 499 MHz beam, or a third of all the pulses. Three beams of different energies and different currents can be delivered into the halls simultaneously.

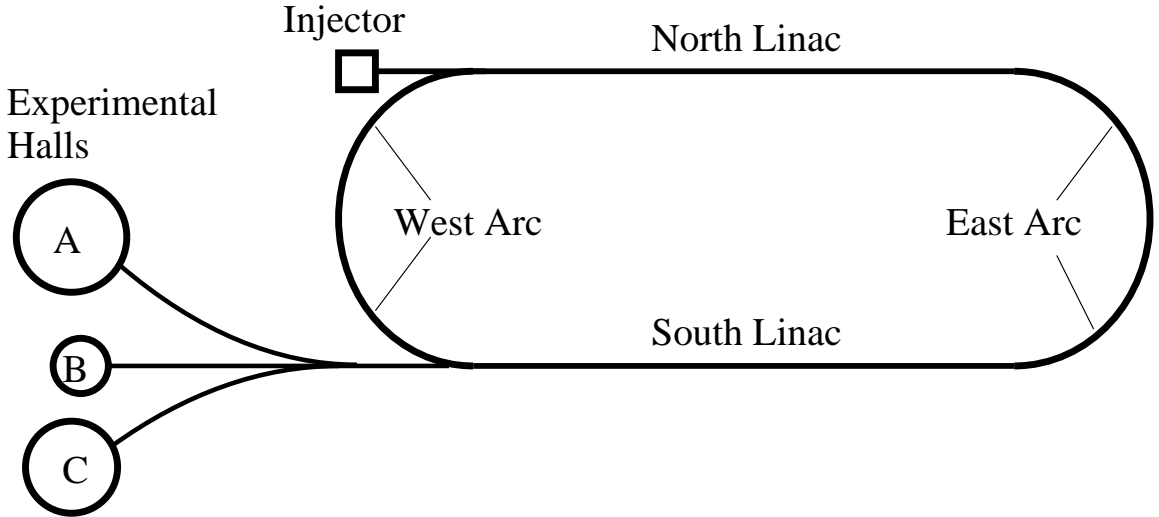


Figure 3.1: Overhead Schematic of the Accelerator and the experimental halls

3.3 Hall C Beamlne

Once the beam arrives at the BSY, it is sent through the Hall C arc and into the hall. The Hall C beamlne consists of 8 dipoles, 12 quadrupoles, 8 sextupoles, which are used to focus and steer the beam. The arc is equipped with several devices to measure the profile, energy, position, and the current of the beam. Figure 3.2 shows the described hardware in the Hall C Arc and beamlne.

3.3.1 Beam Energy Measurement

The beam energy measurement was performed by using the Hall C Arc magnets as a spectrometer [65]. The position and direction of the beam are determined at the entrance and at the exit of the 34.3° bend of the Hall C Arc line by 2 pairs of high resolution harps (wire scanners). A harp is made up of 3 wires, two of which are

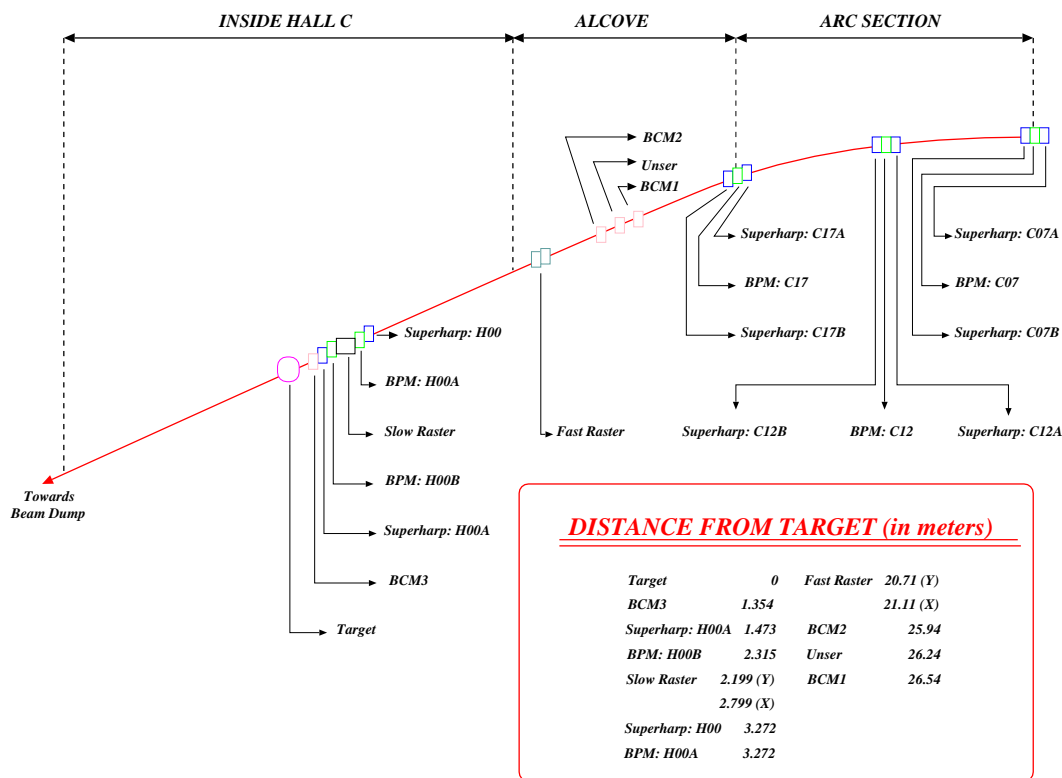


Figure 3.2: Hall C Beamlne and Hardware. See text for details.

oriented vertically and one horizontally. All magnetic elements except for the dipoles are turned off during this measurement. The beam is steered so that it follows the central ray of the magnets in the arc. Then, the beam momentum (and therefore, energy) can be determined as a function of the current in the arc dipoles:

$$E \simeq p = \frac{e}{\theta} \int \vec{B} \cdot \vec{dl}, \quad (3.1)$$

where θ is the arc bend angle, e is the electric charge, and $\int \vec{B} \cdot \vec{dl}$ is the magnetic field integral over the path of the beam. For this measurement, a precise field map of at least one arc magnet is required. One of the arc dipoles has been precisely mapped and the others are assumed to have the same field map, normalized to the central field value. With this information in hand, the incident beam energy can be measured with an uncertainty of $\delta p/p \approx 2 \times 10^{-4}$.

The beam energy measurement was performed twice during the running of E02-019 with agreement of $< 0.0007\%$ between the two results. The measurements gave beam energies of $5.76713 \text{ GeV} \pm 1.65 \text{ MeV}$ and $5.76717 \pm 1.65 \text{ MeV}$, respectively.

3.3.2 Beam Position Monitors

During the running of E02-019, the position and trajectory of the beam were monitoring using 3 Beam Position Monitors (BPMs): H00A, H00B, and H00C. However, only 2 of them performed reliably (H00C did not). The BPMs are cavities with four antennae (rotated $\pm 45^\circ$ from the horizontal and vertical directions to minimize synchrotron

damage), sensitive to the relevant harmonic frequency. The beam pulse frequencies in the accelerator and in Hall C are harmonics of the fundamental frequencies of the BPMs. The amplitude of the signal from each antenna can be related to the distance between the beam and that antenna. Relative beam positions in combinations with superharp measurements can be used to calculate the absolute beam position. More information is available in Ref. [66].

Table 3.1: Nominal Beam positions for E02-019

BPM	Nominal x-pos (mm)	Nominal y-pos (mm)	Distance from target (m)
H00A	0.80	-1.83	3.272
H00B	0.48	-1.50	2.315
H00C	0.48	-1.08	1.360

The BPM readouts were closely monitored by the shift workers during the running of the experiment. The positions were kept to within 0.1mm of the nominal positions for each BPM (Fig.3.1) to make sure that the beam went through the center of the target and the target thickness (traversed by the beam) remained constant from run to run. The nominal position of the beam was calculated using a sieve slit run, where a HEAVYMET collimator (Tungsten with 10% CuNi) with grid of apertures is placed in front of the HMS to let the particles through. This was done by steering the beam until the HMS axis and the beam axis intersected which was achieved when the sieve slit pattern is centered about the central aperture, which is smaller than the others, see Fig.3.3. Using the position of the central aperture from the calibration run in

combination with the locations of the BPMs, the nominal beam position coordinates for the BPMs can be calculated.

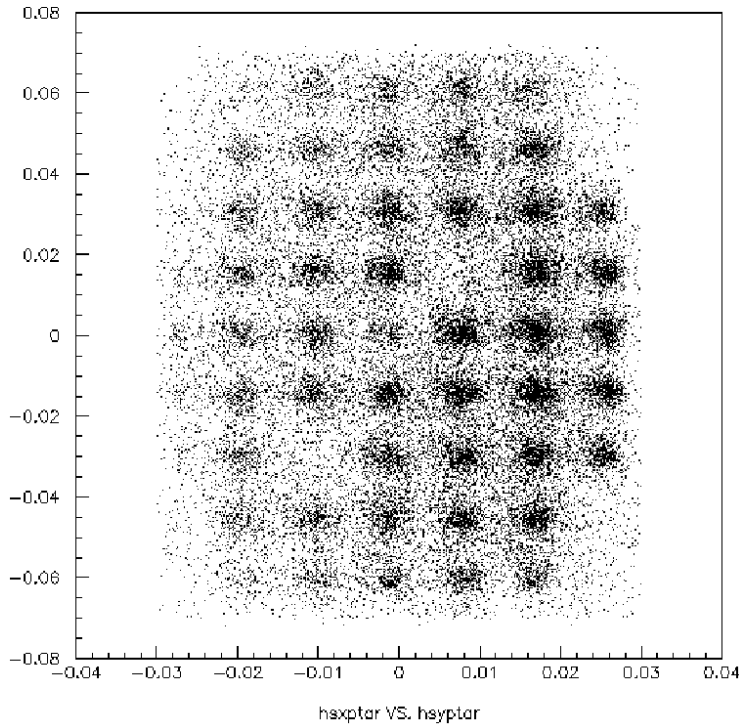


Figure 3.3: Sieve Slit Pattern. The nominal beam position was achieved so that the pattern is centered about the small aperture at $xptar, yptar = 0$, where $xptar$ and $yptar$ are the out-of-plane and in-plane angles with respect to the central ray. Detailed descriptions of the target quantities can be found in Sec. 4.1.

3.3.3 Beam Current Monitors

The current of the electron beam in the hall was measured using 2 microwave cavity Beam Current Monitors (BCM1 and BCM2) and a parametric current transformer (Unser monitor). The BCMs are resonant cavities of a design similar to the previously described BPMs. The antennae pick up the signal that is proportional to the beam

current for all resonant modes of the cavity, but for certain modes (TM_{010} mode), the signal is relatively insensitive to beam position. One can make the cavity sensitive to this mode by adjusting its size and selecting the resonant frequency to be identical to the accelerator RF frequency. Then, the BCM cavity is excited to this mode when the electron beam passes through it and the beam current can be measured by analyzing the signal picked up by the cavity antennae.

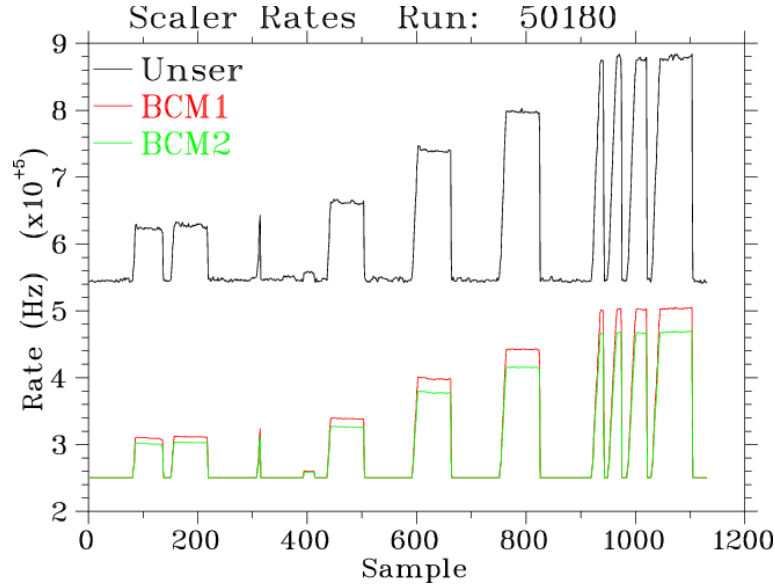


Figure 3.4: BCM Calibration run consisting of alternating periods of beam on and off with increasing current during each beam on period. Short beam-on periods centered around sample 1000 are not used in the calibration as they're too short and a result of beam trips.

The Unser monitor consists of an active current transformer and a magnetic modulator, linked together in a feedback loop. The toroid which is the main current sensor, carries two windings which close the feedback loop of the operational amplifier. This amplifier maintains the balance between the primary and feedback currents.

The error in the balance between these currents is detected and corrected for by a magnetic modulator-demodulator circuit consisting of a pair of toroidal cores. The output signal voltage, proportional to the beam current is measured with a precision resistor from the feedback current [67].

The Unser has a stable and well measured gain, but large drifts in its offset and therefore, is not used to measure the beam current. There were 17 BCM calibration runs taken over the course of the experiment. The calibration runs were about an hour long and consisted of alternating beam on and beam off periods of 2 minutes each, with the beam current increasing for every beam on period until a current of $\approx 100 \mu\text{A}$ was reached (Fig. 3.4), and then the current was decreased during the remaining beam on periods. During the beam off periods, the offsets of the Unser and the BCMs can be determined, and the beam on periods can be used to calibrated the gains of the BCMs using the well-known gain of the Unser and its measured offset. The data from all the calibration runs were combined into one calibration file, and a Hall C calibration program was used to select stable intervals within each beam on and beam off period. Normally, all the beam off periods are averaged over, but since there was concern about the Unser zero drifting over the hour-long run, the beam off periods were used on either side of a beam-on period. The residuals from each calibration run when compared to the global fit can be seen in Fig.3.5 and display a nice scatter around zero without any outliers or trends. Residuals vs current also showed no systematic trends.

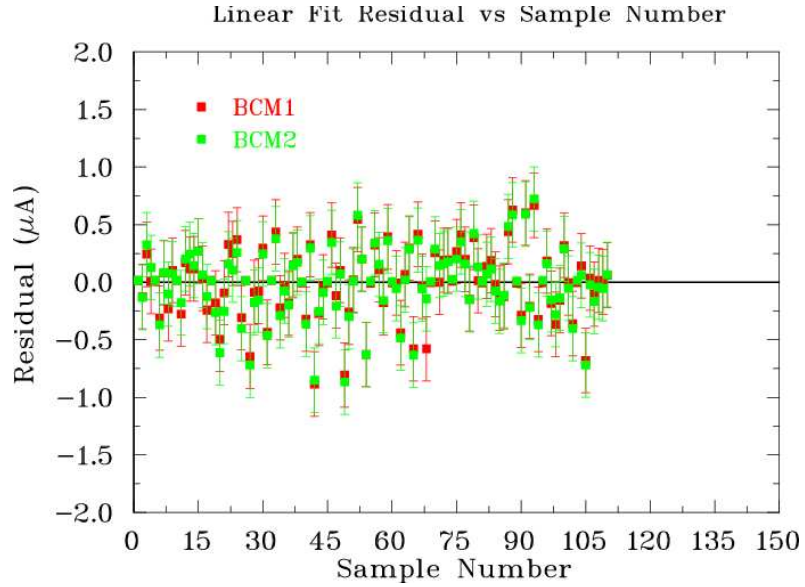


Figure 3.5: BCM Calibration: Residuals for each run compared to the global fit as a function of sample number (equivalent to time).

A more detailed and complete description of both the BCM and Unser monitors can be found in C.S. Armstrong's thesis [68].

There are several sources of systematic uncertainties on the measurement of the charge. The stability of the gain on BCM 2 (which was used in data analysis) is taken to be good to 0.2%. The uncertainty in the Unser zero is taken to be 250nA (see Sec. 4.3.4), for an additional 0.3% uncertainty. Finally, the measurement is sensitive to temperature, which yield another 0.2% uncertainty [33]. The total systematic uncertainty on the charge measurement is 0.5%, with a 0.4% scale uncertainty and 0.3% relative uncertainty.

3.3.4 Beam Raster System

The E02-019 experiment was performed with a beam current of $\sim 80\mu\text{A}$, with the exception of Aluminum data, which were taken at $\sim 35\mu\text{A}$. This is large enough that the cryogenic liquid targets can be overheated by the deposited energy of the beam and bubbles can be formed, resulting in non-uniform target density [69]. To minimize this effect, as well as to avoid damaging the beam dump window, the beam was rastered, which increases the effective spot size and reduces the energy density.

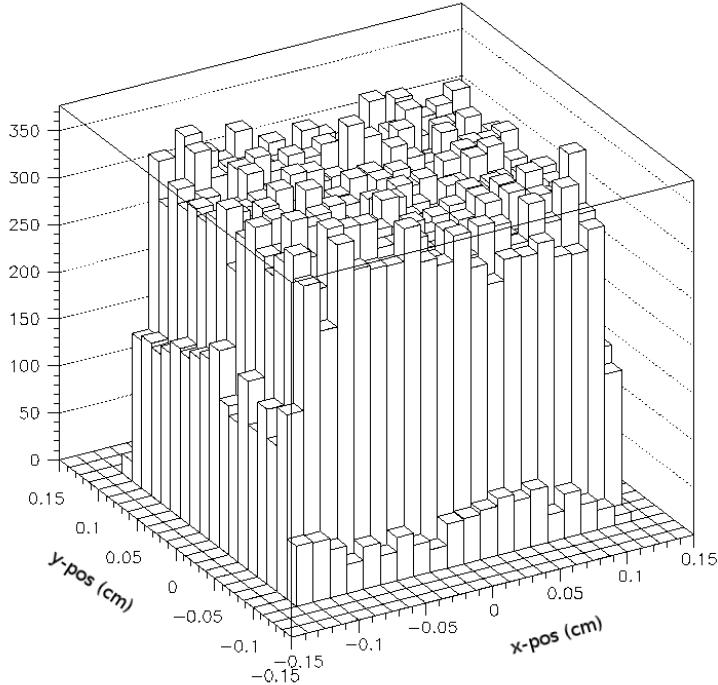


Figure 3.6: Beam Profile with the fast raster turned on. The beam was rastered in both horizontal and vertical directions to avoid melting or boiling of the target.

The fast raster system consists of 2 sets of steering magnets and is located 20m

upstream of the target. The first set rasters the beam in the vertical direction and the second in the horizontal. Until recently, a Lissajous raster pattern was in place. The waveform of the magnet current was sinusoidal, and it slowed down as it approached its peak before reversing direction at the edge of the scan region. This caused more energy to be deposited at the edges, reducing the effectiveness of the raster. In August of 2002, a linear raster system [70] went into operation. The waveform of the new raster system is triangular, resulting in a uniform rectangular shape on the target. The design of the new system had two main goals: to maximize linear velocity and to minimize the turning time. In comparison to the Lissajous raster, the linear raster has a highly homogeneous density distribution over the entire raster region with 98% linearity, 95% uniformity, and 1000m/s linear sweep velocity. The turning time at the vertex of the raster pattern is ≈ 200 ns and the beam traversal time from one edge to another is 20 μ s. The beam 2mm \times 2mm raster pattern can be seen in Fig. 3.6 and is highly uniform.

3.4 Targets

Experiment E02-019 was run with 4 cryogenic (H, 2 H, 3 He, 4 He) and 4 solid (12 C, Be, Cu, and Au) targets. The targets were arranged on a ladder that was remotely controlled by the target operator during the run. The cryogenic targets were contained in Aluminum cells, so the detected electrons could have scattered from either the cryogenic target or the cell. In order to allow a measurement of the contribution

from the container cell, a dummy target was also placed onto the target ladder. Since the target ladder only had space for 3 cryo target cells and one was kept as a spare, there were 2 running periods, with helium data taken during one and hydrogen and deuterium data taken during the other. The systematic uncertainties in the

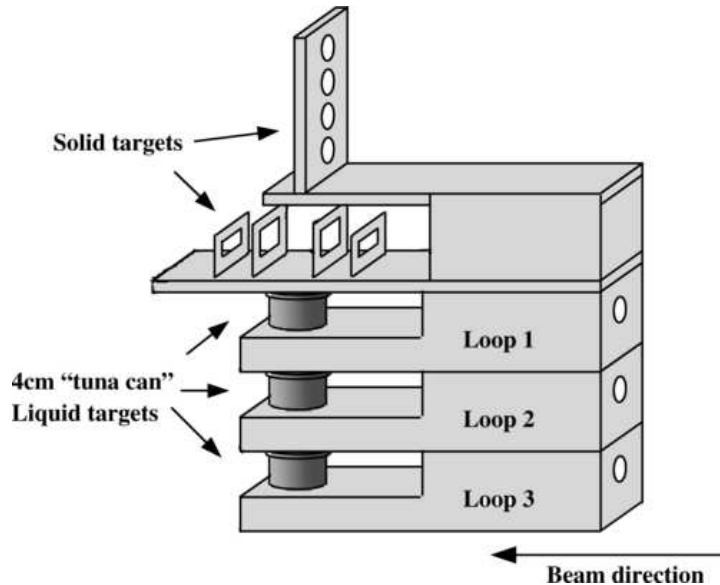


Figure 3.7: Hall C Target ladder.

thicknesses of the solid targets are given in Table 3.2. These are normalization, or scale uncertainties and have no kinematic or time dependence, unlike those for the cryogenic targets, discussed in the next section.

3.4.1 Cryogenic Targets

The cryogenic targets were each held inside of a cylindrical “tuna-can” Al cell with thin walls. The can was oriented vertically (Fig. 3.7), so that horizontal changes in the beam position correspond to changes in the effective target thickness. Accurate

Table 3.2: Systematic uncertainties in the target thicknesses for solid targets.

Target	Uncertainty
⁹ Be	0.5%
¹² C	0.5%
⁶³ Cu	1.0%
¹⁹⁷ Au	2.0%

knowledge of the effective target thickness is vital to the extraction of the cross sections. To measure the target thickness, we need precise measurements of the dimensions of the target cell as well as corrections for the thermal contraction as the dimensions were measured at room temperature. The target ladder as well as the elements on it can move relative to each other during the cooling process and the beam positions may be offset from the center-beam line. Finally, the densities of the cryogenic targets can change with time if there are any leaks in the loops.

The cryotarget has three separate loops in it, each attached to short (4 cm diamter) cell. Even though all three loops can be used at any given time, only 2 were filled with cryogenic materials for this experiment, with the third being left empty as a possible spare. A loop consists of a target cell, a re-circulation fan, heat exchangers and 700W heater (Fig. 3.8). The coolant flow to the loops is controlled by the target operator through Joule Thompson (JT) valves. The coolant, 15K helium for H/²H and 4K helium for ³He/⁴He running, comes through the heat exchanger, where the target material is cooled. The cooled material moves continuously between the heat exchanger and the target cell. The target heater is used to maintain a constant heat

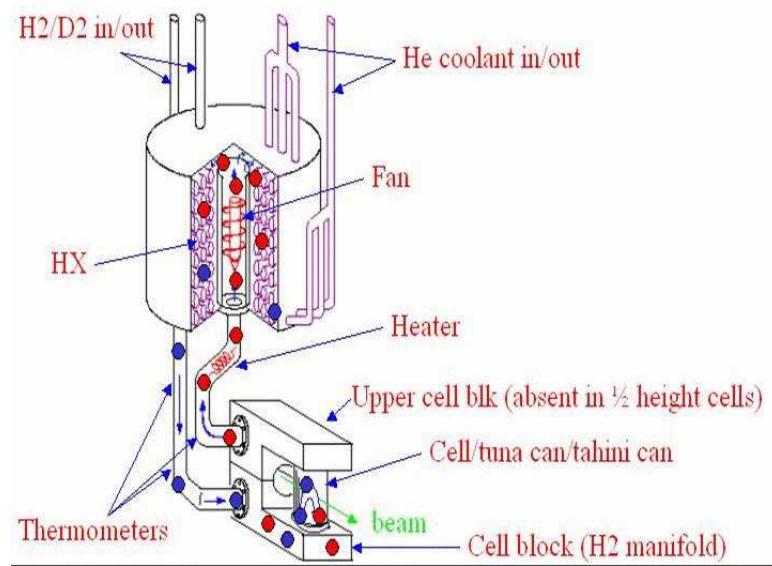


Figure 3.8: Detailed view of a cryotarget loop and its components

load on the target, so that the cooling power doesn't change as the beam current changes.

For E02-019, the H and ^2H targets were operated at 19K, 23 Psia and 22K, 23 Psia, respectively. The helium targets had small leaks, which were corrected for, but their nominal operating parameters were 5.8K at 117 Psia and 6.2K at 182.5 Psia for ^3He and ^4He , respectively.

The dimensions of the three cryogenic cells are listed in Table 3.3 and were measured and compiled by David Meekins [71] from the JLab target group. The thermal contraction of the cells is determined from the final temperature of the loops and the contraction of Aluminum, whose contraction factor becomes relatively independent of temperature below 25K. The cryotargets were operated below this threshold temperature and the contraction factor was found to be 0.996 for the three loops.

Table 3.3: Geometry of the Cryogenic Target Loops. The outer diameter (OD) includes the cell walls.

Loop	OD(mm)	Wall 1 (mm)	Wall 2 (mm)	ID - warm (mm)	ID - cold (mm)
1	40.13±0.08	0.1384±0.0013	0.1270±0.0013	39.86±0.08	39.69±0.08
2	40.18±0.08	0.1219±0.0013	0.1219±0.0013	39.94±0.08	39.77±0.08
3	40.16±0.08	0.1232±0.0013	0.1194±0.0013	39.92±0.08	39.75±0.08

Once cooled down, the target ladder was offset by 2.5 mm beam right, with an additional 1 mm offset that occurred after the target chamber was evacuated. The nominal beam position was calculated to be 1.1 mm beam left. These offsets (4.6 mm) were taken into account when the target thickness was being calculated in addition to each cryo-cell's offset from the axis of the target ladder. (Table 3.5).

Table 3.4: Target Thicknesses for E02-019. Note that the numbers listed for the helium target thicknesses assume no leaks and the actual thicknesses were calculated on a run-by-run basis. Radiation lengths include only the target materials, not their containers.

Target	Thickness (g/cm ²)	Radiation Length (%)
H	0.2828	0.463
² H	0.6525	0.535
³ He	0.2769	0.429
⁴ He	0.5285	0.429
⁹ Be	1.8703	2.870
¹² C	0.6667	1.561
⁶³ Cu	0.7986	6.210
¹⁹⁷ Au	0.3795	5.875

If the beam path does not go directly through the center of the target of radius

Table 3.5: Cryo-loop offsets and adjusted quantities. The offsets in target position are relative to the center of the target ladder. The minus sign denotes beam-right directions. The final quantities are calculated using raster-averaged target length and the nominal target density and take into account the cryo-loop offsets, target ladder and vacuum motion offsets, as well as the nominal beam position offset.

Target	Loop	cell offset(mm)	y_{ave} (cm)	τ (g/cm ²)	ρ (gm/cm ³)
H	2	-0.03±0.02	3.894±0.026	0.2794±0.0023	0.0723
² H	3	-0.10±0.02	3.861±0.026	0.6446±0.0052	0.167
³ He	2	-0.03±0.02	3.894±0.026	0.2736±0.0022	0.0708
⁴ He	1	0.31±0.02	3.890±0.026	0.5229±0.0042	0.135

r , but rather traverses a path displaced by x from the center of the target, then the actual length traversed is

$$y = 2 \sqrt{r^2 - x^2}. \quad (3.2)$$

The relative position of the beam is given relative to the sum of all the offsets. Also, the fact that the beam is rastered over a small area on the target must be accounted for when the target thickness is determined. The final target thickness is calculated by multiplying the target density by the raster-averaged target length:

$$\bar{y} = 2 \frac{\int_{x_0-w}^{x_0+w} \sqrt{r^2 - x^2} dx}{\Delta x}, \quad (3.3)$$

where the limits are defined by the edges of the raster pattern. For E02-019, the size of the raster was ±1.2mm about the center of the beam, x_0 . The nominal and raster-averaged thicknesses are listed in Table 3.5.

Another fact that leads to a correction to the target thickness is that the beam

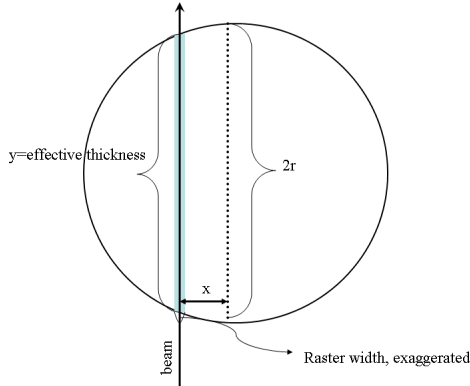


Figure 3.9: Beam path is offset from the center of cryotarget with shaded region indicating the raster pattern. y is the actual thickness when the beam is offset by x from the center of the cryotarget, of thickness $2r$.

position is not constant, but deviates by as much as 0.1 mm from the target center. EPICS data (Sec. 3.7.1) from the BPMs was taken in 30-second intervals for every run. An weighted average for the position of the beam was calculated for each run and converted into a correction to the target thickness using Eq. 3.2. A systematic uncertainty of 1.3% was assigned to this correction based on the maximum deviation from the nominal beam position.

There was an additional factor to account for during the Helium running period. Both Helium loops had small leaks, so that the density did not remain constant over the data-taking period. To account for this, the EPICS (sec. 3.7.1) temperature and pressure readouts were used to calculate the density for each run and the correction applied on a run-by-run basis in the data analysis procedure. The EPICS readouts are done in 2 second increments, which means that a given run has many pressure,

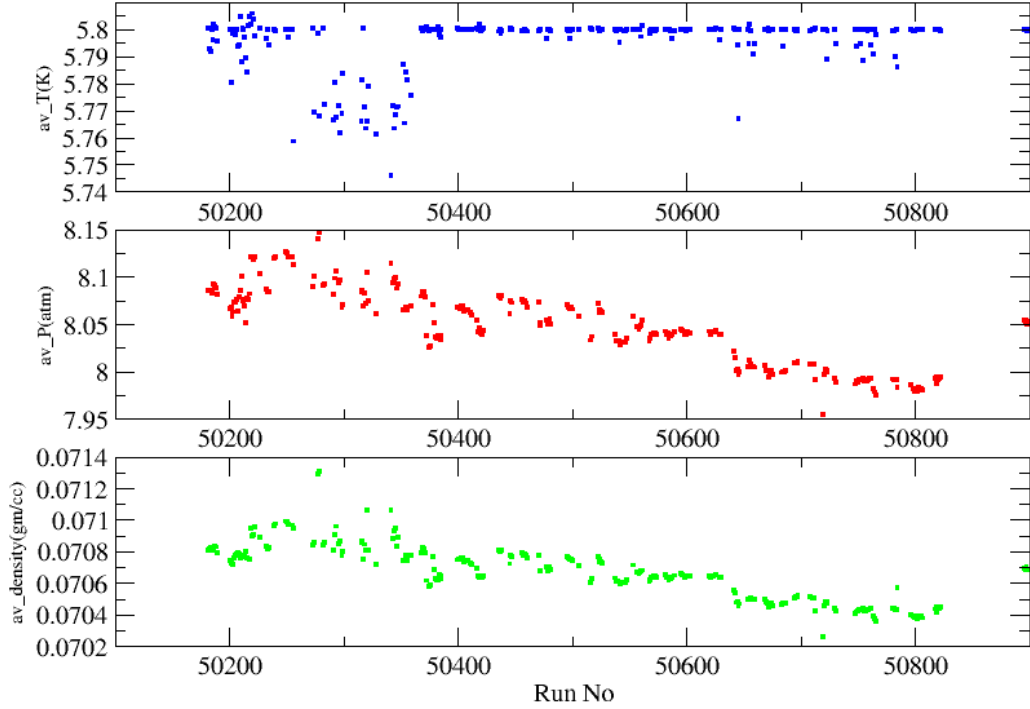


Figure 3.10: The average values for pressure, temperature and calculated density for each ^3He run. The decreasing density indicates a leak in the cryocell.

temperature readouts. A density was calculated for each EPICS event and then averaged for the whole run. For ^3He , tables [72] listing density as a function of temperature for a variety of pressures were used and for ^4He , a NIST report was used [73]. Fig. 3.10 shows the EPICS quantities for the ^3He runs as well as the extracted density as a function of run number. From the decreasing density, it is evident that there was, in fact, a leak. No such leak was detected for the hydrogen/deuterium running period, and therefore a constant density value was used for all the runs.

There are systematic uncertainties associated with the knowledge of the equation of state for each cryogenic target, and the measurements of temperature and pressure. The temperature is known to within 0.1K and the pressure is known to within 1.5Psi. This translates to different uncertainties in the thickness for different targets, which are listed in Table 3.6. Additionally, there's an uncertainty of 1.3% due to the variation in the average beam position on target and a 0.2% uncertainty in the knowledge of the cell diameter. These are the same for all cryogenic targets.

Table 3.6: Target-dependent systematic error sources for the cryogenic targets.

Source	^2H	^3He	^4He
Equation of State	0.5%	1.0%	1.0%
Pressure	0.01%	0.6%	0.2%
Temperature	<0.1%	1.7%	0.9%
Cell Diameter	0.2%	0.2%	0.2%
Beam position on target	1.3%	1.3%	1.3%
Total	1.4%	2.4%	1.9%

3.5 High Momentum Spectrometer

The scattered electrons were deflected and detected using Hall C's High Momentum Spectrometer (Fig. 3.11). The HMS is a QQD system with a bend angle of 25° and a 10.5° minimum closing angle with respect to the beam line [74]. The HMS magnets are supported on a common carriage which rotates around a central bearing, rigidly mounted to the floor. All four magnets are superconducting and are cooled

with 4K Liquid Helium from the End Station Refrigerator (ESR). The quadrupole magnets determine the acceptance and focusing properties of the HMS, while the dipole magnet is used to set its central momentum. In point-to-point tune (optimized for vertex reconstruction), the Q1 and Q3 magnets focus in the dispersive directions and Q2 focuses in the transverse direction. The dipole is also a dispersive magnet. The HMS is referred to as a 'software' spectrometer, meaning that the momentum

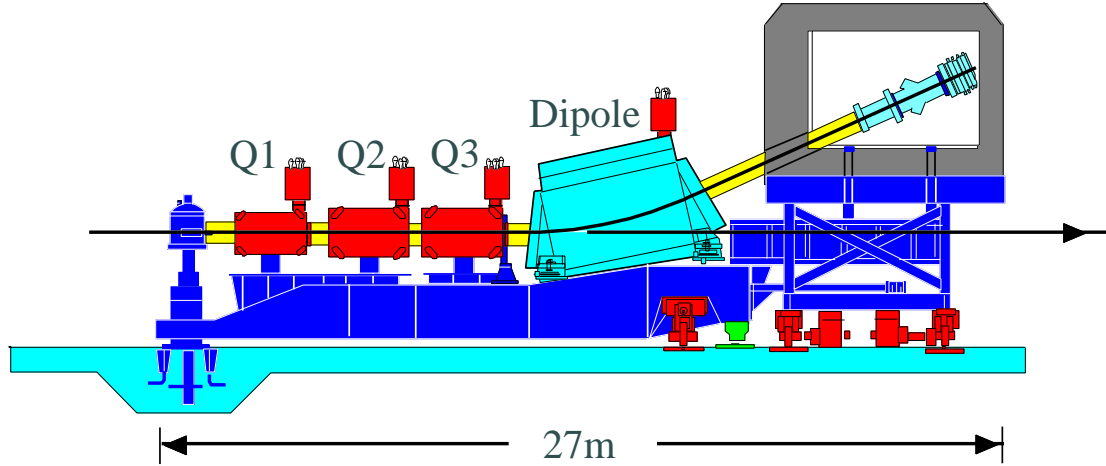


Figure 3.11: HMS: Side view.

of a detected particle is determined by software reconstruction. The HMS can be set to a maximum central momentum of 7.4 GeV/c with a solid angle of $\sim 6.7\text{mSr}$ and a momentum acceptance of $\sim \pm 12\%$ around the central setting. However, to limit the analysis to the area where the acceptance was well known, only events within $\sim \pm 9\%$ central momentum were used in the analysis. The parameters of the quadrupole and

dipole magnets can be found in Tables 3.7 and 3.8, respectively.

Table 3.7: HMS Quadrupole Parameters

	Warm Radius (cm)	Pole Radius (cm)	Length (m)	Pole Field (T)
Q1	22	25	1.89	1.5
Q2	30	35	2.10	1.56
Q3	30	35	2.10	0.86

Table 3.8: HMS Dipole Parameters

Gap	42 cm
Good Field Width	± 30 cm
Length	5.26 m
Pole face Rotations	-6°, -6°

The field in the quadrupole magnets was set by current and the field in the dipole was set using an NMR probe inserted in the magnet. To minimize hysteresis effects, the magnets were always ramped 100A above the highest field first, and then ramped down to each data setting. The fields in the magnets were monitored using Hall probes.

Before entering the first magnet, the scattered particle passes through a collimator, mounted on the front of the Q1 magnet. There was a choice of 3 collimators: pion, large, and sieve. The sieve slit (Fig. 3.12) is used to test the optics of the HMS and consists of an array of small apertures separated by 2.54 cm in the vertical direction and 1.524 cm in the horizontal direction with 2 holes missing in order to verify the

orientation of the slit. The pion collimator (Fig. 3.12) was used to take production data. It is an extended octagon in shape and sets the HMS angular acceptance.

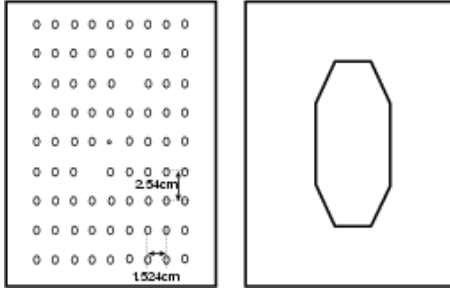


Figure 3.12: HMS Collimators: Sieve and Pion

3.6 Detector Package

The detector package used in the HMS is pictured in Fig. 3.13. The Aerogel Čerenkov detector is not shown as it was taken out for this experiment. The detector stack contains two drift chambers, two sets of x-y hodoscopes, a gas Čerenkov and a lead glass calorimeter. The drift chambers are used for tracking particles, while the hodoscopes are used to form the primary trigger. The calorimeter and the Čerenkov are used to form several legs of the electron trigger and are also used for particle identification (and pion rejection) in the offline analysis.

3.6.1 Drift Chambers

The drift chambers provide tracking information. When a charged particle passes through a gas-filled chamber and ionizes the gas, the ejected electrons “drift” to the

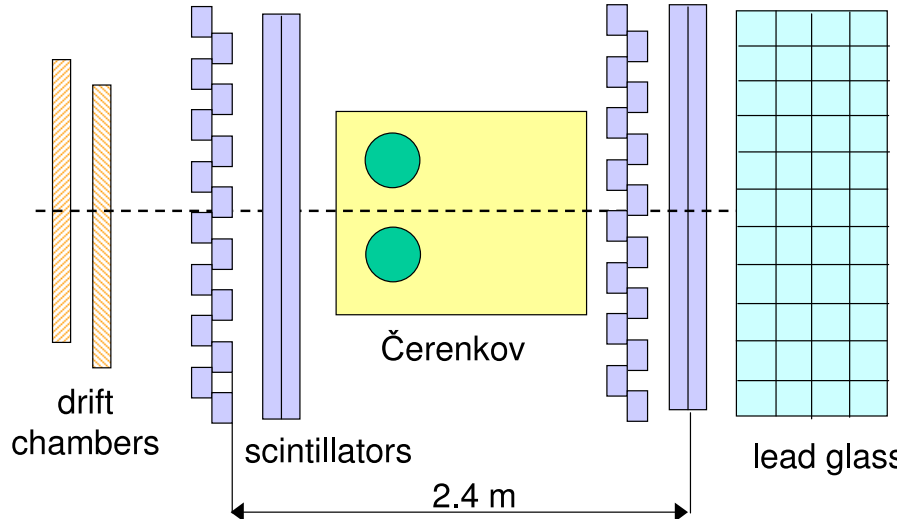


Figure 3.13: Detector Stack in the HMS

wires in the chamber. By measuring the drift time, we can calculate the drift distance and the position of the track.

There are 2 drift chambers in the HMS, one located in the front and the other in the back of the focal plane. There are 6 planes in the drift chambers: X, Y, U, V, Y', X' with spacings of 1.4 cm between them. The X and Y planes are orthogonal and the U, V planes are inclined 15° with respect to the X and X' planes. The X' and Y' planes are offset from the X and Y planes by 5cm. The sense wires (anodes), which reside at ground potential, detect the ionized electrons and the field wires (cathodes) produce the electric field that guides the ionized electrons to the sense wires. A schematic of the drift chambers can be seen in Fig. 3.14.

The signals from each anode wire are amplified and read out in Nanometrics and LeCroy 2735DC discriminator cards. The discriminated signals are carried to the

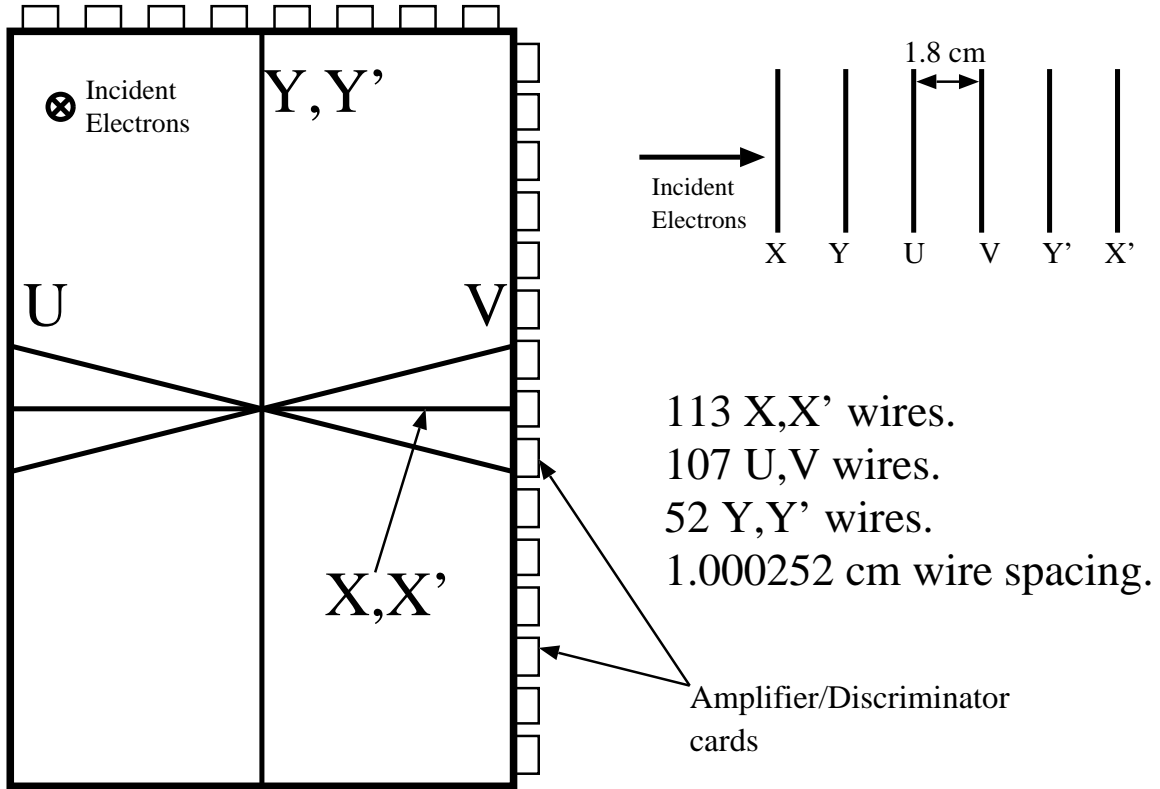


Figure 3.14: HMS Drift Chamber, a front view

LeCroy 1879 Time-to-Digital Converters (TDCs) where a stop signal is formed. The TDCs were programmed to read out events within a $\sim 4\mu\text{s}$ window, since the trigger signal from a particle in the spectrometer arrives at the TDC in $\sim 2\mu\text{s}$.

The drift chambers are filled with a mixture of argon/ethane gas. When a charged particle passes through the chamber, it ionizes the gas. The ejected electrons are accelerated by the electric field and drift from the track to the closest sense wire. The electrons are detected at the sense wires and the signal is read out as a current over some period of time. The sense wires are positioned 1 cm apart from each other, meaning the particle's position can be measured with a 0.5 cm precision, half

the spacing by this method alone. However, precision of 0.5 cm is not nearly good enough for tracking and instead the time that it took for the ionized electrons to reach the sense wires is used. This time is calculated by using the hodoscope TDCs to determine the time that the particle passed through the focal plane and the time that the sense wire detected the ejected electron. This time is then converted to a drift distance which is added to the position of the wire, giving the position of the track. Making use of the different orientations of the sense wires in the 6 planes, the trajectory of the particle can then be reconstructed.

3.6.2 Drift Chamber Calibration

Each hit in the drift chambers has a TDC value associated with it which is read out. These values can be converted to a drift time using timing information from the hodoscopes. The final product, a time-to-distance map, a driftmap, gives the calculated distance from the wire where the event occurred. To calculate a driftmap, we assume a direct relationship between the drift distance and drift time, $x = f(T)$, and that the number of events in a given interval of distance must be equal to that in some corresponding interval in time. We use the drift time distribution in each plane using a large number events and the TDC values for all the wires. Integrating over the time spectrum, we get the drift distance:

$$d = d_{max} \frac{\int_{t_{min}}^T F(t)dt}{\int_{t_{min}}^{t_{max}} F(t)dt}, \quad (3.4)$$

where t_{min} and t_{max} define the times to be used in the fit, d_{max} is them maximum distance from the wire, T is the time recorded by the TDC, $F(t)$ is the drift time distribution. When properly calibrated, the drift distance histogram should be flat. A driftmap is generated for each of the planes in the drift chambers. A sample drift time histogram and the distance histogram calculated from it can be see in Fig. 3.15. A single driftmap was used for all the runs in the analysis.

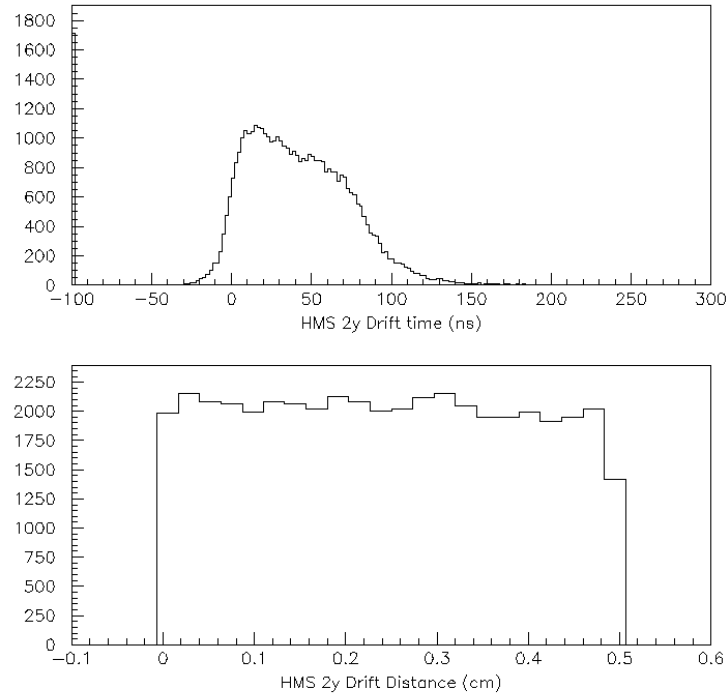


Figure 3.15: Drift time and drift distance spectra for one plane of one of the HMS drift chambers. A negative drift time is recorded because there's an overall offset between times measured in the drift chambers and by the hodoscope.

3.6.3 Hodoscopes

The HMS has two pairs of “x-y” scintillator planes - one placed before and one after the drift chambers. Each x-plane had 10 paddles oriented in the dispersive direction and each y-plane had 16 paddles oriented in the non-dispersive direction. The paddles are 1 cm thick and 8 cm wide and are positioned so that there’s 0.5cm overlap between adjacent paddles preventing any particles from passing between the paddles. The paddles are made of strips of BC404 scintillator with UVT lucite light guides and Philips XP2282B photo-multiplier tubes on each end.

Charged particles ionize atoms in the scintillator paddles when they pass through them. The “liberated” electrons excite molecular energy levels, which, upon their decay, emit light along the length of the paddle. The light that hits the surface of the scintillator at $\theta > \theta_c$ is completely reflected ($\theta_c = \sin^{-1}(1.0/1.58) = 39.3^\circ$). The reflected light is detected with the PMTs mounted on the ends of the scintillator paddles. The signal is then converted into an electrical pulse, split, and sent to ADCs and TDCs, as well as scalers and trigger logic modules in the electronics room of the counting house. The signals from all the tubes on a one side of a given plane (for example: S1X=S1X+ and S1X-) are ORed together. Then, the outputs of the ORs for each plane were ANDed together and then ORed with the remaining hodoscope plane in the pair (for example: S1=S1X and S1Y, S2=S2X and S2Y), giving the primary hodoscope signals used in the trigger.

Timing information from the hodoscope had to be corrected for timing and pulse

height offsets in each element. Different particles deposit different amounts of energy, but since the electronics use constant threshold discriminators, which turn on once the received pulse reaches a set point on the discriminator, the timing information for particles that deposit more energy would be biased to earlier time values.

The timing correction was a consequence of the fact that light that arrives at the PMT could have undergone multiple internal reflections. This effect was corrected by using the distance, d_{prop} , to determine the time of propagation from the point where particle passed through the scintillator paddle to the PMT. The effective velocity of light in the paddle is a function of both the index of refraction and the dimensions of the paddle. The propagation time for event e at PMT i , $t_{prop}^{i,e} = d_{prop}^e / v_{scin}^i$, was then subtracted from the hit time recorded at the PMT. The timing correction was on the order of a few ns.

The need for a pulse height correction arises from the correlation between the ADC value of a PMT signal, $A_{pmt}^{i,e}$, and its arrival time at the TDC. The pulse shape of the analog signal from a PMT is a weak function of amplitude, so the greater the amplitude of the ADC signal, $A_{pmt}^{i,e}$, the sooner it crosses the threshold voltage of the discriminator. This is corrected for by assuming a mathematical form for the leading edge of the analog PMT signal. The form used was a Lorentzian, which fit parameters determined for each PMT. The pulse height correction was on the order of a few ns and was subtracted from the hit time at each PMT. A more detailed explanation of both corrections can be found in Ref. [68].

Prior to the beginning of the experiment, the hodoscope PMTs were gain-matched using a ^{60}Co gamma ray source placed in the center of each paddle. The voltages on all the tubes were set so that the Compton edge of the gamma rays gave a pulse height of 175 mV at the discriminator inputs in the electronics room.

3.6.4 Gas Čerenkov

The gas Čerenkov detector is named after the man who first observed and characterized Čerenkov radiation. Čerenkov radiation is emitted when the speed of a particle is greater than the phase velocity of the electromagnetic fields at a given frequency ω , i.e. $v > \frac{c}{\epsilon(\omega)}$. In other words, the speed of the particle in a medium must exceed the speed of light in the same medium, $v > \frac{c}{n}$. The angle θ_c of emission of Čerenkov radiation relative to the velocity of the particle is given by

$$\cos \theta_c = \frac{1}{\beta n} \quad (3.5)$$

Mirrors inside the detector focus the Čerenkov light onto photo-multiplier tubes, which output a current that is subsequently converted into an electronic signal. The pressure inside the Čerenkov was chosen so that electrons with a given energy would emit Čerenkov radiation, but heavier particles, such as pions, would not. Some pions will still produce a Čerenkov signal if the pion produces a knock-on electron of sufficient energy to emit Čerenkov light. To minimize the rate of the knock-on electrons, the entrance window to the detector is made as thin as possible.

The HMS Čerenkov is a cylindrical tank with an inner diameter of 150cm and a length of 165cm. The Čerenkov detector was filled with a C_4F_{10} gas ($n=1.00143$ at STP), pressurized to 0.35Atm (5.15Psi) giving a refractive index of 1.0005. The resulting pion threshold was $\approx 4.4\text{GeV}/c$ and the electron threshold was $\approx 16\text{ MeV}$. There are 2 spherical mirrors at the back of the tank which reflect and focus the Čerenkov light into 2 5" Burle 8854 photo-multiplier tubes. The signals were relayed into a LeCroy 1881M ADC as well as a discriminator that was subsequently an input to the trigger. The minimum signal results when one photoelectron is ejected from the photocathode. The calibration involved locating the single photoelectron in the ADC spectrum of each tube and fitting a Gaussian to it (see Fig.3.16), the location of the peak was used as the calibration constant to calculate the number of photoelectrons produced by particles in production running (summed over the tubes). The average yield was 6-8 photoelectrons. A typical spectrum of photoelectrons can be seen in Fig. 3.17.

3.6.5 Lead Glass Calorimeter

The HMS calorimeter was used for particle identification in conjunction with the Čerenkov. The calorimeter is the last detector in the HMS hut and consists of four layers of 13 10cm x 10cm x 70cm TF1 lead glass blocks with Philips XP3462G Photomultiplier tubes attached to them. The 2 front layers have the PMTs on both ends of each block, whereas the last 2 layers have PMTs on only one side.

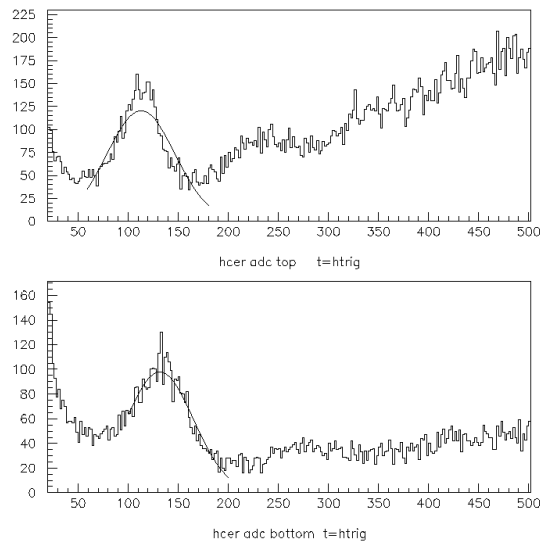


Figure 3.16: ADC spectra for the HMS Čerenkov PMTs, bottom and top. The single photoelectron peak was fit with a Gaussian for calibration. Run 50103 was used.

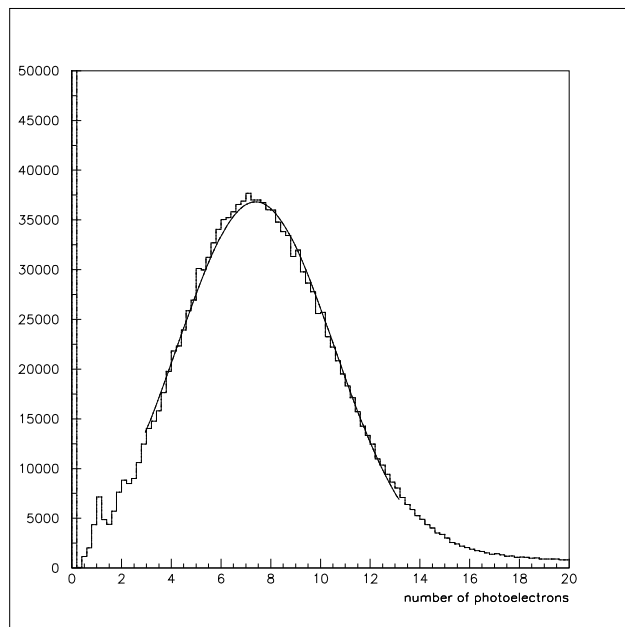


Figure 3.17: A typical spectrum for the HMS Čerenkov. Run 50553 was used, which was taken at $p_{HMS}=3.74$ GeV/c, below the pion threshold.

The calorimeter measures the energy deposited by a charged particle when it passes through it. An accelerating high energy electron emits photons through Bremsstrahlung. These photons form electron-positron pairs which radiate more photons and the process is repeated. Therefore, the number of particles increases exponentially with depth in the calorimeter. This is referred to as a “cascade shower” of particles earning the calorimeter a nickname “shower counter”.

Electrons and positrons deposit all of their energy in the detector, while pions and protons deposit a relatively constant amount of energy, due to ionization and direct Čerenkov light ($\sim 300\text{MeV}$ for pions). So, as long as the energies of the particles are well above this constant, the calorimeter can be used to separate electrons from other particles by measuring the deposited energy. However, pions can undergo nuclear interactions in the lead glass, which can lead to a shower similar to those created by electrons. The pion signal then has a long tail that extends under the electron peak. For this reason, the calorimeter is not used alone for particle identification, but rather in combination with the Čerenkov.

The signal from each PMT is split and the outputs are sent into a LeCroy 1881M ADC and a Philips 740 linear fan-in module where they’re summed. The sum in the first layer (PRSUM) and the sum of all the layers (SHSUM) are discriminated to give three logic signals for the trigger. PRLO and PRHI are low and high threshold on the energy deposited in the first layer, and SHLO is a threshold on the total energy deposited in the calorimeter and is above the pion peak.

Two corrections are applied to the raw ADC values. First, the signal is corrected for attenuation through the block so that it is independent of the distance from the PMT. Once the attenuation correction is made, a gain correction factor is applied to each channel. This gain correction factor is determined through a calorimeter calibration procedure, such that the sum of the corrected ADCs gives the electron energy.

The calorimeter calibration was performed more than once, using different methods before settling on one approach. The goals were to minimize the width of and the position dependence of the electron peak. Each calorimeter block has a gain associated with it, which is used to calculate the deposited energy during the event reconstruction process. When calibrated properly, the electron peak will be placed at electron energy, reflecting the energy deposited in the calorimeter.

After performing an initial calibration, the position of the peak was examined as a function of time to check the stability of the calibration. What was discovered instead was that some electron peaks had anomalous widths (asymmetric, wider than expected). The problem became obvious when the position of the peak was examined as a function of time for a given run. Fig. 3.18 shows fairly sudden changes in the calorimeter spectrum ($HSSHTRK = (\text{energy deposited for a track})/p_{HMS}$) as a function of event number. The right plot shows the two electron peaks that correspond to shifted and unshifted spectra. Since the pion peak (located at ≈ 0.4 in the $HSSHTRK$ spectrum) does not appear to be shifted by as much as the electron peak, the shift

cannot be a result of an offset in the pedestals.

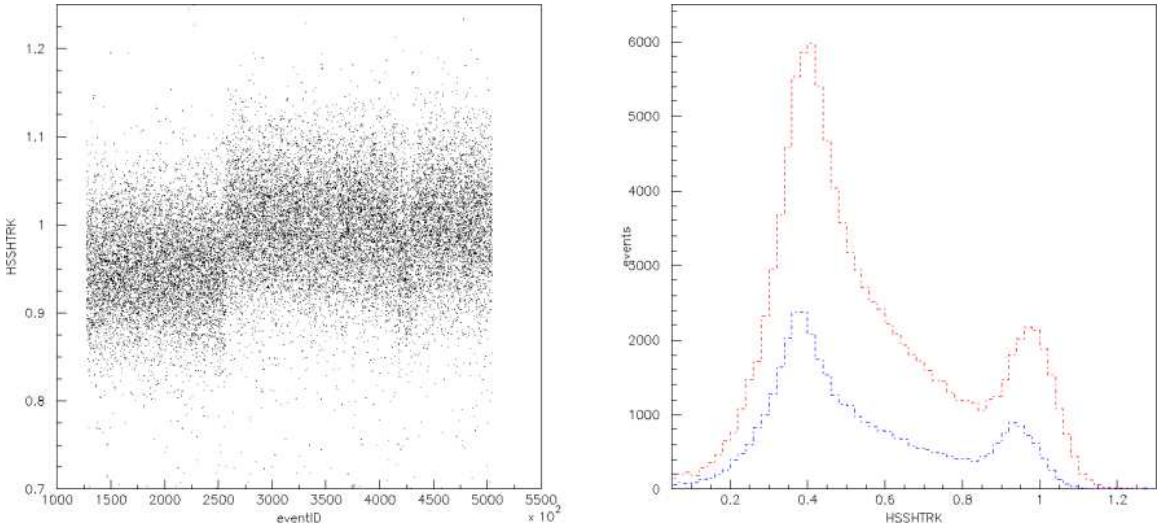


Figure 3.18: The left plot shows the electron spectrum in the calorimeter for run 51572 as a function of event number with sudden shifts. The plot on the right shows the complete spectrum for event numbers corresponding to the nominal peak (red) and the shifted peak (blue).

This shift was determined to be the result of an intermittent degradation of the leading edge of the discriminator signal used to gate the ADC. No correction was made in the end as the small loss in resolution was insufficient to limit π rejection. For a detailed discussion, refer to [75].

The final calibration was performed using a stand-alone compiled program [76]. This code uses some initial set of gains and performs a random walk, changing the gain on each block individually and checking to make sure that the χ^2 of the energy spectrum improves. A sample HMS shower spectrum is shown in Fig. 3.19.

One run was chosen to perform a calibration that would be used for all the data. This run was at our smallest angle (18°) and a fairly high momentum (3.74 GeV/c)

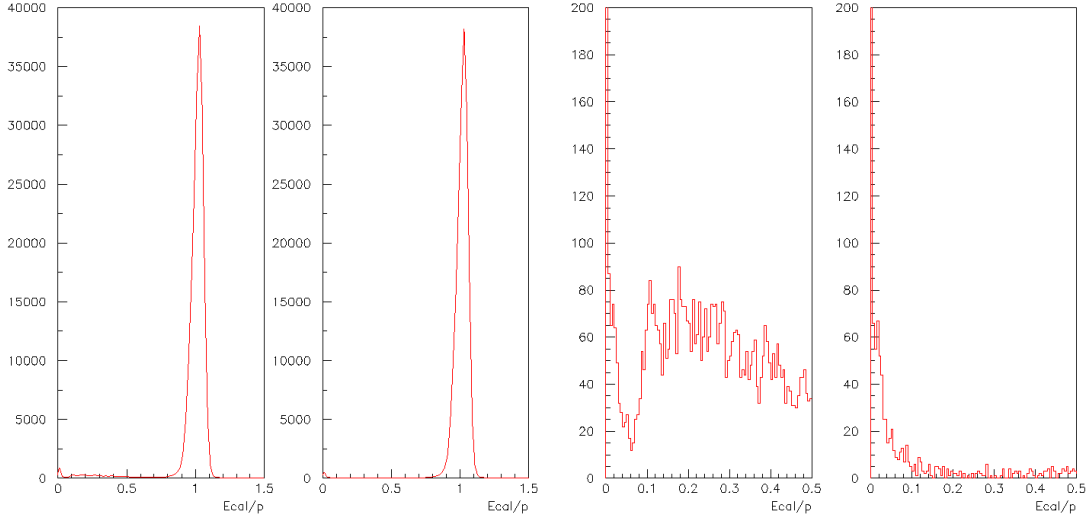


Figure 3.19: HMS shower counter spectrum (Energy deposited in the calorimeter divided by the particle's momentum). The figures are for a deuterium run (51390) at 18° and $p=3.74$ GeV/c. The two figures on the left show the electron peak before and after a Čerenkov cut of 1.5 photoelectrons applied. The two figures on the right show the region 0-0.5 in more detail.

so that the pion background was minimal, but the momentum was still low enough so that the focal plane was well-populated.

3.7 Trigger

There were several triggers in use during the running of E02-019 and they were used for different purposes. Choosing the correct trigger is important since it's the first line of particle identification and time and disk space can be saved if background events can be rejected at the trigger level. The time is of interest because it can contribute to inefficiency by increasing the deadtime - periods when the data acquisition system

is unavailable and cannot accept new events because it's processing/recording the previous event. For E02-019, the deadtime was kept below 20% by the occasional use of prescale factors. Most of the time, the rates were low enough that a prescale factor of 1 was used.

The trigger that was used for the main data taking (e^- detection) was ELREAL, which can be traced in Fig. 3.20. ELREAL is an electron trigger and requires scintillator hits and user-defined particle identification signals.

The first part of the trigger was formed using the signals from the hodoscope. As described in Sec. 3.6.3, a hit in a given plane of the hodoscope is defined as a coincidence between 2 signals from the opposite sides of a plane, not necessarily from the same paddle. Two scintillator triggers are then formed, STOF and SCIN (a.k.a '3/4'). STOF requires a hit in one of the S1 (front) planes and another in one of the S2 (rear) planes, the minimum number of planes for time of flight calculation. SCIN requires hits in 3 of the 4 planes. By that definition, if SCIN is satisfied then STOF is also satisfied.

The other legs of the ELREAL trigger provide preliminary particle identification. The analog signals from the first layer of the calorimeter are sent to discriminators and if they exceed a low and/or a high threshold, PRLO and/or PRHI logic signals are sent to the trigger. SHLO is another logic signal that is sent to the trigger from the calorimeter, but the input to the discriminator in this case is the energy sum in all the layers of the calorimeter. Finally, the CER signal requires the Čerenkov sum

to fire the discriminator (threshold set to ~ 0.5 photoelectrons) .

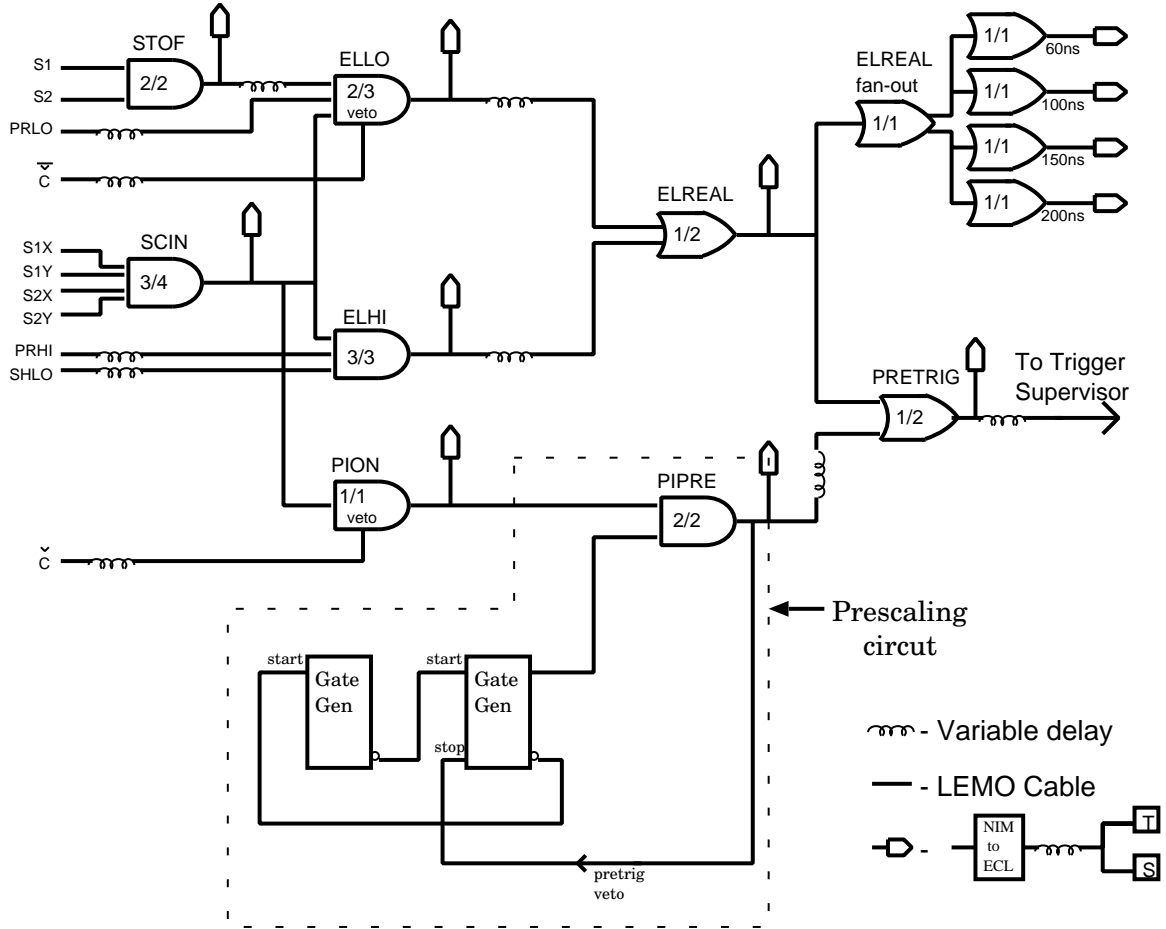


Figure 3.20: HMS single arm electronics

ELLO requires the CER, and 2 of the following: STOF (loose hodoscope cut), SCIN (tight hodoscope cut), or PRLO (loose shower counter cut). The other leg of the trigger, ELHI, requires SCIN, PRHI, and SHLO to be satisfied. So, if an event satisfies either the ELLO or ELHI leg of the trigger, it is a good candidate for an electron. ELCLEAN, the primary electron trigger, is defined as the OR of ELLO and ELHI, and a more strict electron trigger, ELCLEAN, is defined as their AND signal.

Note that the trigger is robust against inefficiency in any given leg. For example, a trigger signal is formed in the absence of a Čerenkov signal or a calorimeter signal, as long as the other detectors are performing well.

In addition to the ELREAL events, a sample of pions was also taken in order to study the pion background and also to have a sample of events that was not sensitive to inefficiencies associated with particle identification requirements. This trigger, PION (Fig. 3.20), was defined as a good hodoscope signal (SCIN) and a Čerenkov veto (note that PION events can still satisfy the ELREAL trigger via the ELLO route). These events were then prescaled by a dynamic prescaling circuit so that the number of events recorded was a small fraction of the number of ELREAL triggers.

Each trigger and most of the pre-trigger signals were output to a TDC and read out by the DAQ system. This made it possible to cut on the various branches of the trigger during the data analysis and efficiency calculations.

3.7.1 Data Acquisition System

The data acquisition for E02-019 was handled by the CEBAF Online Data Acquisition System (CODA) [77]. A schematic of the CODA software chart can be seen in Fig. 3.21. Information from ADCs and TDCs is read out from the Read-Out Controllers (ROCs) which are CPUs in the FASTBUS and VME crates. The ROCs communicate with the Trigger Supervisor, which generates the triggers that start the ROC read outs. Then, the ROCs send the data event fragments to the event Event Builder,

where all the header information and data is compiled into an event. Once the event is built, it is placed into a buffer, then tested (and possibly rejected) and finally written to disk. CODA also contains a graphical user interface (RunControl) that allows the shift worker to start and stop runs and change run parameters.

Three types of information are read out and written to disk during each run: event information from the ADCs and TDCs (read out for event, including raster/BPM information), scaler information (read out every 2 seconds), and slow control variables from the Experimental and Physics Industrial Control System (EPICS) database (read out every 30 seconds). EPICS quantities are not directly associated with data acquisition and include information on spectrometer magnet settings, target status variables, beamline controls, etc.

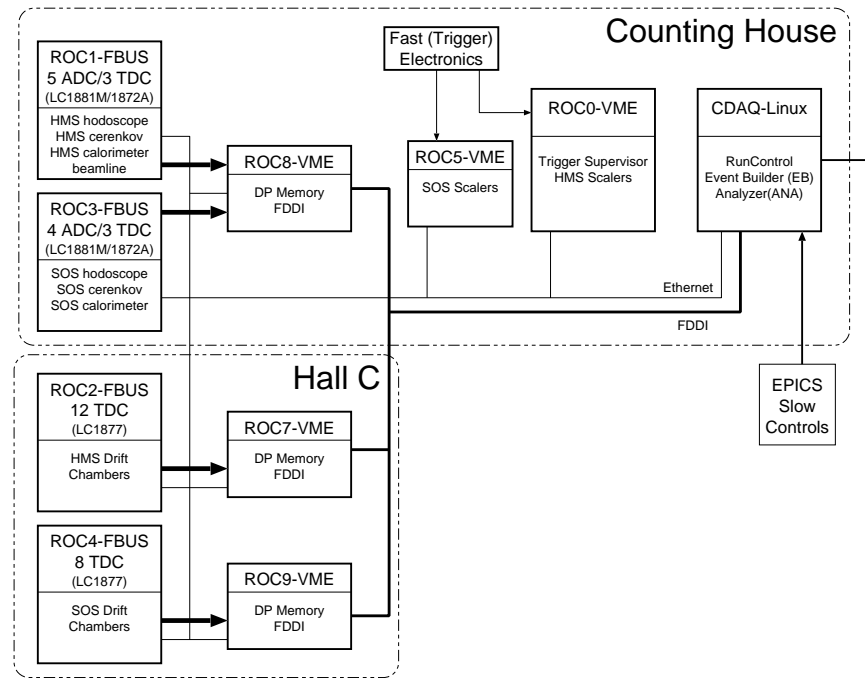


Figure 3.21: Schematic of Hall C data acquisition system, showing the elements described in Sec. 3.7.1

Chapter 4

Data Analysis

The first stage of analysis of the raw data was done using the Hall C reconstruction software, the “Replay Engine.” The code reads in the raw detector signals, generates tracks as well as particle identification information for each event. In addition, the engine also keeps track of software and hardware scaler quantities that are written to report files at the end of the replay. The data is output in two formats: PAW HBOOK files and PAW ntuples. The HBOOK files contain a large set of histograms that are used to check detector performance as well as to perform some calibrations. The ntuples are organized event-by-event, with a set of quantities calculated for each event. The ntuples are then used as the input to the second stage of the analysis, where physics quantities like cross sections are extracted.

In this chapter, the methodology for extracting cross sections will be discussed, including how tracks are reconstructed, how good events are selected and the correc-

tions that are applied.

4.1 Spectrometer Optics/Coordinates

Before discussing the detector quantities, it is important to define the coordinate system used in measuring these quantities as well as the different reference frames used. The spectrometer coordinates (see Fig. 4.1) are defined with \hat{z} along the optical axis (see below) inside the spectrometer, \hat{x} points down in the dispersive direction, and \hat{y} points out in the non-dispersive direction (beam-left).

The central ray is defined as the trajectory of a particle that enters the spectrometer through the center of the entrance aperture or the optical axis of the first magnet. The plane approximately half-way between the two drift chambers is the detection or focal plane. The central rays are those that pass through the center of the detection plane and follow the optical axis. The momentum of the particles whose trajectories lie along the optical axis defines the central momentum of the spectrometer. The detection/focal plane is perpendicular to this central trajectory and tilted 85° with respect to the 'true' focal plane of the spectrometer. The 'true' focal plane is an approximation to the surface defined by the initial rays at various angles, used to determine the position at which they're focused by the magnets.

Within the spectrometer coordinate system, two frames are used: the focal plane frame and the target frame. The focal plane coordinate system has its origin in the center of the detection plane (but the two planes do not coincide), and its variables

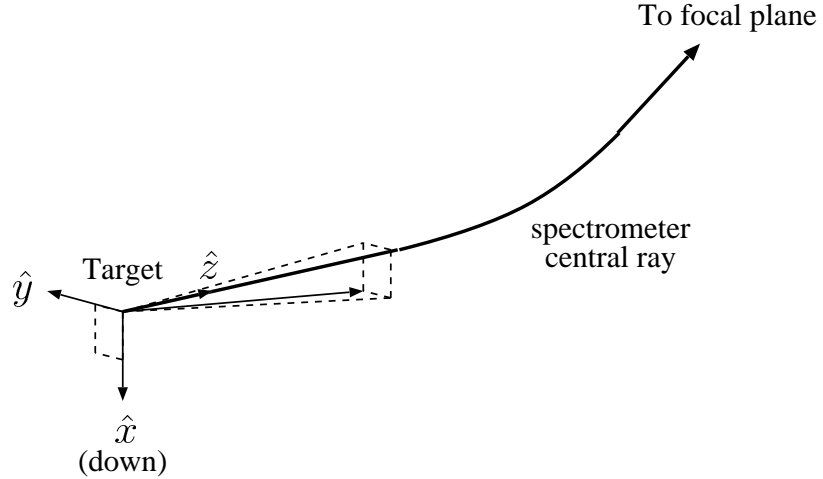


Figure 4.1: Target coordinate system: \hat{z} points along the optical axis inside the spectrometer, \hat{x} points down in the dispersive direction, and \hat{y} points beam-left.

are given the subscript with “fp”. The target coordinate system is centered at the target and the variables associated with it are have “tar” subscripts (see Fig. 4.1).

The typical distribution of electron events in the focal plane is shown in Fig. 4.2. This shape, commonly referred to as an ‘hourglass’, is the result of focusing in the dispersive direction by the Q1 and Q3 quadrupole magnets and in the transverse direction by the Q2 quadrupole.

4.2 Event Reconstruction

The trajectory of the particle is reconstructed using information from the two drift chambers. The hits in the first drift chamber are used to identify clusters of hits, called “space points”. The hits in each of these clusters are then fit to a mini-track, called a “stub”. Within each stub, it is necessary to determine whether the particle

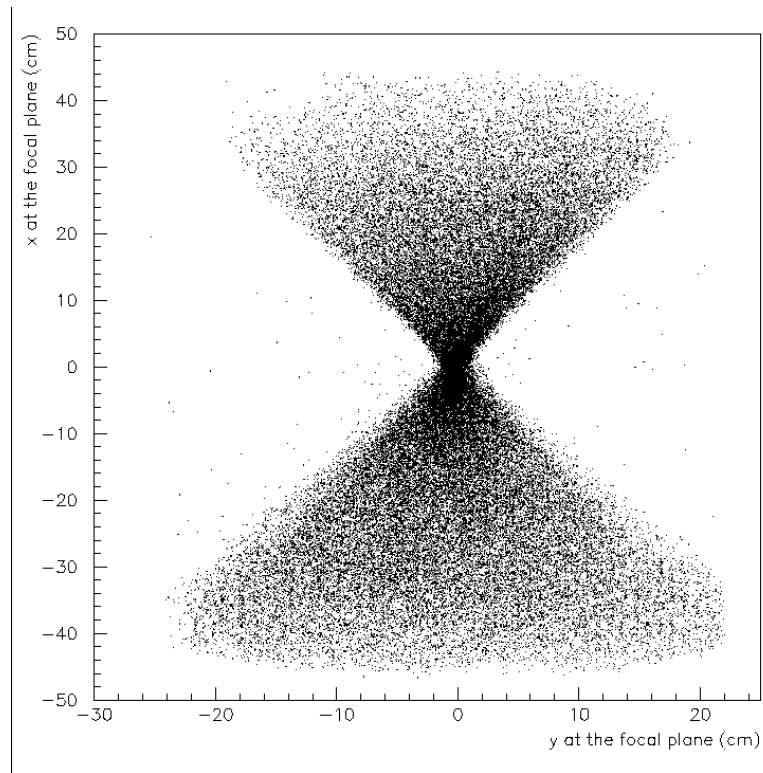


Figure 4.2: Typical “hourglass” distribution of electrons in the HMS. Data from a carbon run at $\theta_{HMS} = 50^\circ$, $p_{HMS} = -1.00$ GeV/c is shown.

passed the wire on the left or the right. The brute force approach is to fit all the left-right combinations and to choose the best one based on χ^2 , but as this method is time consuming, it is the last resort. Instead, for planes with parallel wires (y and y' , for example), a small angle approximation is used. If the same position is reconstructed for the two planes, since the planes are offset by 1/2 cell, the particle is assumed to have passed between the two wires.

After all the fits have been performed for the first drift chamber, this procedure is repeated for the second one. The tracking code then fits one track through them. If more than one track is found, the one with the smaller χ^2 is chosen. The track is then projected to the focal plane, defined as being approximately half-way between the two chambers, and the focal plane variables $(x_{fp}, y_{fp}, x'_{fp}, y'_{fp})$ are determined.

Once the position and angles of the particle are known in the focal plane, we can reconstruct the same quantities at the target. This is done using a transformation matrix of the form:

$$a_0^i = \sum_{j,k,l,m} M_{jklm}^i (x_{fp})^j (x'_{fp})^k (y_{fp})^l (y'_{fp})^m \quad \text{for } (1 \leq j+k+l+m \leq N) \quad (4.1)$$

where a_0^i is a target quantity, M_{jklm}^i is one column of the reconstruction matrix, and N is the order of the transformation, which for the HMS is 5. The quantities given by this transformation are $x'_{tar} = a_0^1$, which is the slope of the track ($\frac{dx}{dz}$) in the x (dispersive) direction, $y'_{tar} = a_0^3$, which is the slope of the track ($\frac{dy}{dz}$) in the y direction, $y_{tar} = a_0^2$, which is the position of the interaction point, and $\delta = a_0^4$,

which is the deviation from the central momentum in %. x_{tar} is not given by this transformation (only 4 quantities can be extracted since only 4 are measured) and is taken to be 0. While the primed quantities correspond to slopes, the acceptance of the HMS is small enough ($<100\text{mr}$), that it's a reasonable approximation to treat those slopes as angles.

The reconstruction matrix elements were obtained previously using an iterative fitting procedure, starting with a model of the spectrometer optics, from COSY INFINITY [78]. The matrix elements are then refit with HMS data taken with the sieve slit, whose pattern makes it possible to determine which hole the particle went through. The matrix elements are then modified so that each event in the sieve slit data is reconstructed to the correct position. Different targets are used for optimization of different variables, and many fits are performed before the matrix elements are finalized. The details of the fitting procedure can be obtained from J. Volmer's thesis [79].

4.3 Particle Identification and Electron Selection

For the majority of the experiment, the HMS was run with the magnets in negative polarity, accepting all negatively charged particles. Since we're interested only in electrons, it is important to be able to select them and reject the pions. The gas Čerenkov and the lead glass Calorimeter were used to select electrons both at the trigger level and with software cuts in the analysis.

For the analysis, a Čerenkov cut of 1.5 photoelectrons and a calorimeter cut of 0.7 times the value of the electron peak ($E_{cal}/p \approx 1$) were used to select electrons. If the electron peak were perfectly centered at 1.0 in the normalized calorimeter energy spectrum (E_{cal}/p), then we could use a constant value cut, but since calibration is not perfect, the reconstructed peak can be shifted a fraction of a percent away from 1.0. The electron peak was fit to a Gaussian, and the calorimeter cut was defined as the peak position fit value times 0.7. Those events that deposited less energy were rejected. In reality, there is only a small fraction of a per cent difference in the yield if a constant value cut for E_{cal}/p is used.

There are several types of background that are present in the data sample. Some are unwanted electrons that are a result of pair production from a photon emitted either through Bremsstrahlung or as a result of π^0 decay. These are charge symmetric and are eliminated through subtraction of a e^+ yield from the positive polarity running. Another background source is electrons scattered from the container cell walls in the case of the cryogenic targets and these are eliminated by subtracting the empty aluminum can data yield. Finally, some pions pass all the software cuts designed to reject them and get into the electron sample by producing knock-on electrons of energy sufficient to produce a signal in the Čerenkov detector. Knock-on electrons are emitted from atoms when a charged particle passes through matter and transfers energy to the constituent atoms. Even though these pions deposit only $\sim 300\text{MeV}$ of energy in the calorimeter, forming a secondary peak in the spectrum at $\sim 0.3/p$, the

tail of this peak extends beyond the cut and into the electron sample.

4.3.1 Charge Symmetric Background

Some scattered electrons emit high energy photons in the target, which in turn form electron-positron pairs. These pairs can also be produced by the $\pi^0 \rightarrow 2\gamma \rightarrow e^+e^-$ decay process of the neutral pions produced in the target. Some of the electrons from these pairs fire the detectors and can form a trigger. Since these events come from a different process than the one we're interested in, it's important to remove their contribution from the data sample. The background yield is charge symmetric because the positrons and electrons are produced at equal rates. This means that an accurate measurement of the positron yield can be used to determine the background electron yield from pair production. The positron background was measured directly by running the HMS in positive polarity (reversing the polarity of the magnets to bend positively charged particles into the detector hut instead of the negatively charged ones) for all targets. Measurements were taken only at those angle and momentum settings where the background was known to be significant.

At small angles and high momentum settings, positron data were not taken since the background yield was negligible. Fig. 4.3 shows the relative positron yield when compared to the electron yield (including the CSBG) at the same setting. The relative yield is quite small for high x and as a result, no positron data was taken for 18° or 22° for any targets, and no positron data was taken for the highest momenta settings

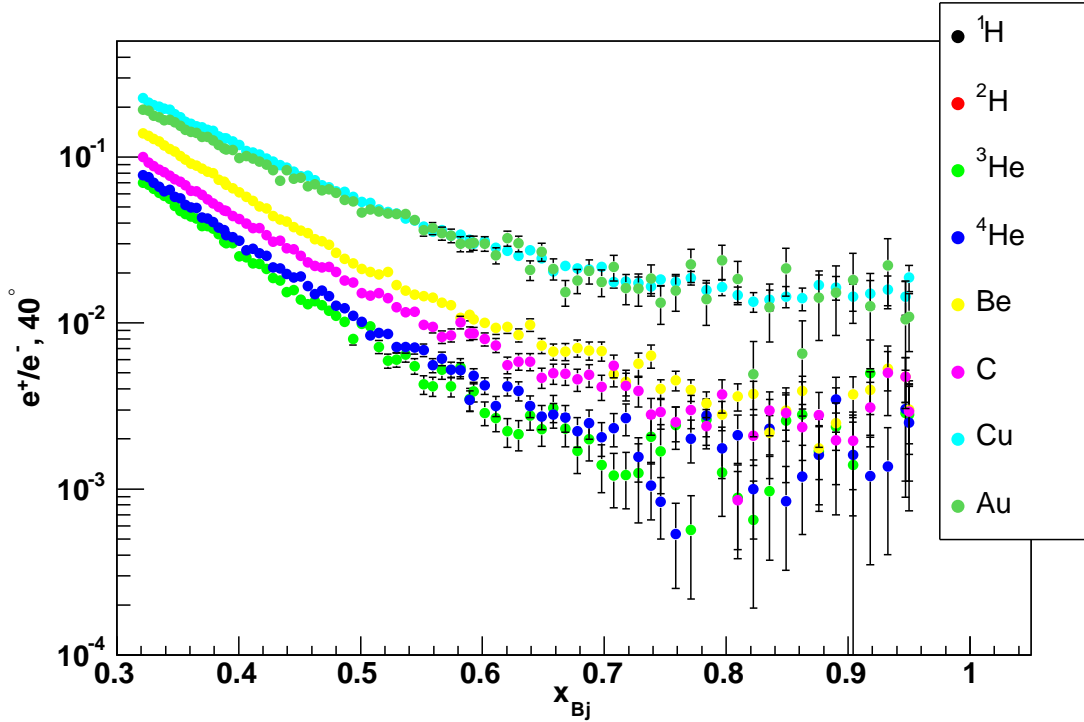


Figure 4.3: The ratio of e^+/e^- yields (a.k.a. CSBG) for all targets at 40° as a function of x

at 26° , except for the Copper target.

The same set of cuts are applied to the positron sample as the electron sample, but since the rates are higher for positive polarity running due to the presence of hadrons, a different trigger is used to keep the dead time low. ELREAL, described in Sec. 3.7 is an OR of two signals, ELLO and ELHI. For the charge symmetric background measurement, the ELCLEAN trigger was used instead, which is the AND of ELLO and ELHI, requiring both a calorimeter and a Čerenkov signal. For the computation of the charge symmetric electron background, we also required the ELCLEAN signal for the electron data sample (both signals were available). The ratio is then computed

using

$$R_{\frac{e^+}{e^-}} = \frac{e_{elcl}^+}{e_{elcl}^-} = \frac{e_{bg}^+}{e_{data}^- + e_{bg}^-} \quad (4.2)$$

where $e_{bg}^{+/-}$ are the background yields from pair production and e_{data}^- is the electron data yield from the reaction we're interested in. Then, using the fact that the yield is charge symmetric, we subtract the background and the net electron yield is then

$$Y^- = Y_{elrl}^- \cdot \left(1 - \frac{e_{elcl}^+}{e_{elcl}^-}\right). \quad (4.3)$$

Since the size of the charge symmetric background varies strongly with kinematics, the systematic uncertainty associated with it is angle-dependent. The size was determined by comparing the F_2^A structure function for copper at the two highest angles (40° and 50°), where the correction is large. As the structure function is expected to scale and the size of the radiative correction is known, we can ascribe any differences to the charge symmetric background subtraction. The uncertainty was determined to be 5% of the size of the correction. For example, the charge symmetric background for the lowest momentum setting at 40° is about 25%, which implies a 1.25% systematic uncertainty. Since the contribution for each angle falls with momentum, the e^+/e^- ratio was parametrized and the systematic uncertainty was calculated for each final data point.

Table 4.1 shows the maximum uncertainty associated with each angle setting of the HMS. As the contribution from the charge symmetric background falls quickly

Table 4.1: Size of the systematic uncertainty due to the subtraction of the charge symmetric background for each of the HMS angle settings used.

θ_{HMS}	Uncertainty due to CSBG(%)
18°	0
22°	0
26°	0.1
32°	0.3
40°	1.25
50°	2

with decreasing angle (see Fig. 4.4), the lowest angles are assumed to have a negligible contribution.

4.3.2 Pion Contamination

Another source of background events are the pions that make it past all the software cuts. This happens when the pions produce knock-on electrons while passing through the entrance window of the gas Čerenkov. As mentioned earlier, these pions typically deposit about 300MeV of energy in the calorimeter forming a second peak in the calorimeter spectrum. This peak is well below the calorimeter cut of ~ 0.7 ($E_{cal}/p_{central}$), but the tail of this peak does extend beyond the cut and into the electron peak.

If the pion background is also charge-symmetric, the pions remaining after the software cuts would be subtracted away since they're also present in the positron sample. However, a detailed study was performed to see how many pions end up in

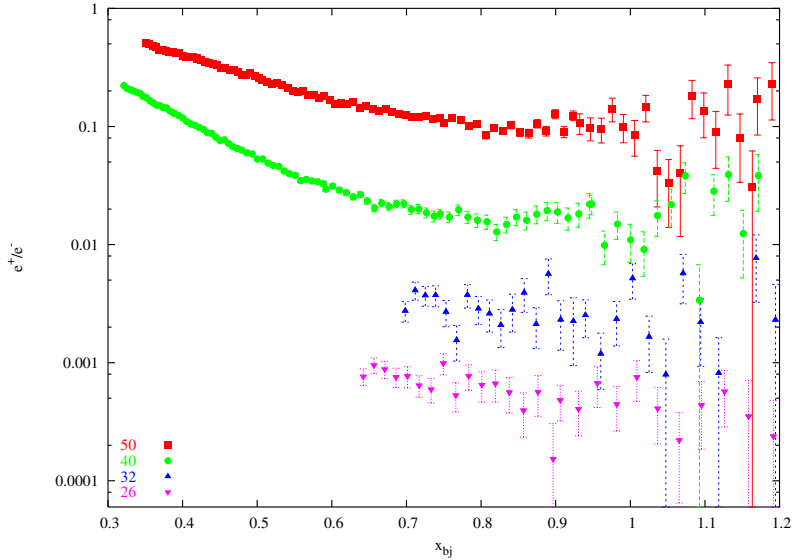


Figure 4.4: Size of the charge symmetric background for copper (e^+/e^-), for the angles where positron data was taken. As this ratio falls quickly with smaller angles, no systematic uncertainty was assigned for $\theta < 26^\circ$.

the data sample. Also, since no positron data was taken at the highest momentum settings at the lowest angles where the π/e ratio was deemed to be very low, it is important to know what the maximum contamination is.

The π/e ratio is largest at the lowest momentum setting of the HMS, where it is 100:1 for heavy targets. To calculate the pion contamination of the electron sample, it is necessary to calculate the pion rejection of the Čerenkov and of the calorimeter. This is done by using a set of acceptance cuts and a strict particle ID cut on one of the detectors to get a clean pion sample. Then, the other detector's particle ID cut (used in the analysis) is applied and the remaining pions are counted.

The problem is that even the “pure” pion sample is contaminated with electrons no matter how tight the cuts. The best solution is to determine the efficiency of

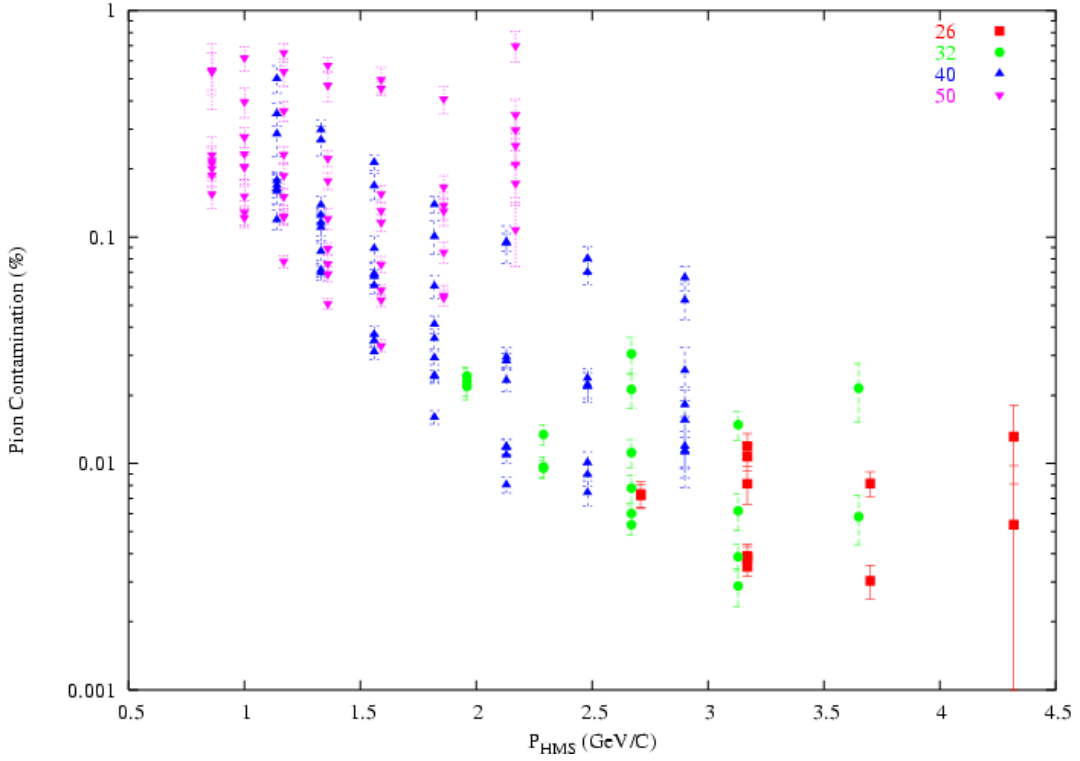


Figure 4.5: Pion Contamination in the HMS for all targets as a function of the central momentum for several θ settings. There appears to be no dependence on angle.

the cut at rejecting electrons and then to calculate how many of the particles in the “pure” pion sample are actually electrons and subtract them. For example, to select a “pure” pion sample using the calorimeter, events with a signal of <0.45 in the E_{cal}/p spectrum are chosen. In order to eliminate possible electrons from this sample, a “good” electron sample is selected (using a very tight Čerenkov cut of 5 photoelectrons) and the fraction of events in this sample that have a calorimeter signal of <0.45 are then subtracted from the original pion sample. Finally, the ratio of the pions obtained in this way to the number that remains after the Čerenkov cut used in the data analysis is applied gives the pion rejection of the Čerenkov.

For the setting with the worst π/e ratio, the pion rejection rate in Čerenkov and calorimeter detectors are 500:1 and 100:1, respectively. This results in a 0.5% pion contamination. At larger momenta, the π/e ratio improves as does the pion rejection of the calorimeter. Since the π/e ratio falls off very quickly as a function of the HMS momentum, positron data were not taken for the highest momentum settings, since the pion contamination as well as the contribution from the charge-symmetric background were thought to be negligible. The degree of pion contamination is shown in Fig. 4.5 and it's small.

The results in Fig. 4.5 represent the upper limit on the pion contamination and we expect that after the subtraction of the charge-symmetric background, it is reduced even further. No correction was made in the analysis for the pion contamination. Since the pion background is very small, we assign it a 50% uncertainty which results in a 0.2% systematic uncertainty in the cross-section at the $x > 1$ settings.

4.3.3 Cryogenic Target Aluminum Cell

The cryogenic targets are liquid and contained inside of cylindrical aluminum cells often called “tuna cans” because of their shape. The cell walls are ≈ 0.12 mm thick (see Table 3.3) and have a density of 2.699 g/cm 3 . This constitutes a significant fraction of the total target thickness and results in a large contribution to the measured yield: $\approx 10\%$ for ^3He and $\approx 20\%$ for ^4He , ^2H at $x < 1$ and as high as 80% for x as it approaches A (see Fig. 4.6). This means that a significant fraction of the electron

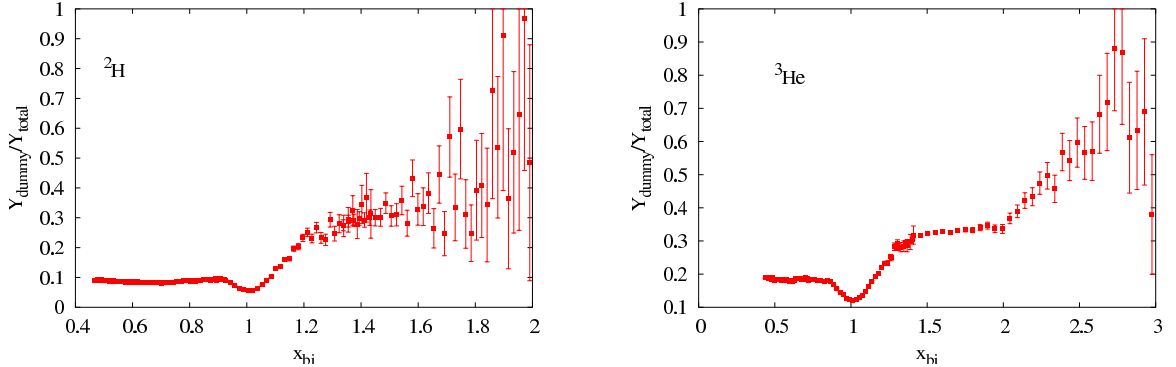


Figure 4.6: Relative contribution from Al end-cap to the cryotarget cross sections for ^2H and ^3He . The fraction approaches 1 at $x \approx A$, as expected.

counts detected come from electrons which scattered from the walls of the cryogenic target container instead of the cryogenic target material. This yield is measured directly by taking data on an empty aluminum target, a.k.a. the “dummy” target. There exists only one dummy target and the data collected with it were for all the cryogenic targets. The dummy target consists of two aluminum plates, thicker than the walls of the cryogenic target cylinders, which reduces the data collection time. The dummy target yields must be scaled by the dummy wall thickness before it is subtracted from the cryogenic target yield. The ratios of the wall thicknesses of the dummy target relative to the cryogenic target cells are listed in Table 4.2.

These ratios are known to within 2-3%. The dummy and cryogenic target data are subjected to identical cuts and the charge symmetric background is subtracted from the dummy data in the same way as it is from the cryogenic data. Finally, the dummy yield is subtracted from the data yield.

An additional correction is applied to the dummy to correct for energy loss due to

Table 4.2: Ratio of dummy to cryotarget wall thicknesses.

Target	Loop	Ratio ($\frac{t_{dummy}}{t_{cryo}}$)
¹ H	2	7.757±0.167
² H	3	7.815±0.231
³ He	2	7.757±0.167
⁴ He	1	7.079±0.228

external radiative effects. The dummy's thickness is several times the radiation length of the normal cryogenic target walls, which means that the radiative effects need to be calculated separately for both cases. The ratio of the two radiative corrections is applied as a weight to each event as it's binned for runs taken with the dummy target. A cross-section model is used to calculate this correction and it is on the order of a few per cent. We believe our knowledge of this correction to 10-20%, implying a contribution 1% to the systematic uncertainty of the cross section. The size of the external radiative correction is shown in Fig. 4.7.

Since the dummy contribution to the cross section depends on x , a constant systematic uncertainty could not be assigned. Instead, an error of 3% of the size of the dummy contribution is used. This ranges from 0.3% to 2.4%.

4.3.4 Boiling of the Cryogenic Targets

During production running with cryogenic targets, the $80\mu\text{A}$ beam is incident on a $2\times 2\text{ mm}^2$ area, depositing on the order of 100W of heat into the target (130W for ²H, for example). If enough energy is absorbed by the cryogenic target, its density

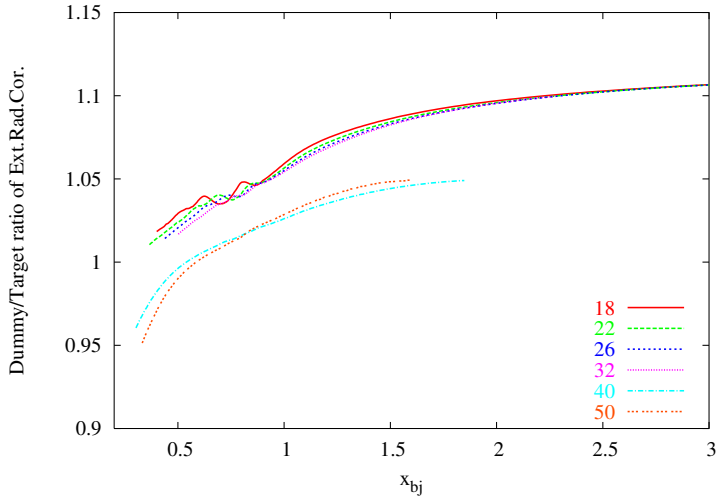


Figure 4.7: Ratio of the sizes of external radiative corrections for the aluminum dummy and the cryogenic target end-caps. The noticeable decrease in the size of the correction at 40° is due to the electron not passing through both dummy foils at large angles.

can change which has a direct effect on the normalization of the yield. This effect is referred to as 'target boiling.' Data was collected specifically to measure the variation of the cryogenic target densities as a function of beam current. All cryogenic targets were used as well as the carbon target, which should show no current-dependent changes in yield, since it's solid and melts only at 3800K.

Four luminosity scans were taken to obtain data for the calculation of the target boiling correction. There were three scans for the running period with helium and one scan for the deuterium/hydrogen period. The yields of the targets for one of the scans before any corrections were made can be seen in Fig. 4.8. There's an obvious problem: the normalized carbon yield decreases with increasing current - carbon appears to boil when it shouldn't.

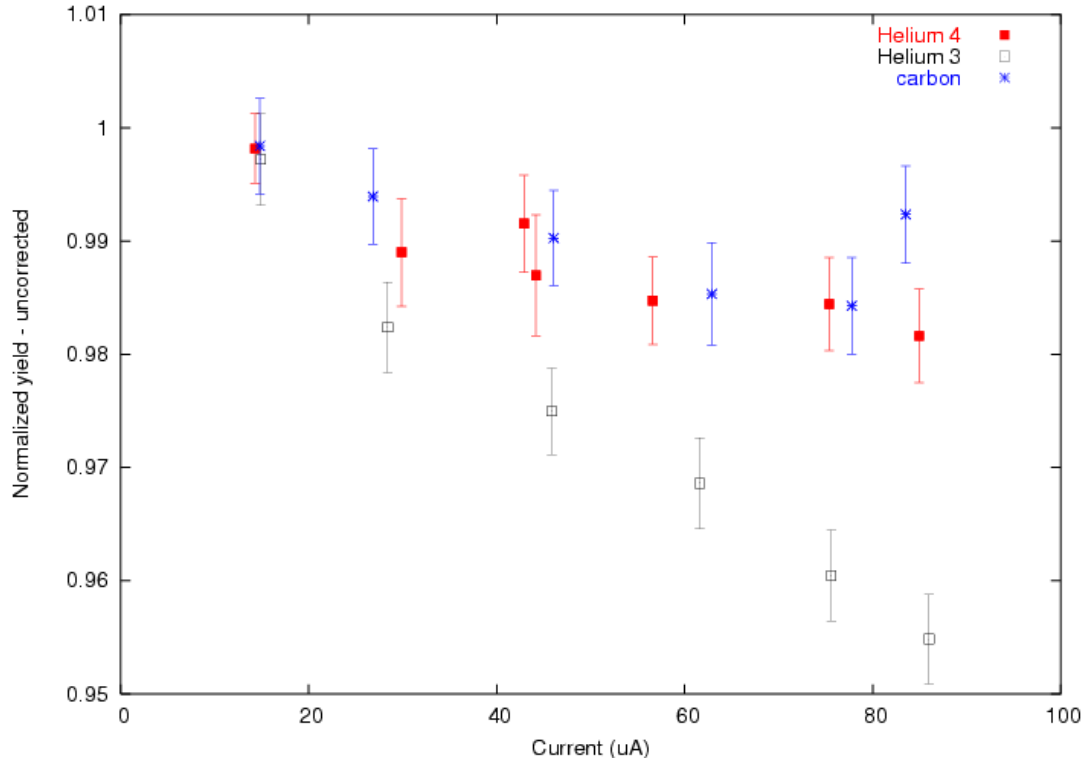


Figure 4.8: Yields from the fourth luminosity scan, in arbitrary units. Target boiling observed for all three targets, including carbon.

After studying this problem at length, this effect was explained by a shift in the BCM calibration. As discussed in Sec. 3.3.3, one set of BCM calibration constants was calculated using all the calibration runs, but some “local” fluctuations are allowed by the errors. The measured yield is related to the measured current, I , as follows:

$$Y_{measured} = \frac{N_{counts}}{Q} = \frac{N_{counts}}{I\Delta t} \quad (4.4)$$

A shift in the BCM calibration results in an offset ΔI to the current, thereby shifting the measured yield. However, if we can determine this offset, then we can extract the

true yield:

$$Y_{actual} = \frac{Y_{measured}}{1 + \frac{\Delta I}{I}} \quad (4.5)$$

The carbon data were fit to this functional form and the necessary offset, ΔI was determined and applied to the cryogenic target data. Fig. 4.9 shows the yields for a carbon luminosity scan after the offset was calculated and applied. The offsets were on the order of a few hundred nA, which is reasonable compared to the size of the residuals for the BCM calibration seen in Fig. 3.5, and are taken into account in the uncertainty of the charge measurement. Once the cryogenic target luminosity runs

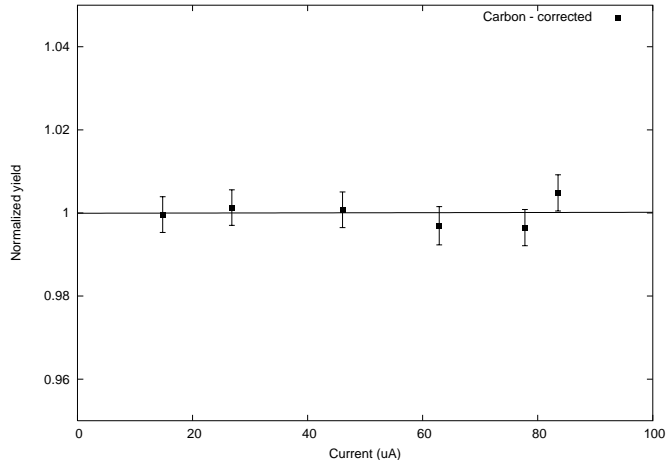


Figure 4.9: Carbon yield for the fourth luminosity scan, corrected for BCM offset. No residual slope remains, which means there's no local target boiling in this solid target.

were corrected for the BCM offsets, the residual slope was taken to be the result of the target boiling. The data were fit to a straight line and the fit parameters (Fig. 4.10) were applied to the cryogenic targets in the data analysis as a density correction. The size of the boiling corrections can be seen in Table 4.3. No target boiling

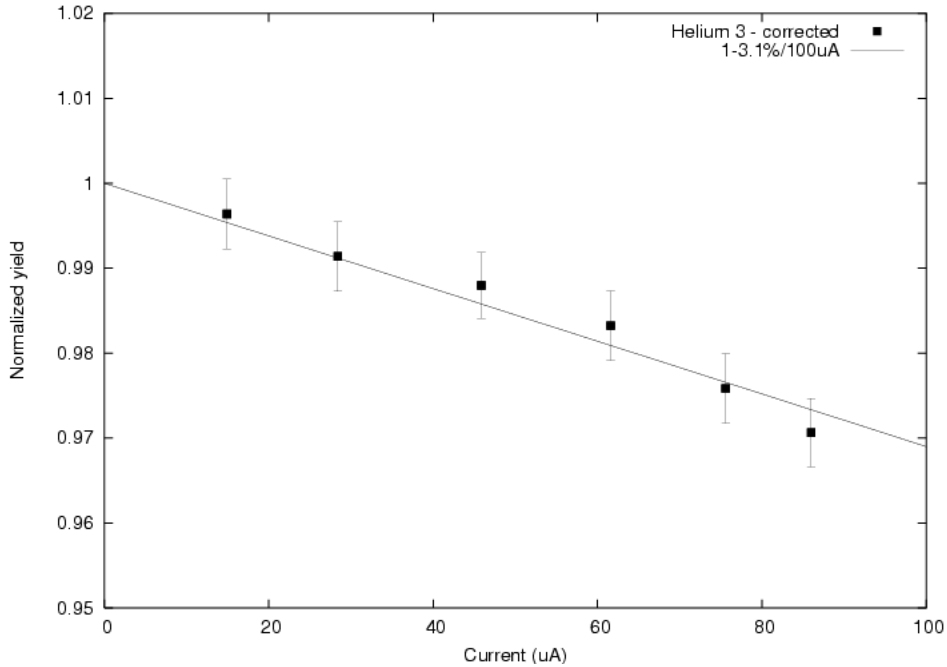


Figure 4.10: Yield for the fourth ${}^3\text{He}$ scan, corrected for BCM offset. The residual slope is the result of local target boiling

was observed for ${}^1\text{H}$ and ${}^2\text{H}$ after applying the BCM offset, which is in agreement with previous experiments in Hall C that used very similar targets and raster. When analyzing the production data, the cryogenic target yields were corrected by applying a factor $C_{boil} = 1 - m_{boil} \cdot \bar{I}$, where \bar{I} is the average beam-on current for a given run and m_{boil} is the slope from the fit to the luminosity data. This correction accounted for the change in the thickness of the cryogenic targets due to the energy deposited by the beam and adds 0.5% systematic uncertainty to the cryogenic target cross sections. While only the helium targets exhibit changes in density with higher currents, the uncertainty is applied to data for all cryogenic targets.

Table 4.3: Cryotarget Boiling Corrections

Target	Correction (%/100uA)
¹ H	0.0
² H	0.0
³ He	-3.10
⁴ He	-1.27

4.4 Extracting Cross Sections

After running the Hall-C replay program, the data are now stored as a series of CERN-LIB HBOOK ntuples [80], which contain event-by-event information on tracks, beam quantities, reconstructed target quantities, timing and PID quantities, and calculated kinematic variables. The analysis code was written in Fortran which is a natural complement to HBOOK ntuples and allows for easy access to and manipulation of the data.

There was a series of central angle and corresponding central momentum settings chosen for production data taking. Data were collected on every target for the same angle and momentum settings. From now on, “data setting” will be taken to denote a certain angle and central momentum setting of the HMS.

4.4.1 Approaches to obtaining σ

There are two approaches to extracting cross sections: the method of corrections and the ratio method. In the first approach, one starts with the measured counts, obtains

a charge-normalized yield (Y_{data} , corrected for charge and detector efficiencies) and then applies a series of corrections to extract the differential cross section:

$$\frac{d\sigma}{d\Omega dE} = \frac{Y_{data} \cdot C_{rad} \cdot C_{bin}}{\Delta E' \cdot \Delta\Omega \cdot N_{scatterers}} \quad (4.6)$$

where C_{rad} is a correction due to radiative effects, C_{bin} is a bin-centering correction, $(\Delta E' \cdot \Delta\Omega)$ is the phase space, and $N_{scatterers}$ is the number of scattering centers in the target. The hard part of this process is obtaining the correction factors.

The ratio method requires the same correction factors, but the idea behind it is different. The goal is to take a Monte Carlo yield and apply effects that appear in the data, such as radiative corrections or spectrometer acceptance. If the experimental effects are properly simulated, the yields from the Monte Carlo and the experiment will be in agreement and the input cross section model will be a good representation of the measured cross section. This is equivalent to:

$$\frac{\sigma_{data}^{born}}{\sigma_{model}^{born}} = \frac{Y_{data}}{Y_{MC}} \quad (4.7)$$

where Y_{data} is the charge normalized data yield integrated over the acceptance of the spectrometer, Y_{MC} is the Monte Carlo simulated yield, σ_{model}^{born} is the Born cross section model (description follows in Sec. 4.4.14), and σ_{data}^{born} is the quantity we're interested

in. If the acceptance function, A , is known, then the data yield can be simulated via

$$Y_{MC} = N_{scatterers} \cdot \int_V A(V) \sigma^{model} R(V) C_{det} dV, \quad (4.8)$$

where A is the acceptance function of the spectrometer (discussed in Sec. 4.4.9), C_{det} are kinematic-dependent detector efficiencies, σ_{model} is a cross section model, V is the volume of the phase space, and R is radiative effects that are also present in the data.

While the first method is more intuitive and easier at the beginning of the analysis process (before a good model of the cross section is obtained), the code associated with it can quickly become extensive, difficult to maintain, and not transparent to the outside observer. Also, the first method assumes that all of the corrections factorize and can be calculated and applied separately. While the cross sections were obtained using both methods and were found to be in excellent agreement, the ratio method is more reliable and the final results quoted will be those obtained with this method. The subsequent sections will outline the procedures followed to obtain cross sections and the processes for calculating the various corrections.

4.4.2 Obtaining Yields

The first step to extracting a cross-section is to obtain a charge-normalized data yield. For a given data setting, a list of all the data runs for each target is made and the ntuples are opened and read in one at a time. Each ntuple is cycled through event by event, and electron as well as acceptance cuts are applied. If the event passes all

the cuts, it is then placed into a 1-D histogram, binned in x_{bj} , which is calculated from θ and E' , which in turn are calculated from x'_{tar} , y'_{tar} , and δ . To obtain a yield for a given run, i , the following is used:

$$Y(i) = \frac{N(i)}{Q(i) * Eff(i)} \quad (4.9)$$

where $Q(i)$ is the accumulated charge for a given run and $Eff(i)$ is the product of several efficiencies (computer live time, fiducial efficiency, prescale factor). One possibility is to store each run in a separate histogram, which would be combined by way of an error-weighted mean with

$$Y = \frac{\sum(Y_i/\sigma_i^2)}{\sum 1/\sigma_i^2}. \quad (4.10)$$

Poisson statistics are used to determine the error on the yield, which assumes $\sqrt{N} \ll N$. However, since statistics are limited in some bins, we use a different way of combining runs that is a better application of Poisson statistics when there are few events:

$$\langle Y \rangle = \frac{\sum_i N(i)}{\sum_i Q(i) \cdot Eff(i)}. \quad (4.11)$$

This method acknowledges the fact that the divisions between runs are arbitrary and treats all the runs at a given setting as one long data taking run. As the counts from each run are placed into the histogram, we also keep a running total of the quantity

in the denominator, the efficiency-corrected accumulated charge. The efficiencies included in this total are those that do not vary with kinematics, but are constant for a given run (e.g. dead time, trigger efficiency).

4.4.3 Electronic Dead Time

Once a trigger is formed in the HMS, the gate is activated, and if another event arrives, it will be ignored. This is the main source of electronic dead time. The events in the HMS occur randomly in time and obey Poisson statistics. For a mean particle rate R , the probability for detecting n events in time t is given by:

$$P(n) = \frac{(Rt)^n e^{-Rt}}{n!} \quad (4.12)$$

with the probability distribution for the time between events given by:

$$P(t) = R e^{-Rt} \quad (4.13)$$

If an event produces a trigger and is accepted, no new events can be accepted for time τ , which is the gate width of the logic signal. For small dead times, the fraction of events that will be detected is the probability that the time between events exceeds τ , which gives us the live time, t_{live} :

$$t_{live} = \frac{N_{triggers}}{N_{total}} = \int_{\tau}^{\infty} R e^{-Rt} dt = e^{-R\tau} \quad (4.14)$$

For E02-019, the gates in the logic modules were 40ns with the exception of the hodoscope discriminators, whose width was 50ns. However, the hodoscopes continue to accept signals even if their outputs are active and extend the output signal to 60ns after the most recent hit. The rates for E02-019 ($R \leq 1\text{MHz}$) allow for the live time to be approximated by the first few terms of the Taylor expansion $(1 - R\tau)$, giving $R\tau$ as the dead time. In this approximation, the dead time is a simple linear function of the gate width and can be calculated by measuring triggers of different gate widths and extrapolating to zero dead time. This allows us to calculate the number of triggers lost in time τ , giving the dead time as:

$$t_{\text{dead}} = \frac{N_{\text{lost}}}{N_{\text{total}}} = \frac{1}{N_{\text{total}}} \cdot \frac{N_1 - N_2}{\tau_2 - \tau_1} \cdot \tau, \quad (4.15)$$

where N_1 and N_2 are the numbers of events corresponding to gate widths of 100ns and 200ns (τ_1 and τ_2), and τ is the hodoscope gate width. N_1 was used in the denominator since it was measured directly, and for the small dead times of E02-019, this is a good approximation. The electronic dead time was calculated for each run and was never greater than 0.2%. It was applied as an efficiency (in the form of $1 - R\tau$) to the yield. Since the inefficiency was extremely small, no systematic uncertainty is assigned to it.

4.4.4 Computer Dead Time

Another source of dead time is the data acquisition system, which cannot accept new events while the previous one is being written. It takes about $350\mu\text{s}$ to write the data for an event to storage. When the computer dead time became significant, the prescale factor was increased, so that not all good events were recorded. The computer live time is

$$t_{c.l.t.} = \frac{N_{triggers}}{N_{pretriggers}}, \quad (4.16)$$

where $N_{pretriggers}$ is the number of good triggers sent to the TS, and $N_{triggers}$ is the number of triggers processed and recorded. The prescale factor was adjusted throughout the data taking to keep the dead time $<20\%$. The final correction factor for the computer live time includes the prescale factor.

4.4.5 Trigger Efficiency

Not all good electron events form a trigger since the detectors are not 100% efficient. The trigger, discussed in Sec. 3.7, is made up of 2 components, which are ORed together. Both components have particle identification elements in them as well as a scintillator trigger. Since the software cuts in the analysis are more strict than the PID in the trigger, we correct for the inefficiency at the software level. However, there's still an inefficiency associated with the scintillator trigger, SCIN or '3/4'. The SCIN trigger requires hits in three scintillator planes for a track. The effi-

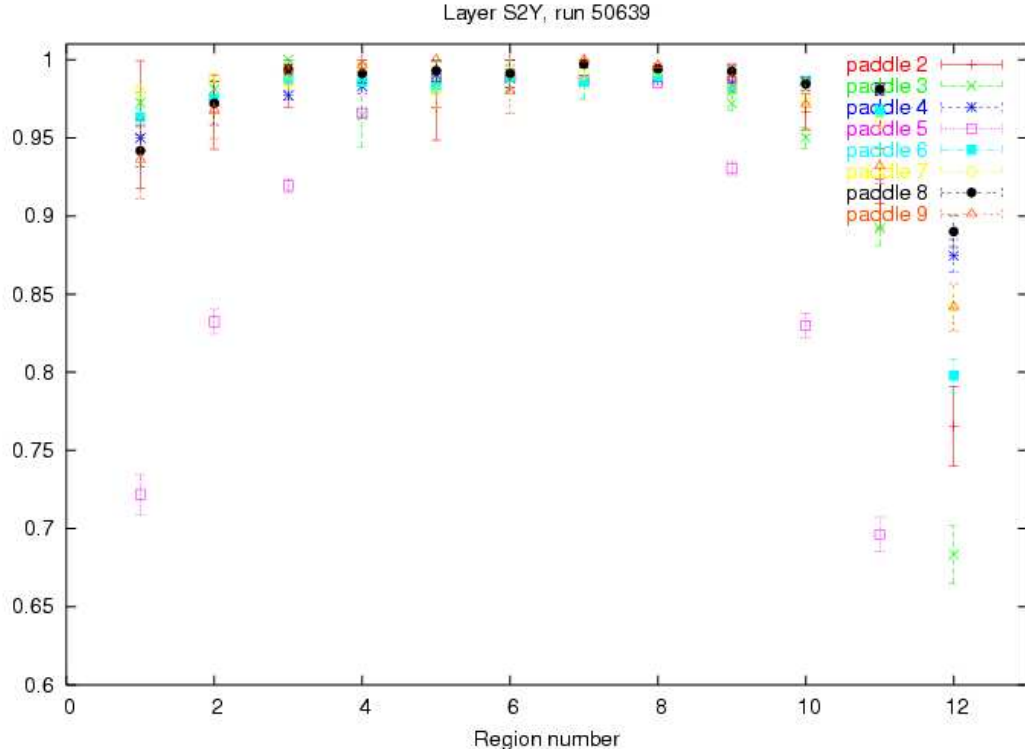


Figure 4.11: The fractional efficiency, '3/4', for the paddles of the fourth layer of the hodoscope detector. The paddle was divided into 12 equally sized regions and the 3/4 efficiency was calculated for each using the same method as for the whole detector. The efficiency shows a fall-off at the edges of the paddles. This effect comes from the attenuation of the signals from events at the other end of the scintillator pads, which are not always detected by the aging PMTs.

ciency is calculated separately for each plane as a ratio between the number of events that fired a given plane and the number of events that should have fired it. Each event is examined and if it produced a hit in the other three scintillator planes, the running sum in the denominator is incremented. If that event also fired the plane being examined, then the total in the numerator is also incremented.

The efficiency for the entire detector is then determined using the possible permutations of three planes firing. This efficiency was found to be constant at $99.3 \pm 0.05\%$

for runs at $x < 1$ kinematics, and decreased for $x > 1$ runs. This trend was investigated and it was determined to be the effect of aging PMTs, as the efficiency was higher in previous years. The efficiency of small regions of the scintillator paddles was calculated and it was found that the center regions are almost 100% efficient and the efficiency decreases as one moves toward the ends of the paddles (Fig. 4.11). The PMTs at both ends of a given scintillator paddle need to fire in order to count as a hit in that plane. A signal from an event at the end of the paddle gets attenuated on the way to the PMT at the opposite end and the signal may fail to fire the discriminator. The runs at $x > 1$ kinematics don't populate the entire focal plane, but rather tend to live near the edges of the acceptance, which is why they have a decreased SCIN efficiency. This event distribution also results in a correlated inefficiency, where a low efficiency from edge events in the 1Y plane is combined with an even lower efficiency for the same events in the 2Y plane, as they are even closer to the edges of the detector. However, since this is a position-dependent effect, it is corrected for with a position-dependent acceptance function described in Sec. 4.4.9.

This overall trigger efficiency is determined by the ELLO leg of the trigger, which has a higher efficiency than the ELHI leg, given that STOF (2/4) and SCIN (3/4) are correlated. Working out an expression for ELLO using the diagram in Fig. 3.20, we find that the efficiency is given by $\text{ELLO} = \text{STOF} * \text{PRLO} + \text{SCIN} * (1 - \text{PRLO})$. The PRLO efficiency was determined to be 99.95% using elastic scattering data, and calculating the ELLO efficiency run-by-run, it was found to be $99.7 \pm 0.1\%$, which some

decrease for $x > 1$ similar to the behavior of the SCIN efficiency.

4.4.6 Tracking Efficiency

A good event must not only fire the electron trigger, but also reconstruct a good track.

In order to count as good, an event must fire the trigger, have 'forward going' time of flight, and have fewer than 15 hits in one of the chambers, but at the same time have enough hits to resolve the left-right ambiguity (not only which wire detected the hit, but which side the particle passed on). Events with more than 15 hits are discounted on the assumption that those hits are generated by electrons scraping the dipole exit window and creating a shower of particles. The tracking efficiency is calculated by taking the number of good tracks formed and dividing by the events with good hits that should have formed tracks.

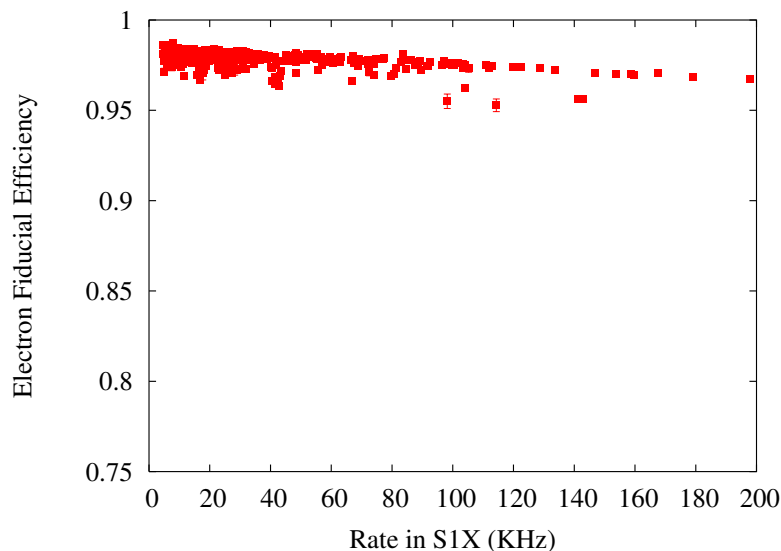


Figure 4.12: HMS Tracking efficiency as a function of rate in S1X. Lower efficiencies were a result of higher rates.

The tracking efficiency is calculated by selecting events within a small region around the central ray (fiducial cut) and applying a particle ID cut. The fiducial cut selects events from the region where signal to noise ratio is the largest and the particle ID cut rejects background events. Pions are able to dissipate energy through elastic collisions or molecular excitations in addition to ionization, making their ionization cross section lower than that of electrons. This results in a lower tracking efficiency for pions.

Any events within the fiducial region that fire the Čerenkov (0.5 or more photoelectrons) and calorimeter ($E \geq 0.7 \cdot p_{track}$) should form a track. The fraction of those that do form a trigger give the tracking efficiency. The tracking efficiency for E02-019 is shown in Fig. 4.12. The efficiency is calculated for every run and the yields are corrected for it. A systematic uncertainty of 0.5% is assigned to the tracking efficiency based on its variation with the event rate.

4.4.7 Detector Cut efficiencies

The Čerenkov and Calorimeter detectors both have momentum dependent efficiencies and corrections must be made for these dependences.

The Čerenkov detector has two elliptical mirrors and the region where they meet as well as their edges have lower efficiencies than the rest of the detector. The Čerenkov was run at 0.35 Atm for this experiment to raise the momentum for which the pions fire it (4.2 GeV/c), and the low pressure decreased its efficiency. Data on elastic ep

scattering was used to select pure e^- samples to parametrize the Čerenkov efficiency as a function of δ (% offset from central momentum, correlated with vertical position) as well as the central momentum setting of the HMS. This correction was applied to each event in the analysis. The shape of the Čerenkov efficiency function is shown in Fig. 4.13. A systematic uncertainty of 0.2% was assigned to this efficiency.

The calorimeter cut ($E > 0.7 \times p$ the position of the electron peak) is also not a 100% efficient and its ability to reject pions depends on the energy resolution, hence the central momentum setting of the HMS. From past experiments [33], the resolution is known to be $6.5\%/\sqrt{E}$ for the HMS calorimeter. The efficiency was found to be fairly stable for higher momenta, but was fit to a second order polynomial for lower momenta. This gave a calorimeter efficiency of $\approx 99.7\%$ for the lowest momentum setting (0.86 GeV/c). For momenta above 1.7 GeV/c, a constant efficiency of 99.895% was used. The variation in the calorimeter efficiency over the kinematic range of the data was minimal and therefore no systematic uncertainty was assigned.

4.4.8 Energy Loss Corrections

The incoming and scattered electrons can lose energy through interactions in the target. The energy of the incoming electron can be lower than the measured beam energy at the vertex, and likewise, the measured energy of the detected electron can be lower than its energy at the vertex. The calculated physics quantities in the analysis engine are corrected for an average energy loss, while spectrometer-related quantities

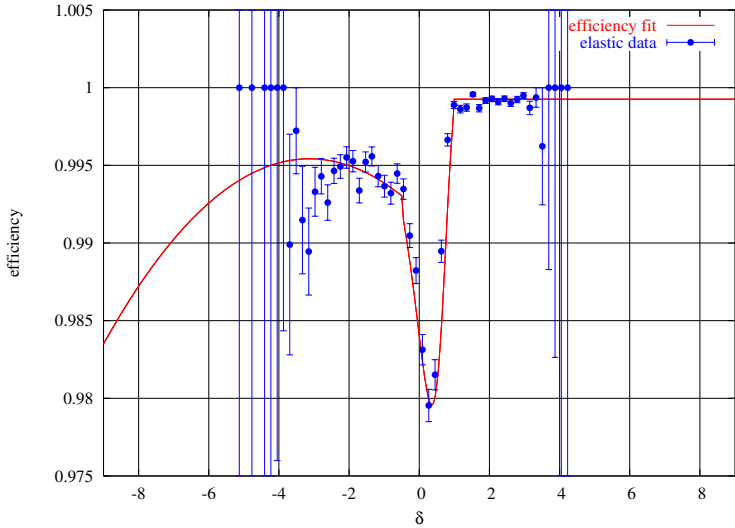


Figure 4.13: Čerenkov efficiency as a function of δ ($\Delta p/p$) for a Carbon run at 4.35 GeV/c and the corresponding parametrization. There are three different parametrizations: one for $\delta < -0.45$, another for $\delta > 0.99$, and a third for $-0.45 \leq \delta \leq 0.99$.

are not. For example, x is calculated using the corrected incoming and scattered electron energies, but if one performs the physics analysis in terms of δ (a common practice), then any quantities calculated from it (i.e. not using the ones already in the engine) need to be corrected for energy loss.

The energy loss is a result of the charged particle interacting with matter. The incoming electron loses energy in the cryotarget cell walls (for example) and in the target material it traverses before the scattering vertex. The scattered particle passes through the remainder of the target material, which for solid targets depends on the scattering angle, then the target-chamber exit window, the air gap and finally, the entrance window to the spectrometer. Since the energy loss occur after the beam energy measurement and before the scattered particle is detected, an energy loss

correction must be applied.

The energy loss is calculated by using the Bethe-Bloch equation [81], and the energy loss is parametrized in terms of momentum transfer with the assumption that the scattering event takes place in the center of the target.

One energy loss correction was applied to the beam energy for the entire experiment since it was found to be fairly constant. That correction is 1 MeV, giving a beam energy of 5.766 GeV. The corrections made to the energy of the scattered electron were of the same order. The corrected momentum was calculated since some of the efficiency corrections are parametrized as functions of momentum. The effect on the cross-section was negligible.

4.4.9 Monte Carlo Yield

There are two analysis procedures needed to account for the finite acceptance of the HMS: software cuts and a model of the spectrometer acceptance. The first method involves cutting on the spectrometer quantities listed in Table. 4.4. These cuts are selected to reject events that did not originate in the target and also to select a region where the reconstruction matrix elements are well known.

For a model of spectrometer acceptance, a simulation of electrons going through the HMS is required. In the simplest picture, spectrometer acceptance can be defined as the probability that an electron event within a certain phase space (defined by δ , x'_{tar} and y'_{tar}) will be accepted. Since the HMS can only detect events within

Variable	Cut
$\text{abs}(\delta)$	$\leq 8 \%$
$\text{abs}(y'_{tar})$	≤ 0.12
$\text{abs}(x'_{tar})$	≤ 0.04

Table 4.4: Acceptance Cuts used in the analysis for both data and MC.

a limited range around the central momentum (ideally, $\pm 15\%$) and angle setting (± 30 mr), most of the events will be lost at the edges due to things like scraping the dipole upon exit or hitting the collimator. This is modeled with a Monte Carlo, with the acceptance being defined as the number of particles that are successfully transported through a model of the spectrometer.

The Hall C single arm Monte Carlo generates events uniformly distributed in x, y, z, δ, θ , and ϕ . The particles are then transported through the magnets of the HMS, which are modeled using the COSY INFINITY program. Using a list of magnet parameters such as their positions, dimensions and field maps, COSY generates a forward matrix that projects rays at the target to the focal point. The position of each event is calculated for several points: beginning and end of each magnet as well as position 2/3 of the way through the first two quadrupole magnets. The tracks in the focal plane are recorded for all particles which make it all the way through the detector stack. The focal plane quantities are determined using the target quantities

in the following way:

$$a_{fp} = \sum_{i,j,k,l,m} F_{ijklm}^x (x_{tar})^i (x'_{tar})^k (y_{tar})^j (y'_{tar})^l \delta^m \quad \text{for } (1 \leq i+j+k+l+m \leq N) \quad (4.17)$$

where N is the order of the expansion (6 for the HMS) and F_{ijklm}^x is one column of the forward transport matrix (there are 4 total, one for each focal plane variable).

In reality, the cross section (and the acceptance function) is a function of 6 variables: $x, y, z, x', y',$ and δ . However, it is possible to simplify it by averaging over the behavior of several variables. For example, we can average over $x, y,$ (related to the size of the rastered beam) and z (related to the target length) for a given target. We simplify further by producing a separate acceptance ntuple for every setting of the HMS and each target geometry. Since the central angle of the spectrometer is fixed for a given setting, x' and y' can be converted to the lab angles, and integrated over ϕ , so that finally, $A=A(\delta, \theta)$. In order to reproduce the measured yield, it's necessary to calculate the number of scattering centers for a given target, $N_{scatterers}$, and the acceptance integral must be weighted by the cross section and detector inefficiencies, giving:

$$Y_{MC} = N_{scatterers} \int A(\delta, \theta) \sigma_{model}^{rad}(\delta, \theta) C_{det} p_{HMS} d\delta d\Omega, \quad (4.18)$$

where the subscript *model* and superscript *rad* denote the radiated model cross section evaluated at a given point, $p_{HMS} d\delta$ is equivalent to dE' , and C_{det} is the combined kinematic-dependent detector efficiency, which includes calorimeter and Čerenkov

efficiencies.

The shape of the acceptance function is shown in Fig. 4.14 as a function of δ and y'_{tar} . The variable y'_{tar} is often used in place of θ_{lab} , since it's the arctan of the angle the electron track makes with the central ray of the HMS in the horizontal plane. The complete definition of θ_{lab} , or just θ , is:

$$\theta_{lab} = \frac{\cos(\theta_{HMS}) + y'_{tar} \sin(\theta_{HMS})}{\sqrt{1 + x'^2_{tar} + y'^2_{tar}}} \quad (4.19)$$

where θ_{HMS} is the central angle of the spectrometer. The complete definition of θ was used in this analysis, since at small angles, the contribution from x'_{tar} cannot be ignored.

Binning the unweighted MC counts in the exact same manner as the data, automatically generates the acceptance function. The weighted, simulated yield in a particular bin is given by:

$$Y_{MC} = N_{scatterers} \sum_{events} \sigma_{model}^{rad}(\delta, \theta) C_{det} p_{HMS} (\Delta\delta\Delta\Omega)_{bin}, \quad (4.20)$$

where $\Delta\delta\Delta\Omega_{bin} = (\Delta\delta\Delta\Omega)_{bin}^{gen} / (N_{gen}^{bin})$ represents the relative phase space for a given event. The generated solid angle depends on the generation limits in x'_{tar} and y'_{tar} , the in- and out-of-plane angles. For this analysis, 5×10^6 events were generated for each acceptance ntuple, with the generation limits of $\delta \pm 15\%$, $x'_{tar} \pm 100$ mr, and $y'_{tar} \pm 50$ mr.

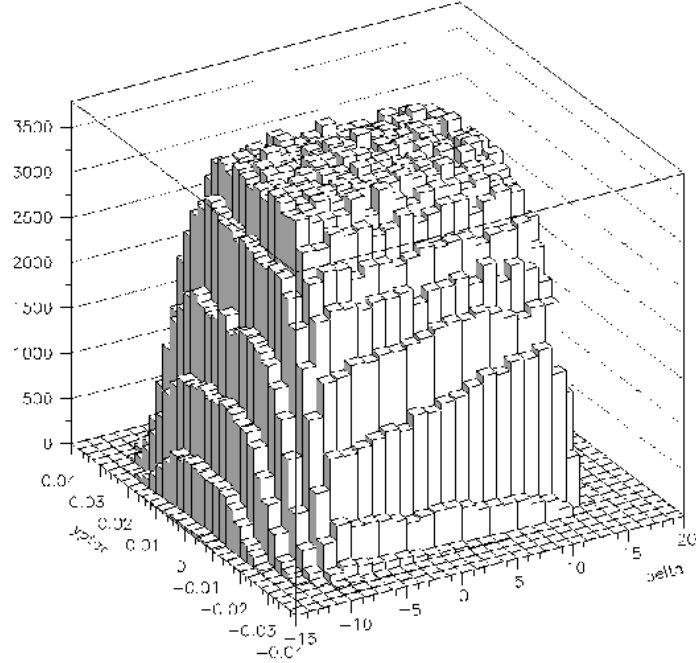


Figure 4.14: Shape of the acceptance of the HMS from Monte Carlo in δ and y'_{tar} (unweighted MC counts are shown on the vertical axis). The variable y'_{tar} is often used in place of θ_{lab} as it is the slope of the track in the y -direction (horizontal) and is therefore the arctan of the angle the track makes with the central angle of the HMS. This is not a good practice for small angles, where the contribution from x'_{tar} to the correct calculated scattering angle is non-negligible.

It was discovered, when combining data from adjacent HMS momentum settings, that the acceptance function does not perfectly model the acceptance of the detector and there's an additional δ -dependent effect. A polynomial fit from a previous experiment [82] was used since it described the data well (Fig. 4.15). This correction was applied on an event-by-event basis in the Monte Carlo. A 1% scale and a 1% relative uncertainty were applied to the acceptance based on experience from previous experiments in the Hall.

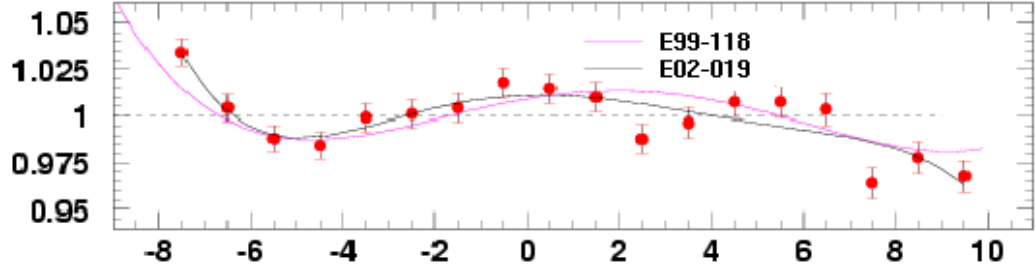


Figure 4.15: Ratio of Data to Monte Carlo vs. δ . This is a residual acceptance effect, independent of momentum or angle with 2 fits, one from our experiment, and the other from a different analysis [82].

4.4.10 Bin-Centering

The data in this experiment were taken at several angles. Because the HMS has a finite acceptance around the central angle setting, the counts have some distribution in θ_{lab} for a given x bin. This means that the measured data yield in any given (x, θ) bin is an average value rather than the yield at the center of the bin. These are not the same unless the cross section has a linear dependence on θ . Instead of correcting the data and moving each event to the center of its bin using a cross section model, the correction was applied to the MC. By putting in a cross section model with the same angular dependence as the data into Eq. 4.20, the simulated yield is averaged over the acceptance in the same manner as the data.

To determine the systematic uncertainty associated with the choice of the bin-centering model, it was varied and the experimental cross sections were recalculated. The input model was altered in two ways for this test: in the first, the calculated

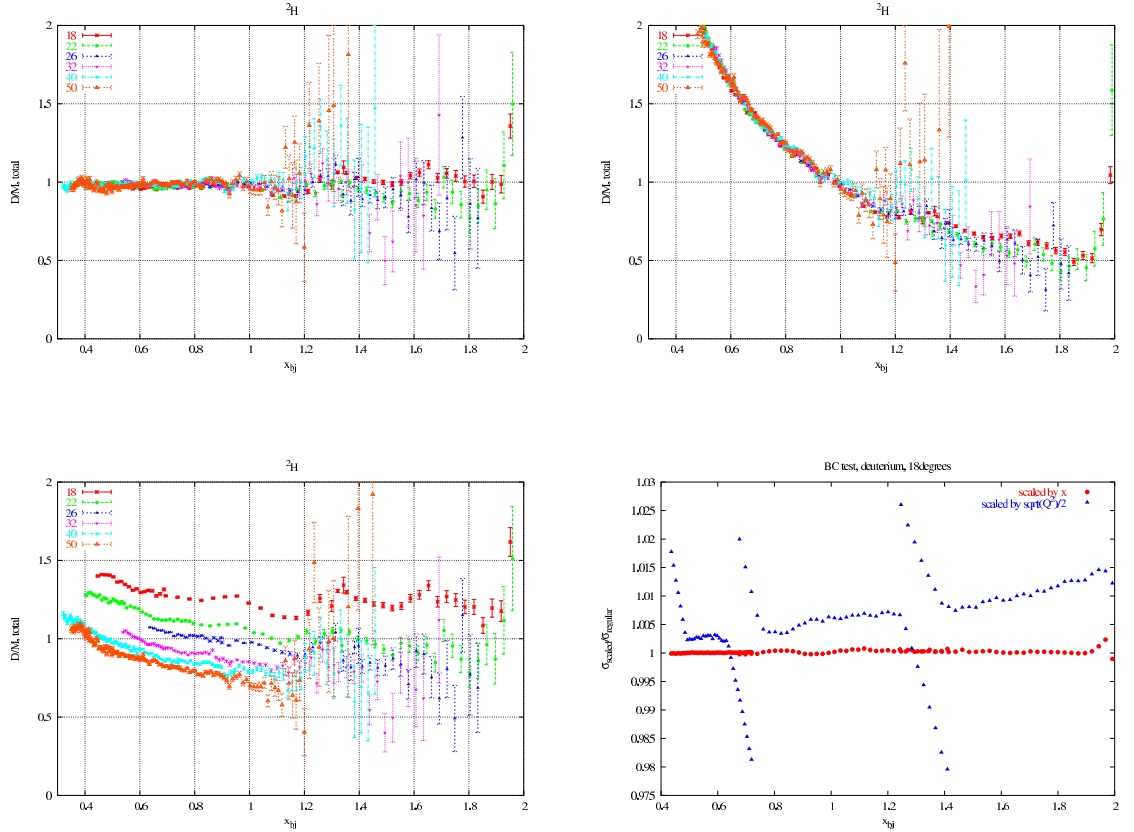


Figure 4.16: The top left plot shows the data to model ratio before the bin-centering test. The top right and bottom left plots show the effect on that ratio if the model is multiplied by x in one case and $\sqrt{Q^2}/2$ in the other case. The scale factor is a gross overestimate of the disagreement between data and optimal model. The bottom right plot shows ratio of the experimental cross sections extracted with the altered model to those extracted with the optimal model. There are three HMS settings in the 18° data set, and the features at the edges of the settings for the $\sqrt{Q^2}/2$ test are a result of the data being binned in x , where the edge bins do not include events from the whole acceptance.

cross section at each point was multiplied by x ; in the second, it was multiplied by $\sqrt{Q^2}/2$. Fig. 4.16 shows the result for 18° deuterium data. Since the input model was scaled by more than the disagreement between the original cross section model and the data, this variation in the extracted cross section is an overestimate. A conservative uncertainty of 0.5% in the bin-centering model was assigned.

4.4.11 Radiative Corrections

The measured cross sections also need to be corrected for effects from internal and external radiative processes. Internal radiative processes include vacuum polarization, vertex corrections, and internal bremsstrahlung. An electron can also lose energy through bremsstrahlung while passing through the target, which is an external effect.

Fig. 4.17 illustrates external bremsstrahlung. No correction was made for the nuclear elastic contribution.

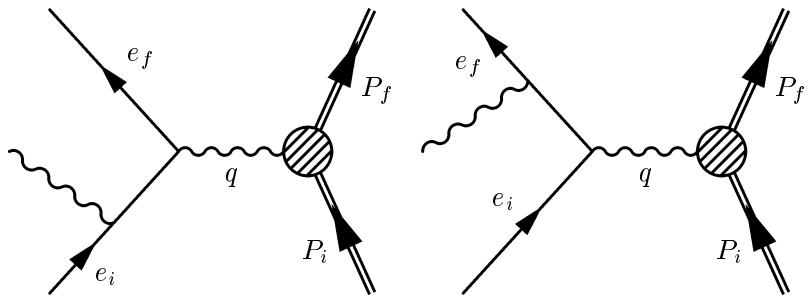


Figure 4.17: The incoming and/or scattered electron can lose energy through bremsstrahlung. The radiative corrections procedure restores events that lose energy in this way to the correct data bin since the event may have ended up in a higher or lower energy bin, depending on when it underwent bremsstrahlung.

The challenge that radiative processes present can be understood by examining

Fig. 4.17. In order to calculate the contribution of, for example, the process depicted on the left hand side in the figure, the cross section must be known for beam energies that are lower than that of the experiment. Similarly, for the figure on the right hand side, the cross section must be known for scattered energies greater than those of the experiment. This requires a realistic cross section model, which was developed for this analysis and is described in Sec. 4.4.14.

In this analysis, the radiative correction was originally calculated with the method described by Stein in [83] using the peaking approximation method of Mo and Tsai [84]. However, this approximation does not do a good job for thick targets at low x and the full 2-D integral needs to be calculated.

The approach adopted was one described in detail by Dasu [85] and used to do radiative corrections for SLAC experiments. In this approach, a complete calculation of Mo and Tsai's formula for external effects is done. An equivalent radiator is used to take into account materials before and after the target, such as air, aluminum target exit window, mylar and kevlar entrance and exit windows for the magnets. Unlike in Dasu's analysis, where the Bardin prescription [86] is used for the internal corrections, Mo and Tsai's approach is used in this analysis.

The radiated and Born versions of the model cross section are used to form the correction factor:

$$C_{rad} = \frac{\sigma_{model}^{rad}(x, \theta)}{\sigma_{model}^{born}(x, \theta)} = \frac{\sigma_{MT}^{i+e}(x, \theta)}{\sigma_{model}^{born}(x, \theta)} \quad (4.21)$$

The subscript MT denotes Mo and Tsai's equivalent radiator calculation, and the su-

scripts i and e refer to the internal and external radiative corrections, respectively.

A cross section model is used to generate a list of Born and radiated cross section

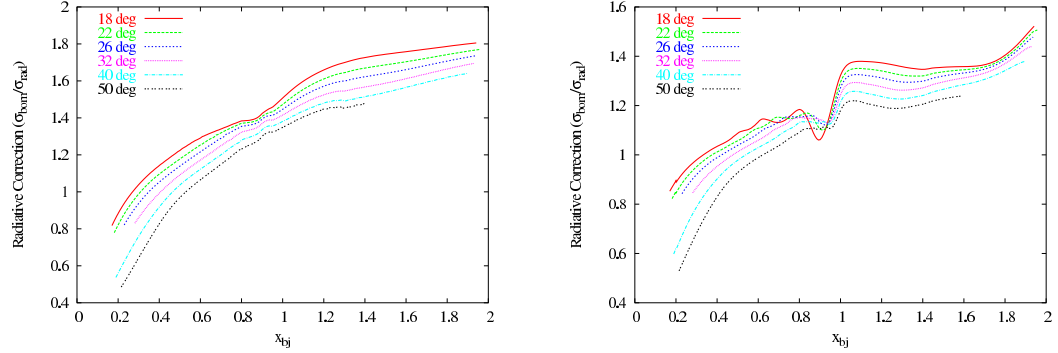


Figure 4.18: Radiative Corrections for ^2H (right) and ^{197}Au (left) at all angle settings. The y-axis shows the size of the radiative correction, which is given by the ratio $\sigma_{\text{born}}/\sigma_{\text{rad}}$.

values in increments 10 MeV for each central angle setting of the HMS. The correction for each data point is interpolated from the two closest points and is applied as a correction to the binned, radiated cross sections.

The size of the correction can be seen if Fig. 4.18. where the ratio of the extracted cross sections with and without radiative corrections is shown.

To determine the systematic uncertainty from the choice of the cross section model used to calculate the radiative correction, the model was scaled by x in one case, $\sqrt{(Q^2)}/2$ in another case, (as was done for the bin-centering uncertainty) and the correction recalculated. At low values of x , the radiative correction is progressively more sensitive to the quasielastic tail with increasing values of Q^2 . The cross section model was calculated for the kinematics of previous experiments using the quasielastic archive [42] and found to be in good agreement in the region around the quasielastic

peak down to Q^2 values of ≈ 0.5 GeV 2 . To determine the uncertainty associated with the quasielastic tail, the quasielastic contribution alone was scaled by 10% (somewhat higher than the level of disagreement between our cross section and the quasielastic archive) and the correction factor recalculated.

A systematic uncertainty of 1% due to the radiative correction model is applied for the entire kinematic range. At low x , this is the combined effect of rescaling the entire model and the quasielastic tail alone, and for $x > 1$, the uncertainty is the result of the model rescaling alone. An additional uncertainty of 1% is included due to the limitations inherent in the calculation, for a total of 1.4% systematic uncertainty.

4.4.12 Corrected Cross Section

Once the measured data yield and the simulated MC yield have been obtained, the experimental Born cross section can be extracted through:

$$\sigma(x, \theta_c) = \frac{Y_{data}}{N_{scatterers} \int \sigma_{model}^{rad}(x, \theta) C_{det} A(x, \theta) d\Omega} \cdot \sigma_{model}^{born}(x, \theta_c) \quad (4.22)$$

where the denominator is the Monte Carlo yield, previously described in Sec. 4.4.9, and the subscript c denotes the central angle setting of the HMS. If the Monte Carlo perfectly describes the spectrometer acceptance and the cross section model used as a weight for the simulated yield agrees well with the data, the ratio in Eq. 4.22 should be about 1. An example of data and MC yields is shown in Fig. 4.19, where the agreement between the two is excellent in the δ -region to which this analysis is

confined.

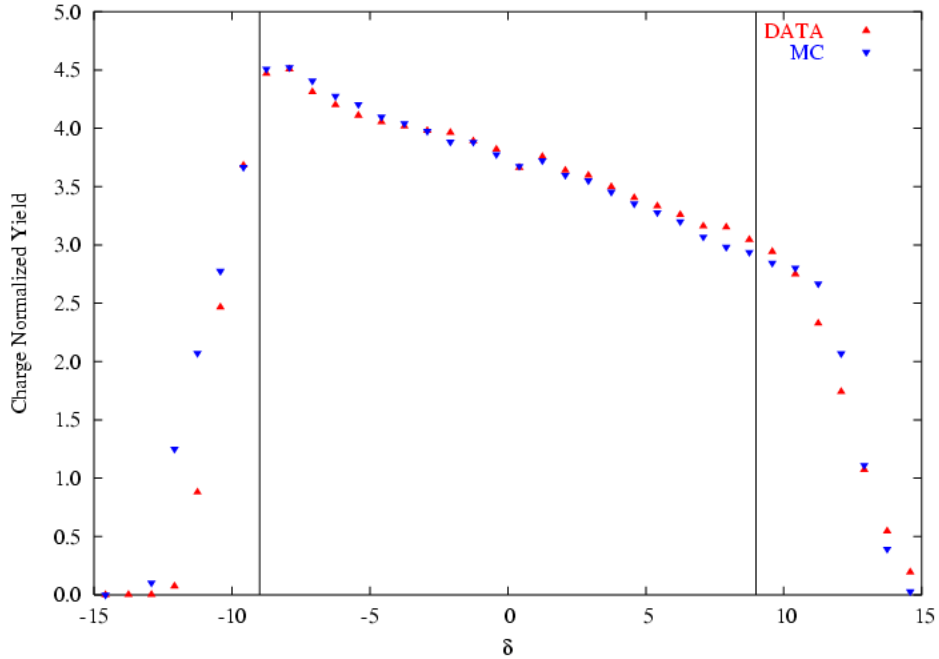


Figure 4.19: Data and MC yields for Carbon, 40° , $p_{HMS}=1.14$ GeV/c, arbitrary units. The vertical lines at ± 9 represent the software cut applied to the data and MC. The discontinuity at $\delta \approx 0$ is the result of a region of decreased efficiency in the Čerenkov. This region corresponds to the overlap between the two mirrors and is well reproduced in the MC.

4.4.13 Coulomb Corrections

It is also important to correctly treat the Coulomb distortion of the electron wave function by the electrostatic field of the nucleus. The nucleus has two effects on the electron: it is accelerated due to the attractive force when in close proximity to the nucleus, increasing the electron's momentum and also, the attractive force focuses the electron wave function.

A distorted wave Born approximation (DWBA) calculation using Dirac wave func-

tions is the correct approach [87] to the problem but it's not a practical solution given the computational load involved. Instead, a local Effective Momentum Approximation (EMA) is used [88].

The first effect is quantified by calculating the shift in the momentum due to the acceleration by the nucleus. The enhancement of the momenta is given by: $k'_f = k_f + \Delta k$ and $k'_i = k_i + \Delta k$, with $\Delta k = -.775V_0/c$, where V_0 is the potential energy of the electron in the center of the nucleus. V_0 is the lowest order of the electrostatic potential inside a charged sphere and is given by

$$V_0 = \frac{-3\alpha(Z-1)}{2R},$$

where R is the radius of the nucleus. Note that $Z - 1$ is used instead of the Z in the given reference, since we're calculating acceleration due to the A-1 nucleus. The nuclear radii used for the different targets are given in Table 4.5. The extra factor of 0.775 [88] comes from the fact that the scattering is distributed over the volume of the nucleus and the potential needs to be modified to reflect the average potential inside a homogeneously charged sphere.

The second effect is the focusing of the electron wave function by the attractive potential of the nucleus and is accounted for with a “focusing” factor, which enters into the cross section quadratically. The wave functions of incoming and outgoing electrons are both enhanced, but the artificial enhancement of the phase space in the shifted cross section cancels the focusing factor of the outgoing electron [90]. The

Target	Radius (fm)
³ He	1.96
⁴ He	1.67
⁹ Be	2.70
¹² C	2.89
⁶³ Cu	4.60
¹⁹⁷ Au	6.55

Table 4.5: RMS charge radii. For heavy targets, the radius is given by $R = 1.1A^{1/3} + 0.86A^{-1/3}$ and previously determined values are used for helium [89].

remaining focusing factor is given by $(k'_i/k_i)^2$.

The complete form of the Coulomb correction is then:

$$C_{coulomb} = \frac{\sigma_{born}(k_i, k_f)}{\sigma_{born}(k'_i, k'_f)} \frac{1}{(k'_i/k_i)^2} \quad (4.23)$$

The size of the correction is shown in Fig. 4.20 for all targets at 18°. The correction is largest for the heaviest target, which for E02-019 is ¹⁹⁷Au, where it reaches 10% for 18°, and 20% for 50°.

There is a 10% uncertainty associated with the Coulomb potential, which needs to be included in the measured cross section. To determine the contribution from this uncertainty to the cross section, the coulomb corrections were evaluated for each target and kinematic setting with a 10% shift applied to the potential. The ratio of this shifted correction to the normal correction was parametrized as a function of x for each θ_{HMS} setting and for each target. Evaluation of this parametrization at any data point gives the systematic uncertainty associated with this correction. The

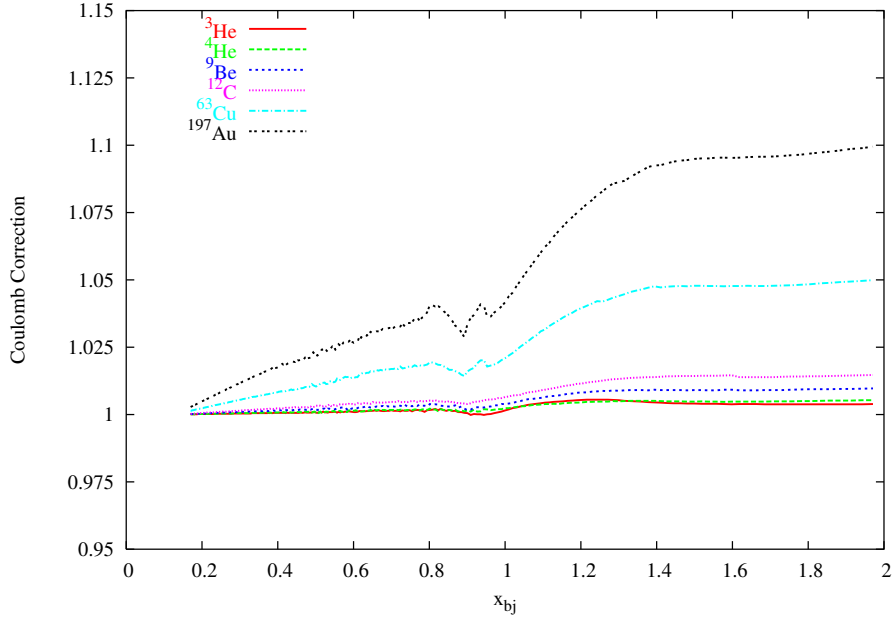


Figure 4.20: Coulomb correction factor for all targets at 18 degrees. The dip around $x_{bj} = 0.9$ is a result of a transition between two different models for the inelastic cross section.

largest corrections and therefore, the largest uncertainties are for ^{197}Au , where the uncertainty at $x > 1$ reaches 0.5% and 2% for 18° and 22° , respectively.

4.4.14 Cross Section Model

The three sets of corrections described above all require an input model of the cross section. For E02-019, the cross-section model consists of 2 parts: a quasi-elastic contribution and a deep inelastic contribution.

The quasi-elastic contribution is calculated from a scaling function, $F(y)$, the off-shell electron-nucleon cross-section, and a kinematic factor, K .

$$\frac{d\sigma}{d\Omega d\nu} = F(y) \cdot (Z \cdot \sigma_p + N \cdot \sigma_n) \cdot K \quad (4.24)$$

The scaling function $F(y)$ used for ${}^2\text{H}$, a variation of the form used in [91], is given by:

$$F(y) = (f_0 - B) \cdot \frac{\alpha^2 e^{-(ay)^2}}{\alpha^2 + y^2} + B e^{-b|y|} \quad (4.25)$$

This form was modified for heavier targets to get:

$$F(y) = (f_0 - B) \cdot \frac{\alpha^2 e^{-(ay)^2}}{\alpha^2 + y^2} + B e^{-(by)^2} \quad (4.26)$$

where the parameters a , b , f_0 , B , and α are fit to the $F(y)$ extracted from the data for each target (see Table 4.6). This is done by taking the data cross section, subtracting the inelastic contribution (calculated using the inelastic part of the model), and dividing out the kinematic factor and the electron-nucleon cross section, which is described in Sec. 2.1.1. After the fit, the iterated model was used as the input to the cross section extraction and the process was repeated until good agreement between the data and the model was achieved for all settings.

	${}^2\text{H}$	${}^3\text{He}$	${}^4\text{He}$	${}^9\text{Be}$	${}^{12}\text{C}$	${}^{63}\text{Cu}$	${}^{197}\text{Au}$
f_0	8.742e-03	5.309e-03	4.020e-03	3.481e-03	3.182e-03	2.874e-03	2.642e-03
B	8.239e-04	2.184e-03	1.345e-03	1.161e-03	1.359e-03	8.866e-04	7.632e-04
a	7.727e-03	2.886e-03	2.699e-03	3.120e-03	3.027e-03	3.096e-03	3.065e-03
b	9.394e-03	1.035e-02	7.494e-03	7.840e-03	7.050e-03	7.094e-03	6.768e-03
α	45.3	64.2	100.2	110.9	137.2	132.4	132.4

Table 4.6: $F(y)$ fit parameters as determined by fitting the experimental scaling function to the form of Eqs. 4.25 and 4.26.

An additional correction to the quasi-elastic model was introduced. Since the

quasi-elastic model is based on y -scaling, it doesn't work perfectly for the largest negative y values, where the low Q^2 data is affected by final state interactions (FSIs) and doesn't scale. A polynomial fit for each target was done for the ratio of the data to the model at large negative y 's ($x_{bj} > 1.4$) to account for this effect.

The inelastic cross section is calculated slightly differently for over the range of x . For $x < 0.8$, parametrizations [92] of the proton and neutron structure functions (F_2^n and F_2^p) are used and they're smeared using the momentum distribution $n(k)$ which is determined from the derivative of $F(y)$ used in the quasi-elastic model cross section via Eq. 2.20. The inelastic cross section is obtained using the resulting nuclear structure functions through Eq. 2.33. A polynomial correction function is then applied to the result to reproduce the shape of the data. This function is different for every target. In the $x_{bj} > 0.9$ region, only the smearing prescription is used with the corresponding $n(k)$ for a given target. For the region where $0.8 < x_{bj} < 0.9$, a weighted average of the two prescriptions is used so that the transition between the two regions is continuous. Once a good model was obtained for the quasielastic region, it was subtracted from the measured data cross section and the resulting inelastic data was compared to the inelastic model. A residual slope in the inelastic data/model ratio was found for $x > 0.9$ for all angles, and it was corrected for with a straight line fit.

The data as well as model cross sections, including quasielastic and inelastic contributions, are shown in Fig. 4.21 for several targets at 18° and 32° .

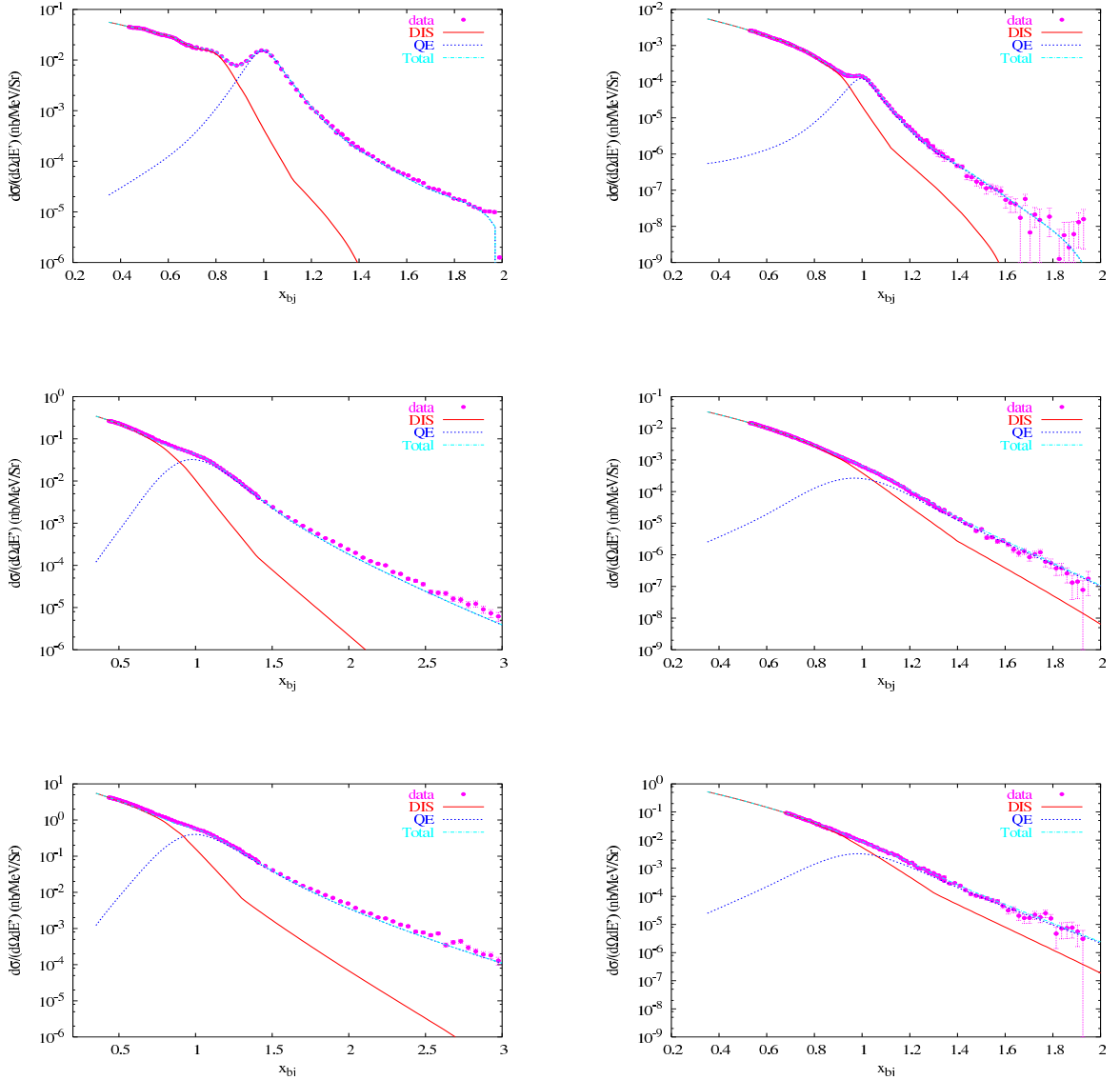


Figure 4.21: Data and model cross section for ^2H (top), ^{12}C (middle), and ^{197}Au (bottom) at 18° (left) and 32° (right). The model cross section is separated into the inelastic and quasi-elastic pieces to show their relative contributions. The rise of the data cross section around $x \approx 2$ for ^2H is the result of elastic electron-deuteron scattering contribution.

Chapter 5

Results

In this chapter, the results will be presented, starting with cross sections and following up with the extracted scaling and structure functions. The sources of systematic uncertainties will be discussed in Sec. 5.8. Throughout this chapter, the results shown will include only the statistical error bars.

5.1 Cross Sections

The measured cross sections are shown in Figs. 5.1-5.3, excluding the Beryllium and Copper targets for space reasons alone. The six sets of data in each plot correspond to the six central angle settings of the HMS: 18° , 22° , 26° , 32° , 40° , and 50° . The Q^2 and E' values associated with the center of the quasielastic peak are shown in Table 5.1 for each central angle setting. The data are plotted as a function of energy loss, ν , and the characteristic quasielastic peak can be seen especially well in the deuterium

data and its evolution as the relative contributions from the quasielastic and inelastic reactions change can also be seen.

Table 5.1: Central Angle settings and corresponding Q^2 values at the quasielastic peak ($x=1$)

θ_{HMS}	E' (GeV)	Q^2 (GeV 2)
18	4.43	2.5
22	3.98	3.3
26	3.55	4.1
32	2.98	5.2
40	2.365	6.4
50	1.805	7.4

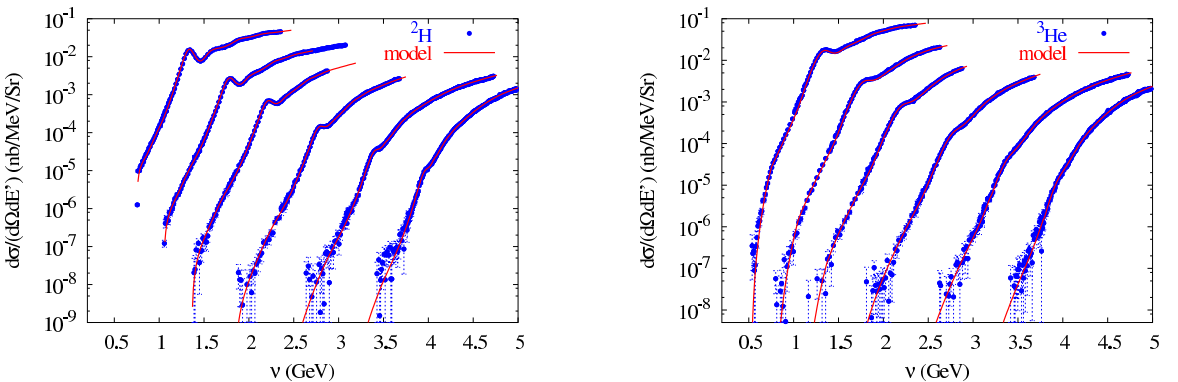


Figure 5.1: ^2H (left) and ^3He (right): experimental cross section and Born cross section model. Errors shown are statistical only.

Fig. 5.4 shows the cross section for Carbon at 32° along with a theoretical calculation by O. Benhar [62]. The experimental cross section is very well reproduced by the calculation, which includes the contributions from Final State Interactions. The FSIs can be seen to be a significant effect at low energy transfers, where they double the total calculated cross section by $x \approx 1.4$ and the contribution continues to grow

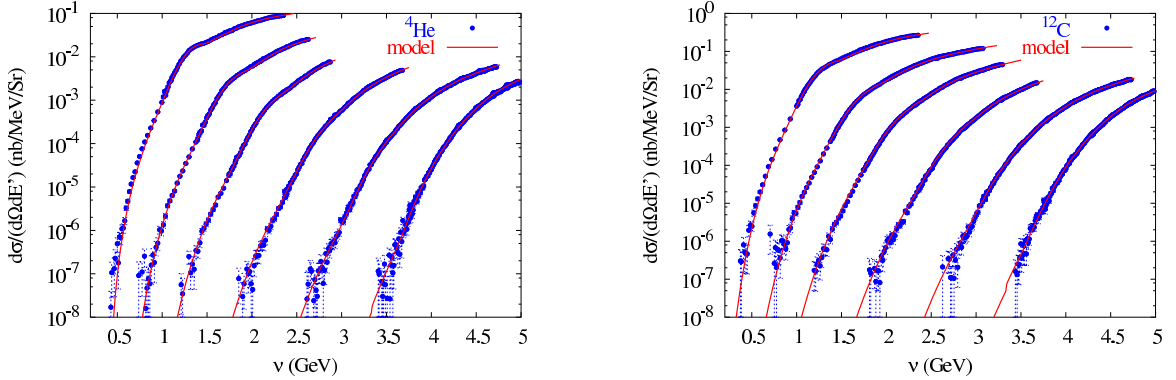


Figure 5.2: ^4He (left) and ^{12}C (right): experimental cross section and Born cross section model. Errors shown are statistical only.

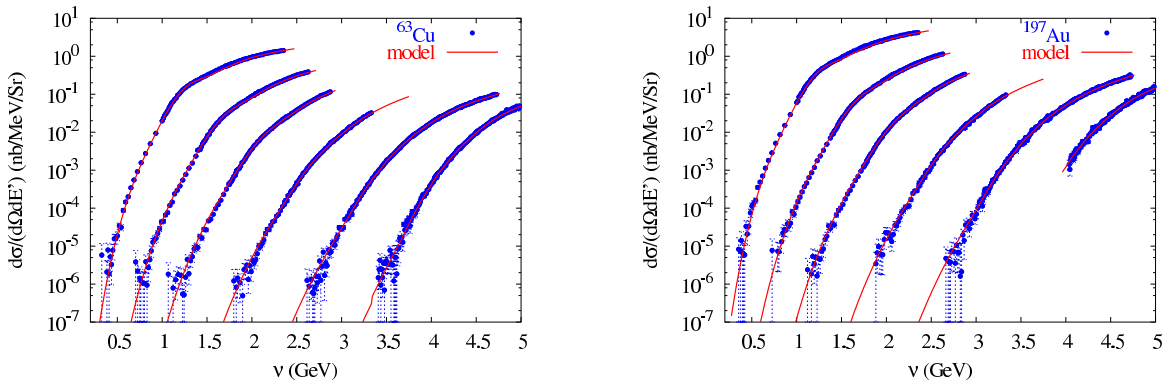


Figure 5.3: ^{63}Cu (left) and ^{197}Au (right): experimental cross section and Born cross section model. Errors shown are statistical only.

with x .

In the work of Benhar et al., the theoretical cross section is calculated using a convolution integral of the form:

$$\frac{d\sigma}{d\Omega d\nu} = \int d\nu' \left(\frac{d\sigma}{d\Omega d\nu'} \right)_{IA} f_{\mathbf{q}}(\nu - \nu'), \quad (5.1)$$

where $f_{\mathbf{q}}(\nu)$ is a folding function that accounts for FSI effects, and $\left(\frac{d\sigma}{d\Omega d\nu} \right)_{IA}$ is the

inclusive cross section in the Impulse Approximation obtained from a nuclear matter spectral function. The spectral function is constructed from two pieces [93]: one coming from the shell model picture and the second from correlations. The former is calculated using a momentum-space wave function for a single particle in a given shell state and summing over all the occupied states. The latter piece is calculated by integrating the correlation contribution from the nuclear matter spectral function [94] with the nuclear density distribution to give the contribution for a finite nucleus.

The FSIs were treated with the Correlated Glauber Approximation [93], which employs the eikonal and frozen approximations. The former assumes that the struck particle moves in a straight line and the latter assumes that the spectator nucleons are fixed. The folding function includes two FSI effects: an energy shift in the cross section and a redistribution of the cross section strength from the quasielastic peak to the region of low energy transfer. The cross sections in this region are very small and decreasing rapidly, so even a small contribution from FSIs results in a significant enhancement. In Benhar's calculation, the FSIs do not disappear at high Q^2 , but rather become constant as the width of the quasielastic peak in ν becomes constant with increasing Q^2 and the folding function contains no Q^2 dependence. This seems to have already happened by the kinematics of 32° and 40° , as can be seen in the second plot of Fig. 5.4.

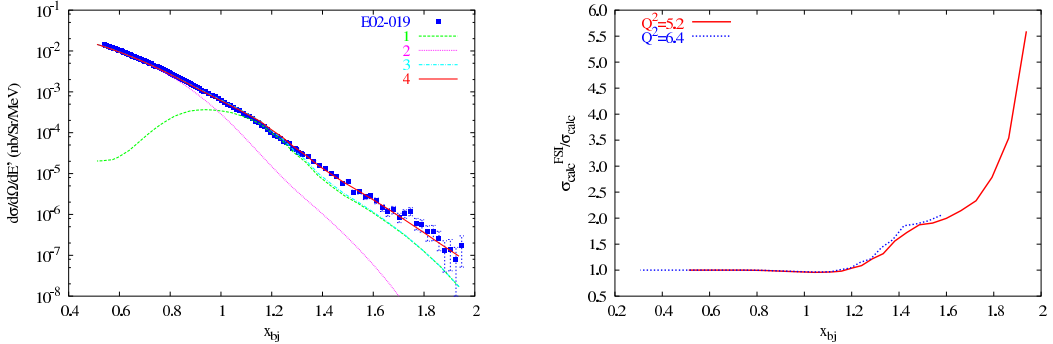


Figure 5.4: Carbon cross section at $\theta_{HMS} = 32^\circ$, data and theory calculation (left). The contributions in the theoretical calculation are as follows: (1) quasielastic, (2) inelastic, (3) sum of (1) and (2), (4) total cross section, including FSIs. Calculation provided by O.Benhar [62]. The right plot shows the relative contribution from FSIs alone for 32° and 40° , obtained by comparing the final folded cross section to the sum of the quasielastic and inelastic pieces. Note that the contribution from FSIs is very similar at these values of Q^2 .

5.2 $F(y,|q|)$ Scaling Function

The scaling function $F(y,|q|)$ was extracted for each target via the method described in Sec. 2.1.1. The inelastic contribution has been subtracted from the measured cross section using the model described in Sec. 4.4.14. Fig. 5.5 shows the region around the quasielastic peak for deuterium and the size of the inelastic contribution can be seen. The inelastic contribution is the largest for the setting with the largest Q^2 , 50° for E02-019, with $\approx 30\%$ of the total strength at the quasielastic peak. Experimental scaling functions are shown in Figs. 5.6-5.8, along with the fit to the data that was used as an input to the cross section model.

PWIA predicts that scaling will be approached from below with increasing Q^2 , as more strength from the spectral function is integrated over. In reality, scaling appears to be approached from above, as is very well seen in deuterium data (Fig. 5.6). This

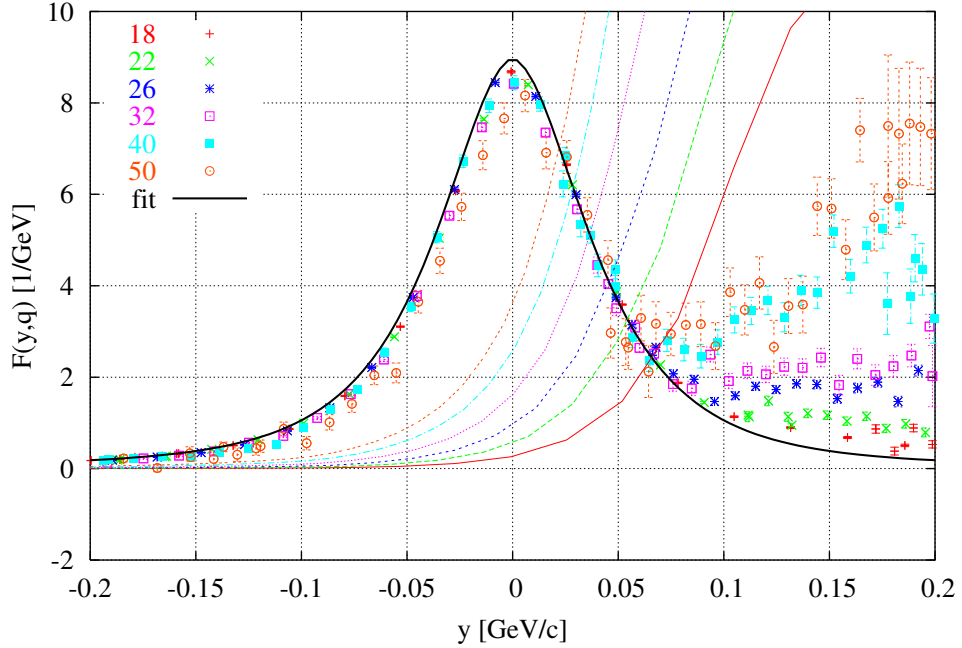


Figure 5.5: Scaling function $F(y, q)$ for deuterium, as extracted from experimental data. The inelastic cross section (solid color lines) was calculated using a model described in Sec. 4.4.14 and subtracted from the experimental cross section. The solid black line is the fit to the experimental scaling function that was then used in the cross section model.

is because much of the strength in the tail comes from FSIs, which are not included in the PWIA, but their contribution is large enough to change the approach to scaling.

This approach can be seen when the scaling function is plotted for fixed values of y , as a function of Q^2 . Once the points lie on a flat line - there's no Q^2 -dependence and the scaling regime is reached. This can be seen in Figs. 5.9 and 5.10 for ^2H and ^{12}C , respectively. Note that in Figs. 5.6-5.8, the inelastic contribution was subtracted before the extraction of $F(y, |\mathbf{q}|)$. That is not the case in Figs. 5.9 and 5.10, where the scaling function is determined using the total measured cross section. This way,

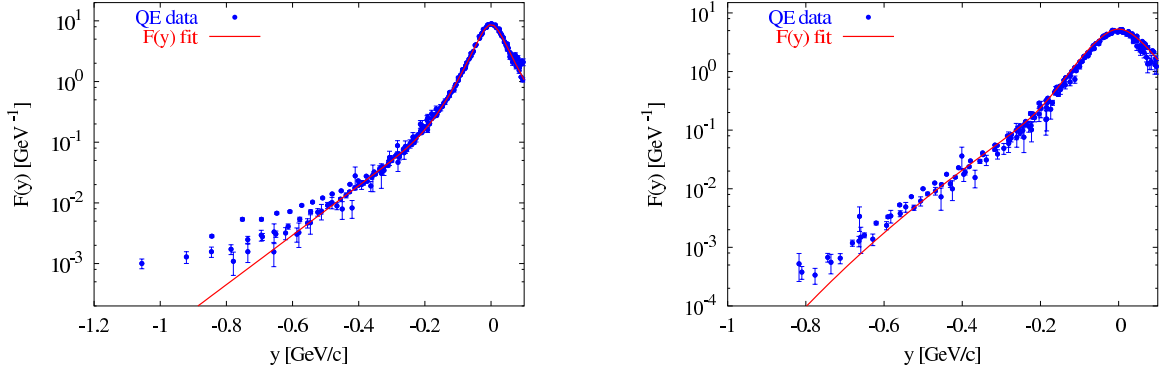


Figure 5.6: ^2H (left) and ^3He (right): experimental scaling function, $F(y, |\mathbf{q}|)$, and the fit to it. The fit was used to calculate the quasielastic contribution to the model cross section. Errors shown are statistical only. For ^2H , the points that lie above the fit correspond to lower Q^2 values, and have the highest contributions from FSIs. The inelastic contribution was subtracted using the cross section model described in Sec. 4.4.14.

the decrease in the inelastic contribution can be seen. In the plots, y values between 200 MeV/c and -700 MeV/c are shown, even though y -scaling is not expected for positive y , as those data correspond to the high energy loss side of the quasielastic peak. The inelastic contribution breaks the scaling for low values of y (positive and negative). As y becomes more negative, the onset of this scale-breaking moves to larger values of Q^2 , where the inelastic contribution is largest. At large negative values of y , the scaling is broken for low values of Q^2 , which are the data with the largest contributions from FSIs. The ^{12}C scaling function is also plotted for constant y values as a function of $1/q$ in Fig. 5.11. In order to determine the asymptotic limit, the inelastic contribution would need to be subtracted and the $1/q^2$ term must be shown to be negligible (i.e. $1/q \ll 1$), which is not the case for all the data points. If one wishes to extract the asymptotic limit of the scaling function, it might be best

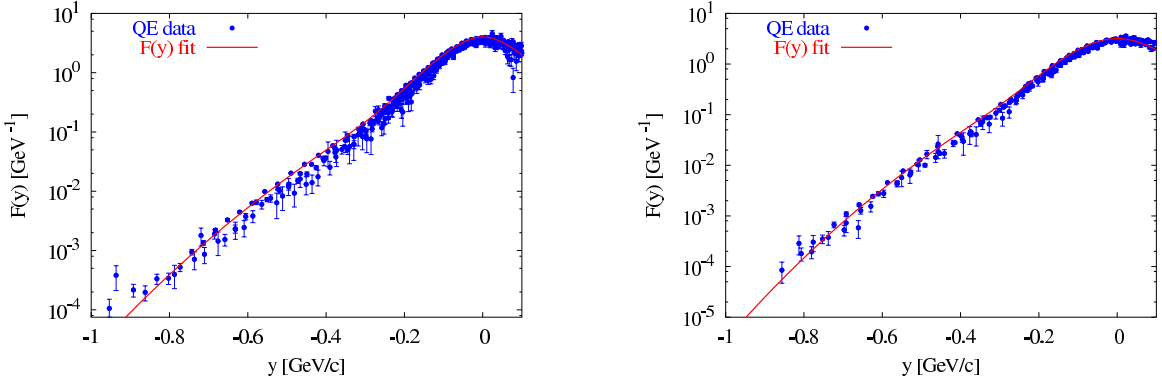


Figure 5.7: ${}^4\text{He}$ (left) and ${}^{12}\text{C}$ (right): experimental scaling function, $F(y, |\mathbf{q}|)$, and the fit to it. The fit was used to calculate the quasielastic contribution to the model cross section. The inelastic contribution was subtracted using the cross section model described in Sec. 4.4.14. Errors shown are statistical only.

to combine this data set with other available data [42].

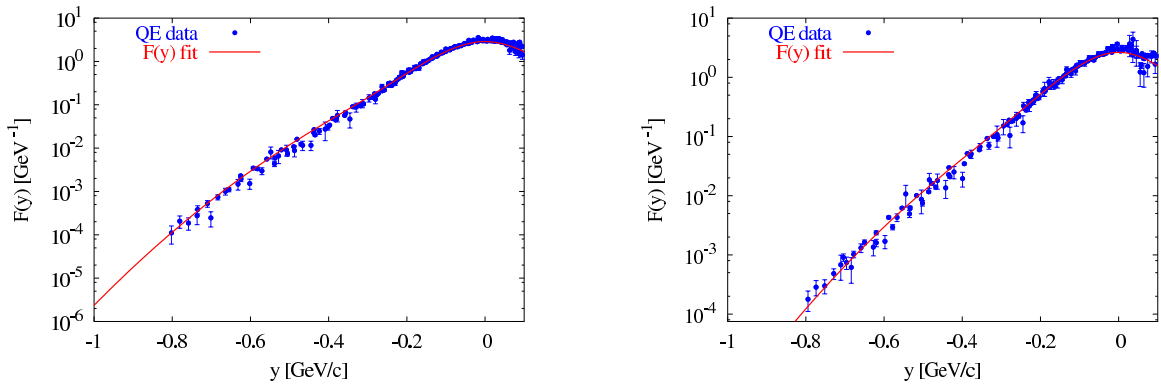


Figure 5.8: ^{63}Cu (left) and ^{197}Au (right): experimental scaling function, $F(y, |\mathbf{q}|)$, and the fit to it. The fit was used to calculate the quasielastic contribution to the model cross section. The inelastic contribution was subtracted using the cross section model described in Sec. 4.4.14. Errors shown are statistical only.

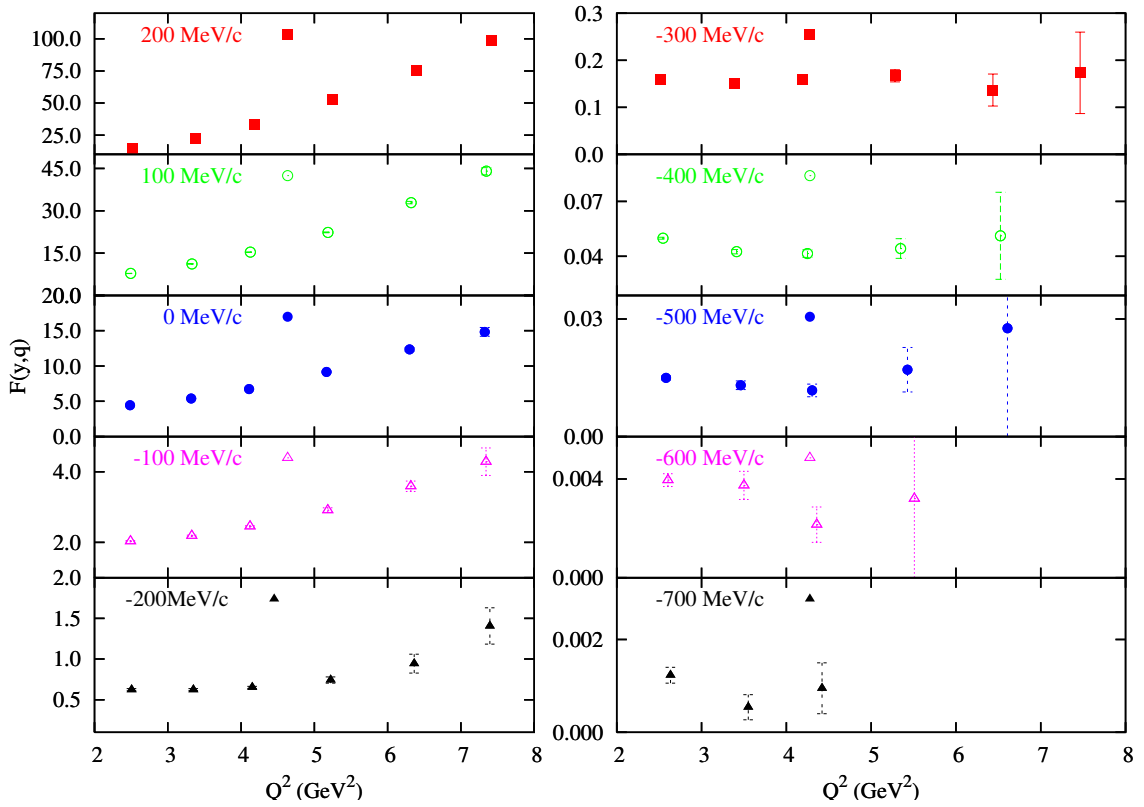


Figure 5.9: ^{12}C scaling function, shown for fixed values of y , as a function of Q^2 . The inelastic contribution has not been subtracted and it is the cause of scaling violations for positive and small negative values of y at high Q^2 . At large negative values of y , scaling is broken at low Q^2 due to contributions from FSIs which decrease with increasing Q^2 .

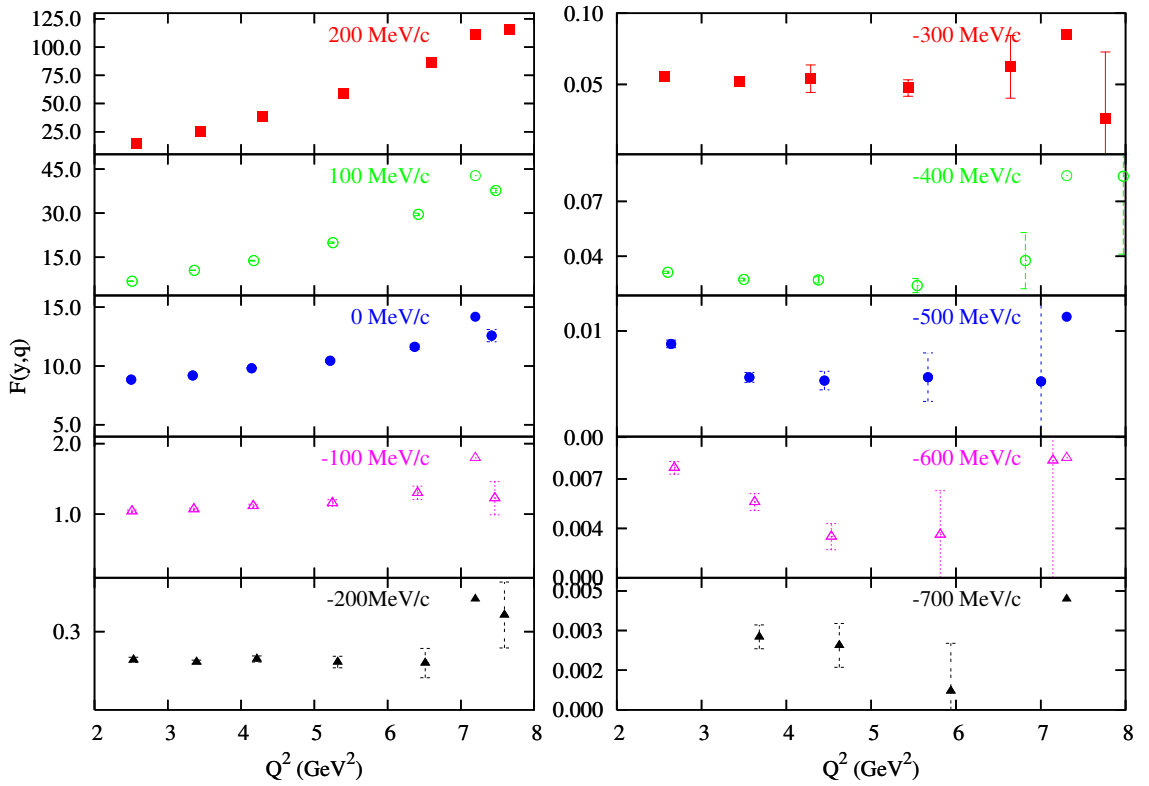


Figure 5.10: ^2H scaling function, shown for fixed values of y , as a function of Q^2 . The inelastic contribution has not been subtracted and it is the cause of scaling violations for positive and small negative values of y at high Q^2 . At large negative values of y , scaling is broken at low Q^2 due to contributions from FSIs which decrease with increasing Q^2 .

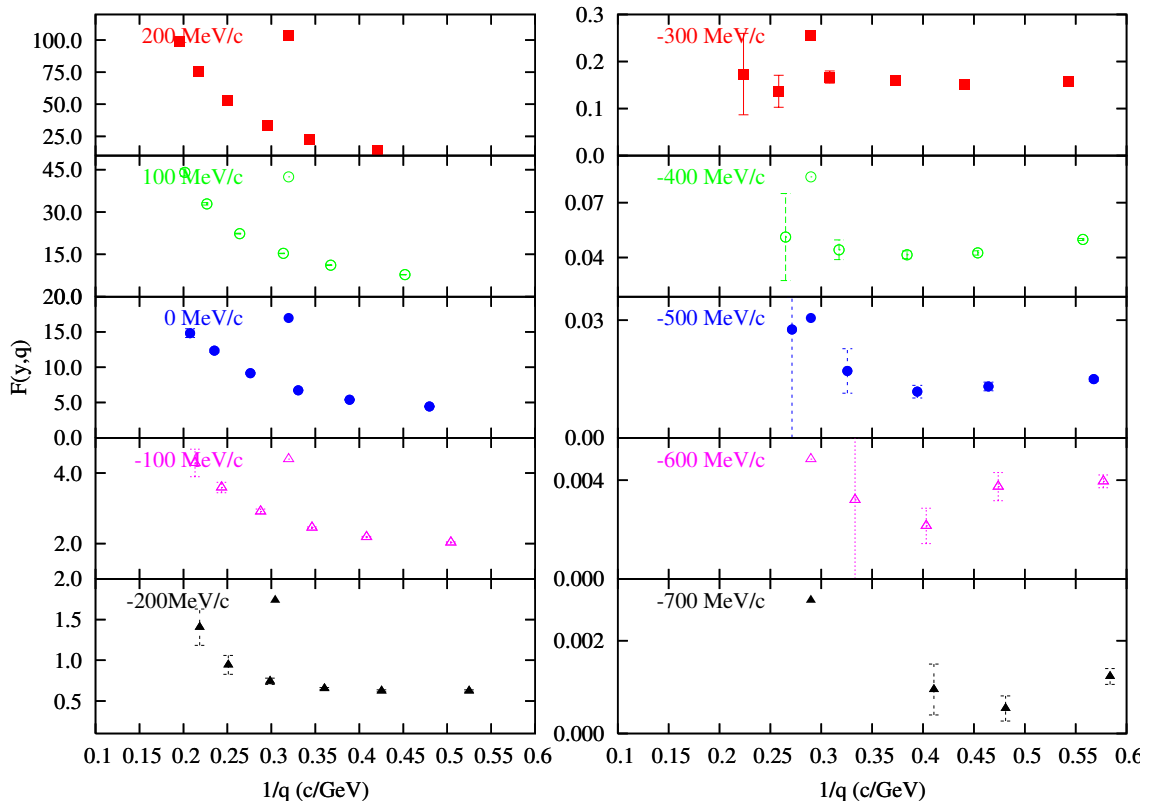


Figure 5.11: ^{12}C scaling function, shown for fixed values of y , as a function of $1/q$. Following the approach of [44] described in Sec. 2.1.1, it may be possible to extract the asymptotic limit of the scaling function, provided that the inelastic contribution is subtracted at $1/q \ll 1$.

5.3 Superscaling

Superscaling function $f(\psi')$ was extracted from the measured cross sections with the method described in [48]. In this reference, the lightest nucleus that was included in the analysis was ^6Li and superscaling was observed for all nuclei studied. For E02-019, the lightest nucleus examined as a function of $f(\psi')$ is ^4He , which was included in the superscaling analysis of [47] and was found to superscale, except in the region of the quasielastic peak. As in the references, Fig. 5.12 shows the superscaling function $f(\psi')$ for the selected targets for all available kinematics. In E02-019 data, we see that

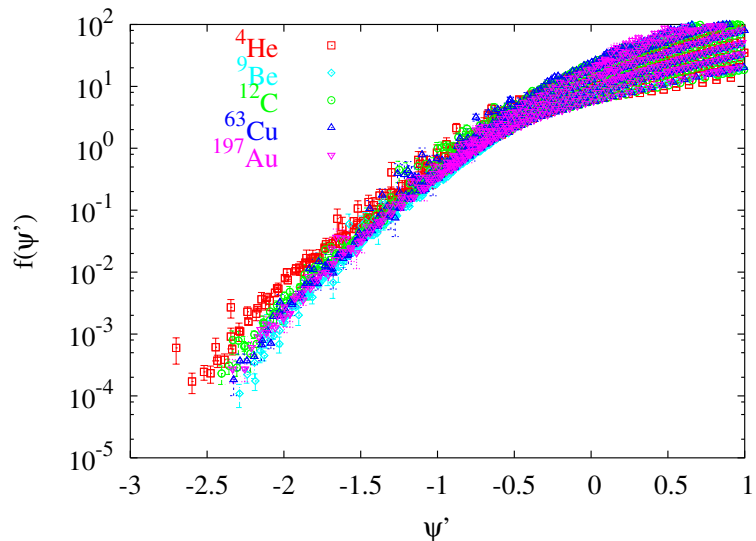


Figure 5.12: Superscaling function $f(\psi')$, extracted from the E02-019 cross sections for all available kinematics, $A>3$.

^4He deviates noticeably from the superscaling curve described by the heavier targets. Deviations around the quasielastic peak can be explained by the ^4He momentum distribution, which has a well-defined peak. However, this explanation doesn't extend

into the quasielastic tail.

When we examine $f(\psi)'$ for just one kinematic setting, the deviation of ${}^4\text{He}$ can be more easily seen. In addition, the heavy targets do not appear to form one scaling curve, especially for large negative values of ψ' . However, when a similar plot is made using the conventional variable, y , and the corresponding scaling function $F(|\mathbf{q}|,y)$, we observe similar behavior (see Figs. 5.13 and 5.14). While superscaling gives better scaling behavior at the peak for low values of Q^2 , as is seen in Fig. 5.13, $F(|\mathbf{q}|,y)$ does a better job for the high momentum tail and for higher Q^2 values (see Fig. 5.14).

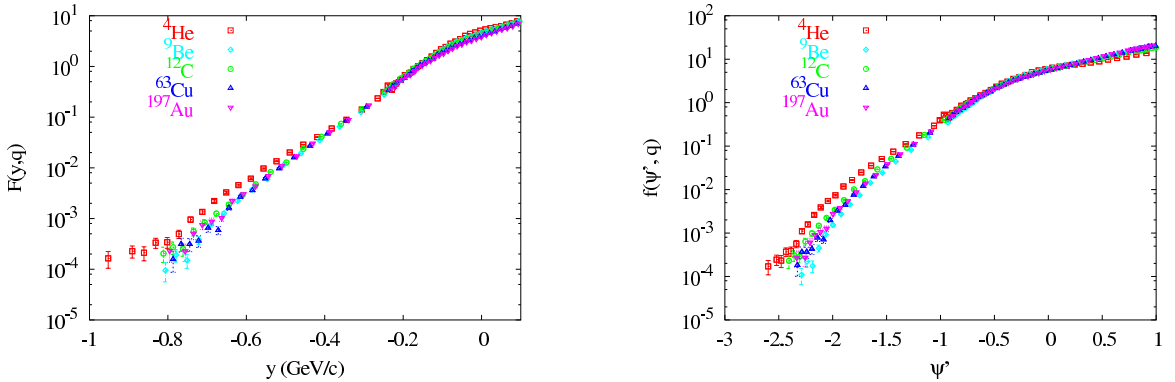


Figure 5.13: $F(|\mathbf{q}|,y)$ and $f(\psi')$, shown for $A>3$, for the central angle setting, 18° .

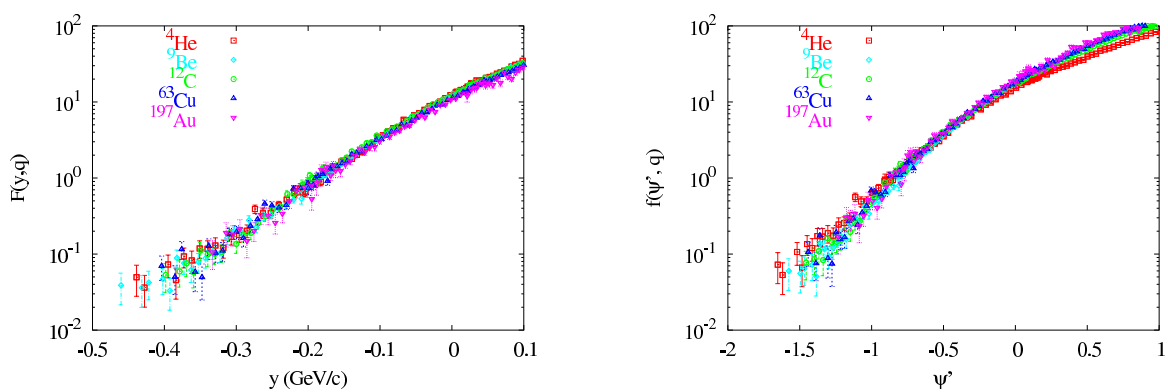


Figure 5.14: $F(|\mathbf{q}|, y)$ and $f(\psi')$, shown for $A > 3$, for the central angle setting, 40° .

5.4 Other Scaling Variables - y_{cw}

The cross section data were also analyzed in terms of the modified scaling variable y_{cw} , described in Sec. 2.1.3. The results of this analysis can be seen in Figs. 5.15 and 5.16, where the reduced cross section, $F(y, |\mathbf{q}|)$ is shown as a function of both y , and y_{cw} . Also plotted are the results of theoretical calculations of momentum distributions, $n(k)$ for several nuclei using Light Front Dynamics and Coherent Density Fluctuation Model [95, 96], converted to $F(y, |\mathbf{q}|)$ through Eq. 2.20. The latter model, CDFM, is a natural extension of the Relativistic Fermi Gas model, that uses the density and momentum distributions to explain the observations of both scaling and superscaling. Both calculations are only available for Carbon, where the LFD curve shows excellent agreement with experimental data examined as a function of y_{cw} . This could suggest that y_{cw} is the appropriate variable for this analysis. However, the current definition needs to be replaced with a relativistic version, since it breaks down for large negative values of momentum, where the quantity under the square root in Eq. 2.30 becomes undefined. For deuterium of course, the two variables are the same.

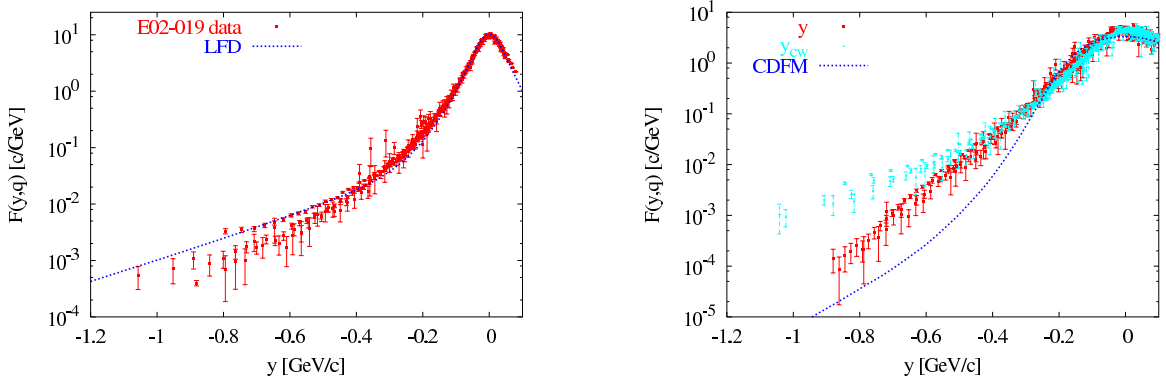


Figure 5.15: Experimental scaling function, $F(y,|\mathbf{q}|)$ for ^2H and ^4He , shown as a function of conventional y , as well as y_{cw} , along with a theoretical calculation by the group using the LFD approach. For ^2H , $y=y_{cw}$. The inelastic contribution has been subtracted from the data.

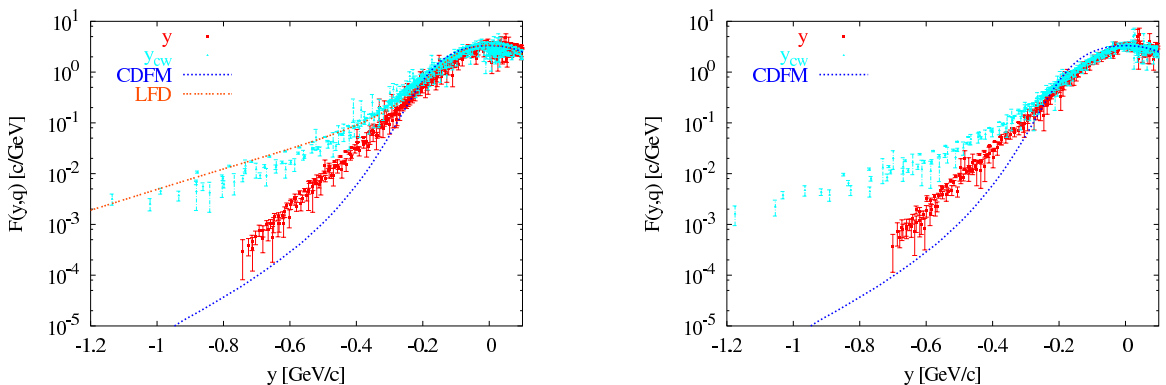


Figure 5.16: Experimental scaling function, $F(y,|\mathbf{q}|)$ for ^{12}C and ^{197}Au , shown as a function of conventional y , as well as y_{cw} , along with a theoretical calculation by the BLANK group using the LFD (^{12}C only) and CDFM approaches. The inelastic contribution has been subtracted from the data. Remarkable agreement is seen for ^{12}C between the LFD calculation and the data analyzed in y_{cw} .

5.5 Short Range Correlations - Ratios

In order to study $2N$ and $3N$ correlations in nuclei, cross section ratios were obtained of nuclei with $A > 3$ to those of ^2H and ^3He . If these ratios show plateaus, they are believed to be a signature of $2N$ or $3N$ correlations, depending on the x -range. At $x > 1$, the electron can scatter from a single nucleon of high momentum, or from a correlated pair or trio of nucleons. Different regions in x are sensitive to these different reactions. For example for $1 < x < 1.4$, the scattering is believed to be from a single moving nucleon, and scattering from a correlated pair takes place for $x \approx 1.4 < x < 2$. Similarly, scattering from a $3N$ correlated cluster is believed to be taking place for $2.5 < x < 3$. Previous measurements [97] of the ratios have shown no evidence of correlations for $Q^2 < 1.4 \text{ GeV}^2$, which has since then been used as the threshold for this kind of scaling. The E02-019 data exceed this threshold.

To estimate the relative probabilities of SRCs in heavier nuclei (A_1) to those in lighter nuclei like ^2H or ^3He (A_2), a ratio of the experimentally measured cross sections, $R(A_1, A_2) = \sigma_{A_1}/\sigma_{A_2}$, is formed and an isoscalar correction [97] is applied to give:

$$r(A_1, A_2) = R(A_1, A_2) \times \frac{A_1(Z_2\sigma_p + N_2\sigma_n)}{A_2(Z_1\sigma_p + N_1\sigma_n)}, \quad (5.2)$$

where σ_n and σ_p are the elastic electron-nucleon cross sections. The isoscalar correction factor shows little Q^2 dependence and varies very slowly with x . For example, the correction factor for the $^{12}\text{C}/^3\text{He}$ ratio varies between ≈ 1.125 at 50° and ≈ 1.138

at 18° at $x=1$.

Fig. 5.17 shows the cross section ratios of ^{12}C and ^{63}Cu to ^2H . The data at 18° have the best coverage and statistics, and show a possible plateau for both targets for $x > 1.4$. The ratios are limited by the deuterium data, which has large contributions for the aluminum container cell that grow with x , reaching 100% at $x \approx 2$. The $2N$ correlation plateau is more clearly seen in the ratios of the same cross sections to ^3He (see Fig. 5.18), where the same end-cap subtraction constraints don't dominate until much larger x values.

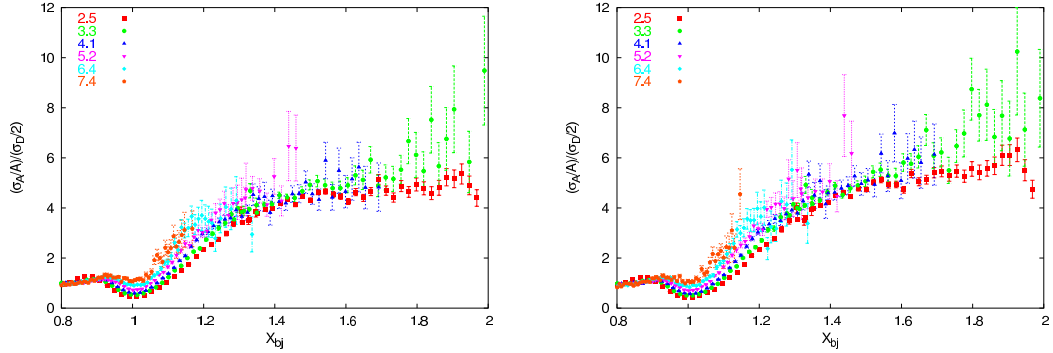


Figure 5.17: Cross section ratios of ^{12}C and ^{63}Cu to ^2H . The expected $2N$ plateau for $x > 1.4$ is not flat, since the ^2H cross sections in that region are limited by the subtraction of the aluminum cell yield, which dominates the cross section. The Q^2 values quoted in the figure are calculated at the quasielastic peak.

It's been suggested that while the ratios are a signature of SRCs, they cannot be used to provide a quantitative measurement since different targets will have different FSIs. However, a more widely accepted idea [63] is that the FSIs in the correlations region are localized to the correlations themselves since they're dominated by the rescattering of the knocked-out nucleon by the correlated nucleon(s). Therefore, the

FSIs do not contribute to the ratios, but rather cancel out.

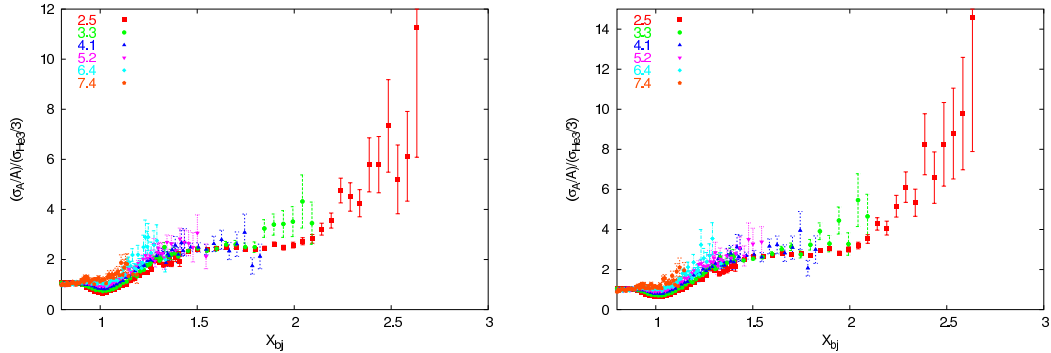


Figure 5.18: Cross section ratios of ^{12}C and ^{63}Cu to ^3He . The expected 2N plateau for $x > 1.4$ is better visible than in the ratios to ^2H . However, the expected plateaus at $x > 2.5$ suffer from poor statistics and the large contribution from the aluminum cell to the helium cross section. The Q^2 values quoted in the figure are calculated at the quasielastic peak.

$3N$ correlations can also be seen in ratios to ^4He , which is less affected by the target cell contribution in the $2.5 < x < 3$ range than ^3He . This ratio is shown in Fig. 5.19 and suggests a plateau in the $x > 2.5$ region, where $3N$ correlations should be visible if present. It appears that the ratios shown in Fig. 5.18 are not independent

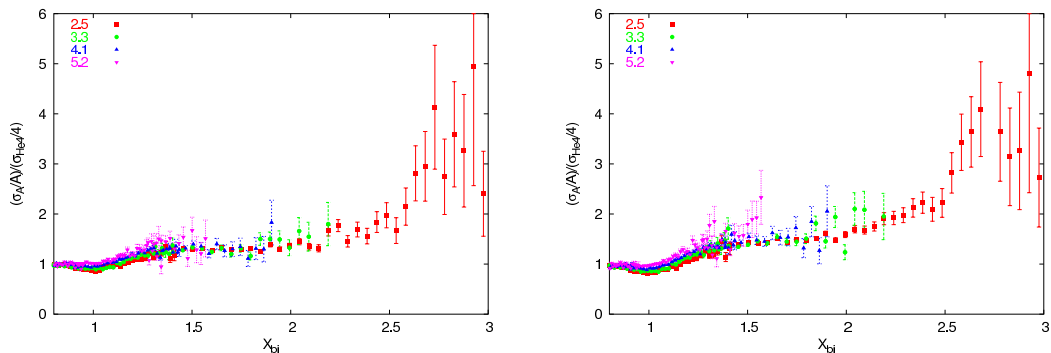


Figure 5.19: Cross section ratios of ^{12}C and ^{63}Cu to ^4He . The $3N$ plateau is seen more clearly in this case than in the ratio to ^3He . The Q^2 values quoted in the figure are calculated at the quasielastic peak.

of Q^2 . Therefore, when $r(A_1, A_2)$ was extracted from the data, it was done separately for each Q^2 setting. Table 5.2 lists the ratios, $r(A_1, A_2)$, of A_1 to ${}^3\text{He}$, in the 2N correlation region ($1.5 < x < 2$) for the three lowest Q^2 settings. For targets in common with [97], the ratios for this experiment are lower. However, the two data sets are consistent if systematic as well as statistical errors are taken into account. The systematic uncertainties listed in Table 5.4 apply to the cross sections, and not all of them are included when ratios are taken since many of the corrections (e.g. detector-related quantities) will cancel. Also, some uncertainties such as those coming from the radiative corrections, have a contribution associated with the method and another contribution that's target-dependent. In such cases, only the target-dependent errors were propagated. For the uncertainty on the end-cap subtraction for ${}^3\text{He}$, a 1% uncertainty was used (3% of the $\approx 35\%$ contribution at $1.5 < x < 2$).

Table 5.2: $r(A_1, {}^3He)$ in the 2N correlation region ($1.5 < x < 2$) for $A > 3$ at each kinematic setting with data in the relevant x region. Q^2 values are quoted at $x=1.5$. Errors quoted are statistical and systematic. See text for discussion of systematic errors.

A_1	$Q^2 = 2.71 \text{ (GeV}^2\text{)}$	$Q^2 = 3.73 \text{ (GeV}^2\text{)}$	$Q^2 = 4.76 \text{ (GeV}^2\text{)}$
${}^4\text{He}$	$1.86 \pm 0.009 \pm 0.073$	$1.89 \pm 0.031 \pm 0.074$	$1.83 \pm 0.079 \pm 0.071$
${}^9\text{Be}$	$2.09 \pm 0.011 \pm 0.071$	$2.06 \pm 0.030 \pm 0.070$	$2.10 \pm 0.086 \pm 0.072$
${}^{12}\text{C}$	$2.42 \pm 0.013 \pm 0.083$	$2.47 \pm 0.038 \pm 0.084$	$2.42 \pm 0.099 \pm 0.083$
${}^{63}\text{Cu}$	$2.70 \pm 0.015 \pm 0.095$	$2.72 \pm 0.041 \pm 0.096$	$2.76 \pm 0.114 \pm 0.097$
${}^{197}\text{Au}$	$2.83 \pm 0.016 \pm 0.111$	$2.81 \pm 0.043 \pm 0.110$	$2.97 \pm 0.122 \pm 0.116$

5.6 Inelastic Response

The inelastic response is best examined by looking at the F_2 structure function. It is extracted from the measured cross section with the method described in Sec. 2.2 and has an additional systematic uncertainty associated with R .

As was discussed in Sec. 1.3.3, scaling of the nuclear structure function has been previously observed in x in the deep inelastic region. Similar behavior is seen in E02-019 results, shown in Figs. 5.20 and 5.21, for low values of x . To examine the Q^2 -dependence of the structure function, it is useful to plot it for constant values of x as is done in Figs. 5.22 and 5.23 for the Helium-4 and Carbon targets. Even at low values x (< 0.65), there is a significant fall-off in F_2 over the Q^2 range of E02-019. Data for $x < 0.45$ are not shown, since data at only two settings of θ_{HMS} reach that kinematic range. Of the low- x data that are shown, only the two highest Q^2 settings

reach the DIS regime ($W^2 > 4$, shown in Fig. 5.24), so it's not surprising that scaling is not observed.

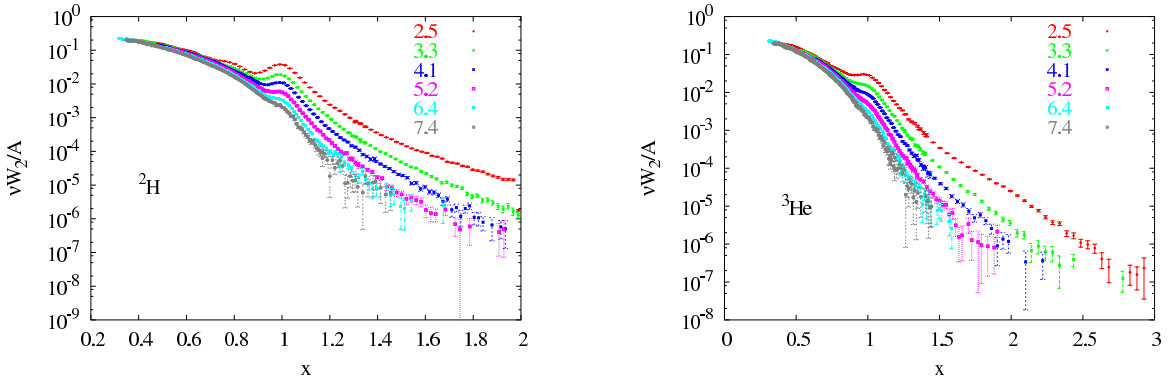


Figure 5.20: F_2 structure function for ^2H (left) and ^3He (right) as a function of x , all HMS angle settings. Scaling is seen for the lowest values of x only.

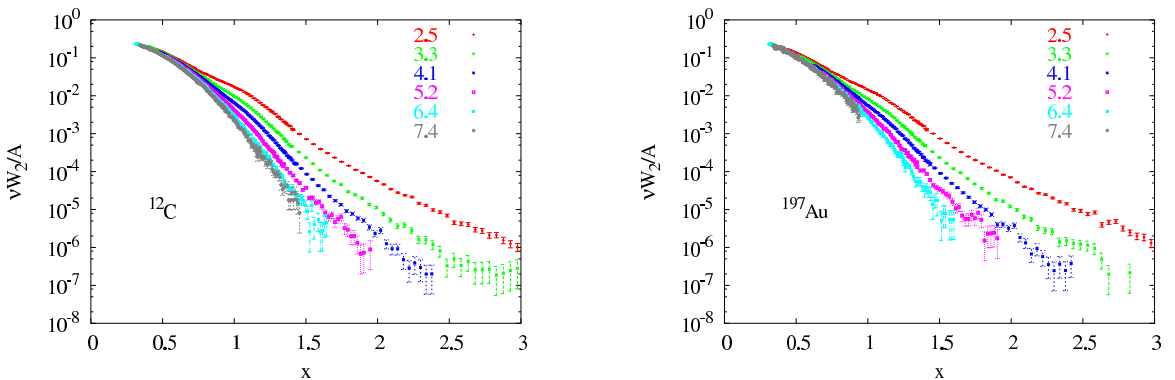


Figure 5.21: F_2 structure function for ^{12}C (left) and ^{197}Au (right) as a function of x , all HMS angle settings. Scaling is seen for the lowest values of x only.

Since scaling is only seen in the data over a small range in x , it is more useful to instead look at F_2 as a function of ξ , which includes first order target mass effects and extends the scaling to lower values of Q^2 . The general scaling behavior for several nuclei can be seen in Figs. 5.25 and 5.26. Scaling violations are obvious for the lighter

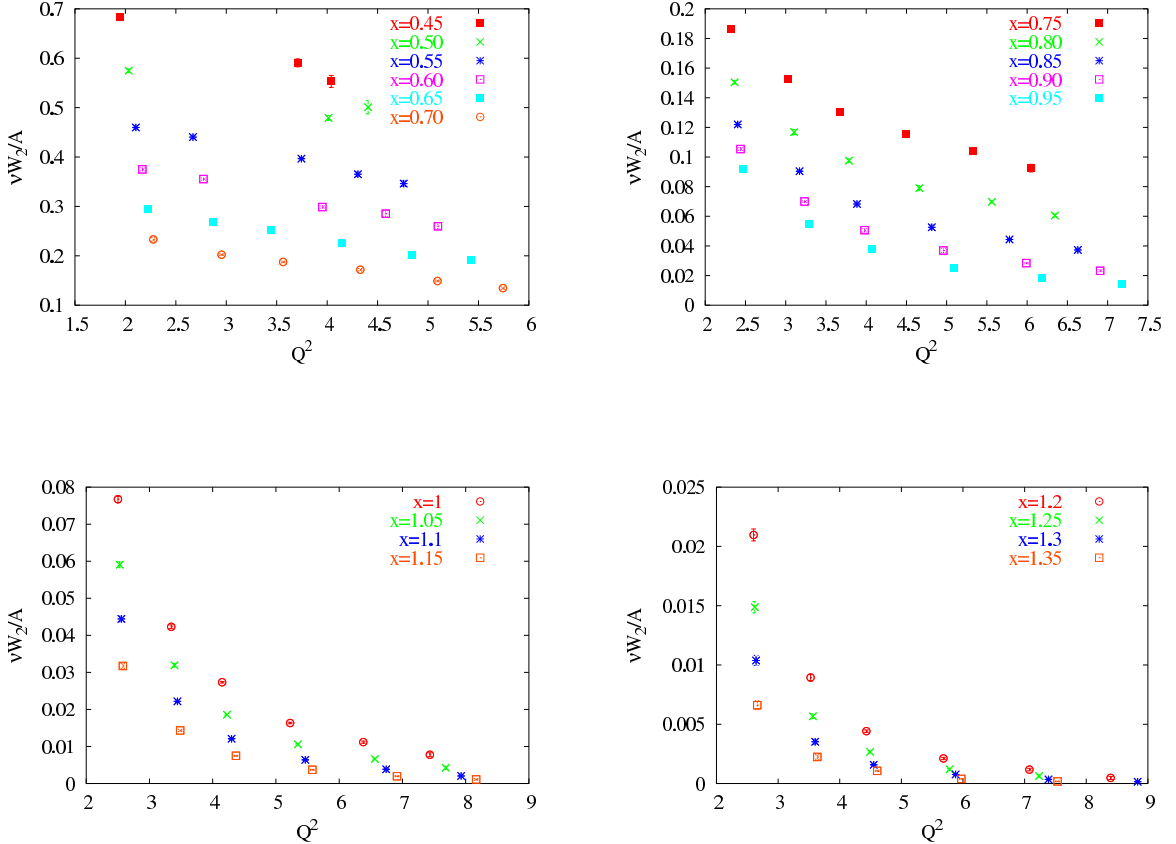


Figure 5.22: F_2 structure function for ${}^4\text{He}$ as a function of Q^2 for fixed values of x . Even at the lowest values of x , the structure function shows a large decrease over the Q^2 range of E02-019.

targets, which have a well defined quasielastic peak appearing at different ξ values for different Q^2 values, rather than at a fixed point, as it does in x . The locations of the quasielastic peak in ξ for each Q^2 are given in Table 5.3. The scaling is best for lowest and highest values of ξ , with scaling violations around the quasielastic peak. The approach to scaling as a function of Q^2 is examined for constant values of ξ for Helium-4 in Fig. 5.27 and Carbon in Fig. 5.28. F_2 falls off less with increasing Q^2 for fixed ξ as compared to fixed x values. The most significant scaling violations are at low

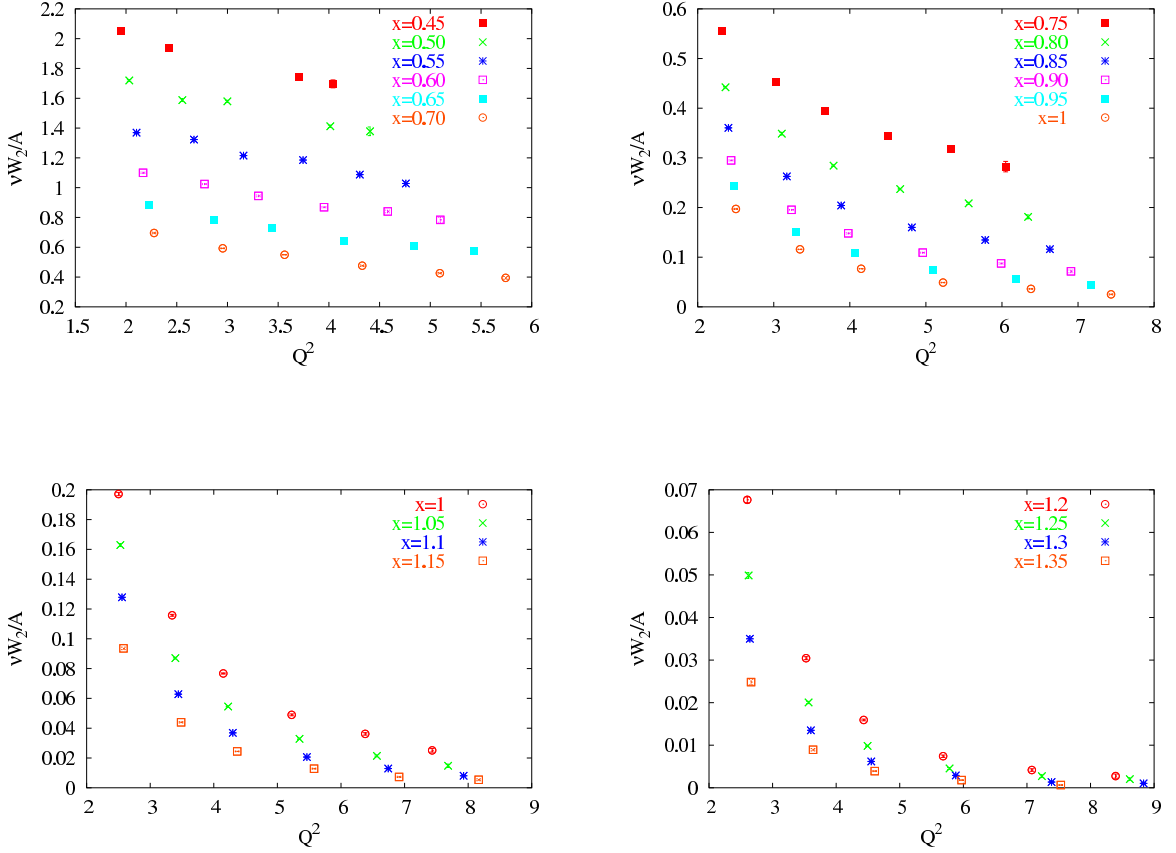


Figure 5.23: F_2 structure function for ^{12}C as a function of Q^2 for fixed values of x . No scaling is observed in x . The scaling that was seen for low values of x in Fig. 5.21, is for the data at the two largest angles (40° and 50°) where the coverage extends below $x < 0.4$ into the DIS region where scaling is expected.

Q^2 values around the quasielastic peak, and decrease quickly with higher momentum transfers. These violations are much smaller in heavier nuclei whose broader peak in $n(k)$ averages over a wider range in ξ in what is referred to as local duality.

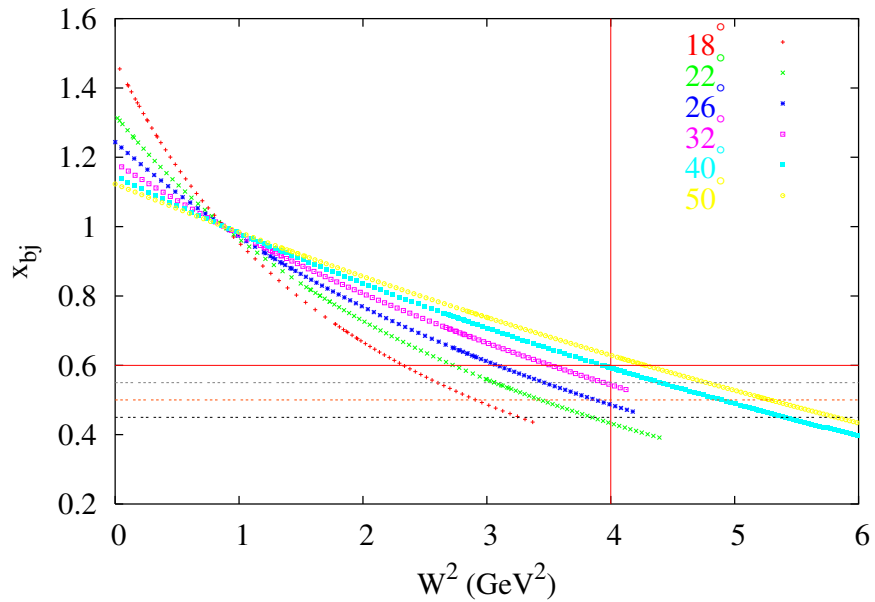


Figure 5.24: Kinematic coverage in x and W^2 . Note that the DIS regime ($W^2 > 4$) only has data at two θ_{HMS} settings over a large range in x .

Table 5.3: Location of the quasielastic peak in ξ ($x=1$) for the θ_{HMS} settings of E02-019 and the corresponding Q^2 values.

θ_{HMS}	Q^2 (GeV 2)	ξ ($x=1$)
18	2.5	0.784
22	3.3	0.82
26	4.1	0.846
32	5.2	0.871
40	6.4	0.891
50	7.4	0.903

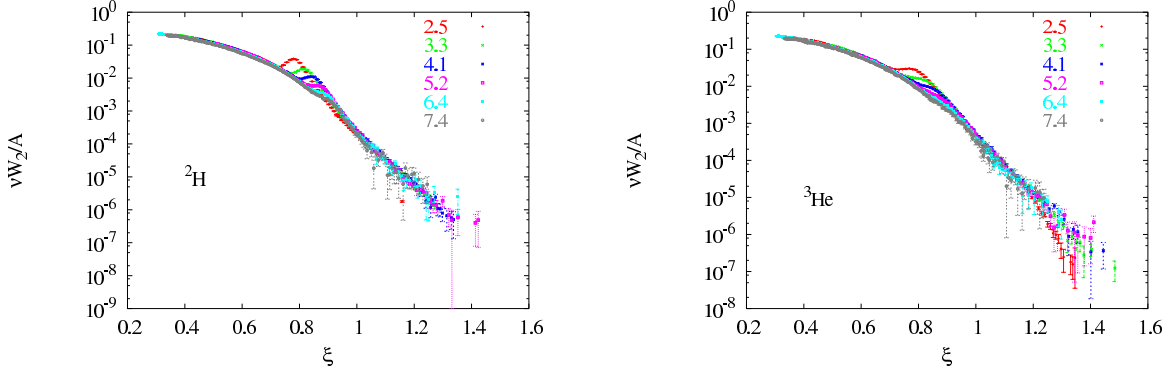


Figure 5.25: F_2 structure function for ^2H (left) and ^3He (right) as a function of ξ , all HMS angle settings. The largest scaling violations are seen around the quasielastic peak, which is very well defined in these light targets.

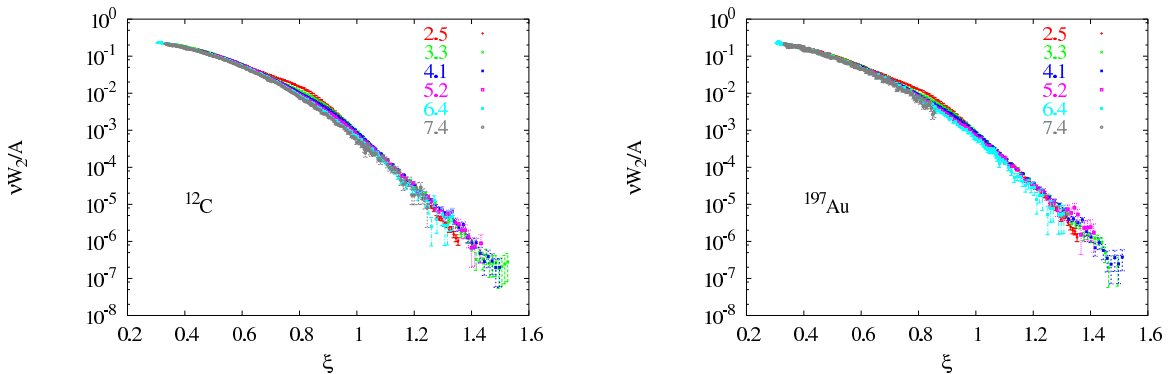


Figure 5.26: F_2 structure function for ^{12}C (left) and ^{197}Au (right) as a function of ξ , all HMS angle settings. While the quasielastic peak is not as well defined in the heavier targets as it is in the light ones, scaling violations are still seen around the peak.

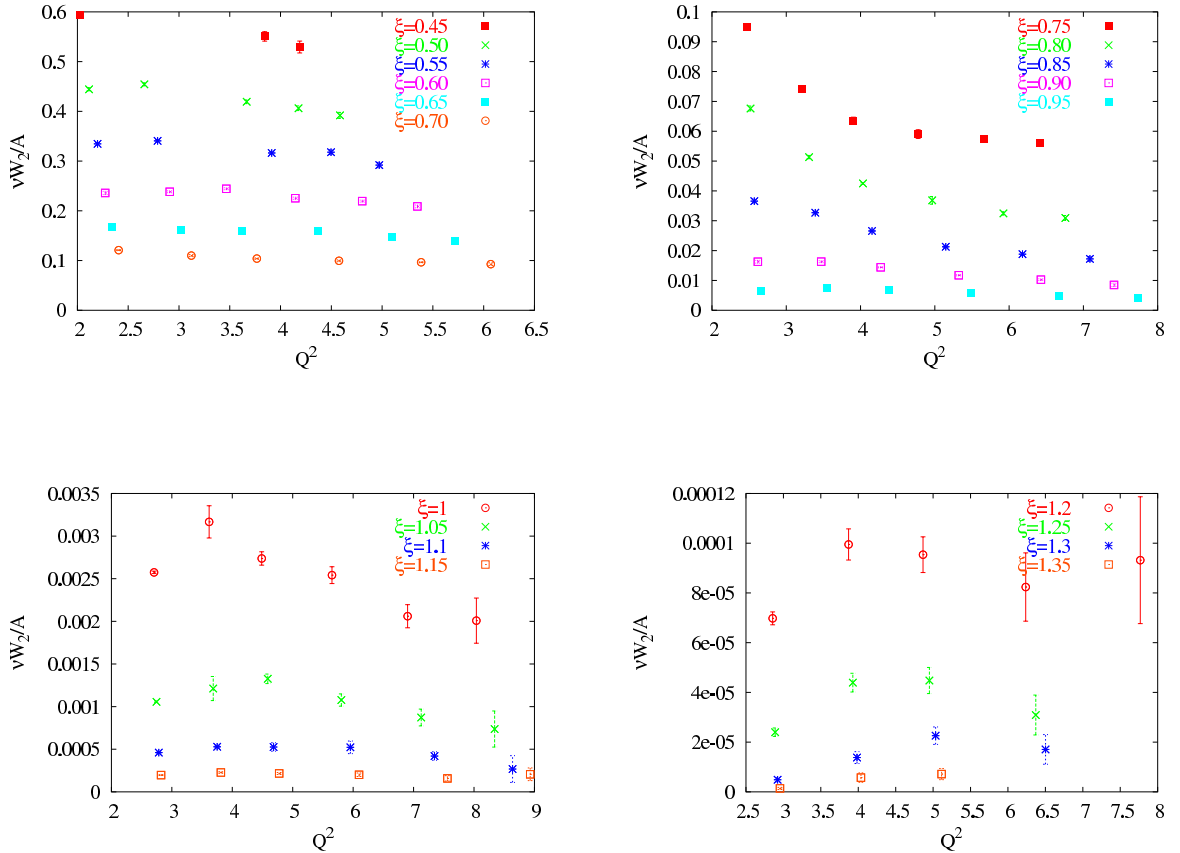


Figure 5.27: F_2 structure function for ${}^4\text{He}$ as a function of Q^2 for fixed values of ξ . Scaling behavior is best for low ξ , but scaling extends into the quasielastic region, with some violations at low Q^2 values.

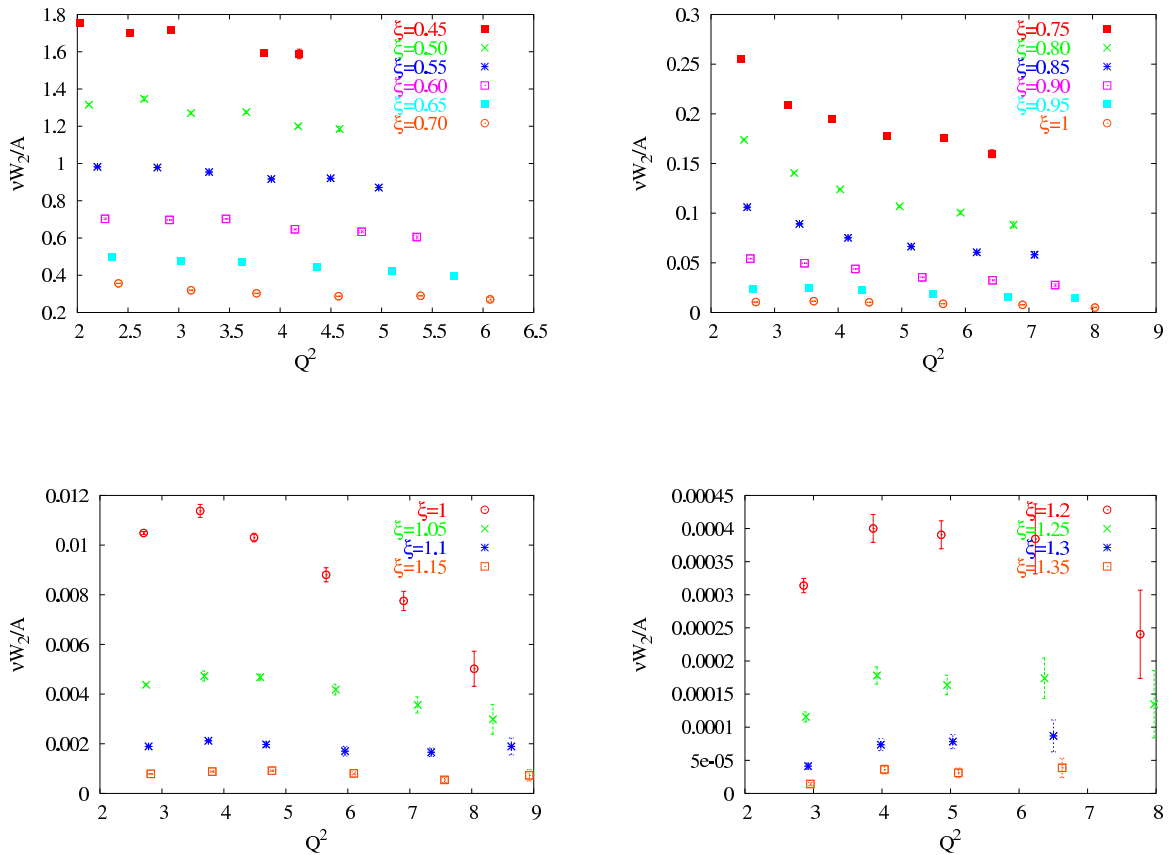


Figure 5.28: F_2 structure function for ^{12}C as a function of Q^2 for fixed values of ξ . Scaling behavior is best for low ξ , but scaling extends into the quasielastic region, with some violations at low Q^2 values.

5.7 A-dependence of F_2

In Sec. 5.6, the F_2 structure function was seen to scale reasonably well for most nuclei over the entire range of ξ with the possible exception of the region around the quasielastic peak. From studies of the EMC effect, we know that the structure function is modified in the nuclear medium, and the size of the effect is similar for different nuclei. This means, that if we plot the structure function vs ξ for a variety of nuclei at a given Q^2 , we expect scaling for the high energy loss side of the quasielastic peak. Fig. 5.29 shows that this is indeed what happens. Scaling in ξ extends into the quasielastic regime as well. This is interesting because different reaction mechanisms are at work in different kinematic ranges, but they all conspire to yield scaling of the F_2 structure function in ξ for all nuclei at a common Q^2 .

Fig. 5.29 shows that there's some target-dependence for low Q^2 values around the quasielastic peak, which is to be expected, since the light nuclei have different momentum distributions from those of heavy nuclei. There's also some target-dependence in the high momentum tail, presumably from different FSIs, but this goes away with increasing Q^2 , supporting O.Benhar's idea that FSIs become Q^2 -independent, and it would seem also target-independent.

The F_2 structure function can also be examined for a given angle setting and a fixed ξ as a function of atomic number A , which is done in Fig. 5.30 for 18° and 22° . This figure clearly shows the deviation of light nuclei from the scaling curve in the quasielastic regime and excellent scaling for low values of ξ , corresponding to the high

energy loss side of the quasielastic peak.

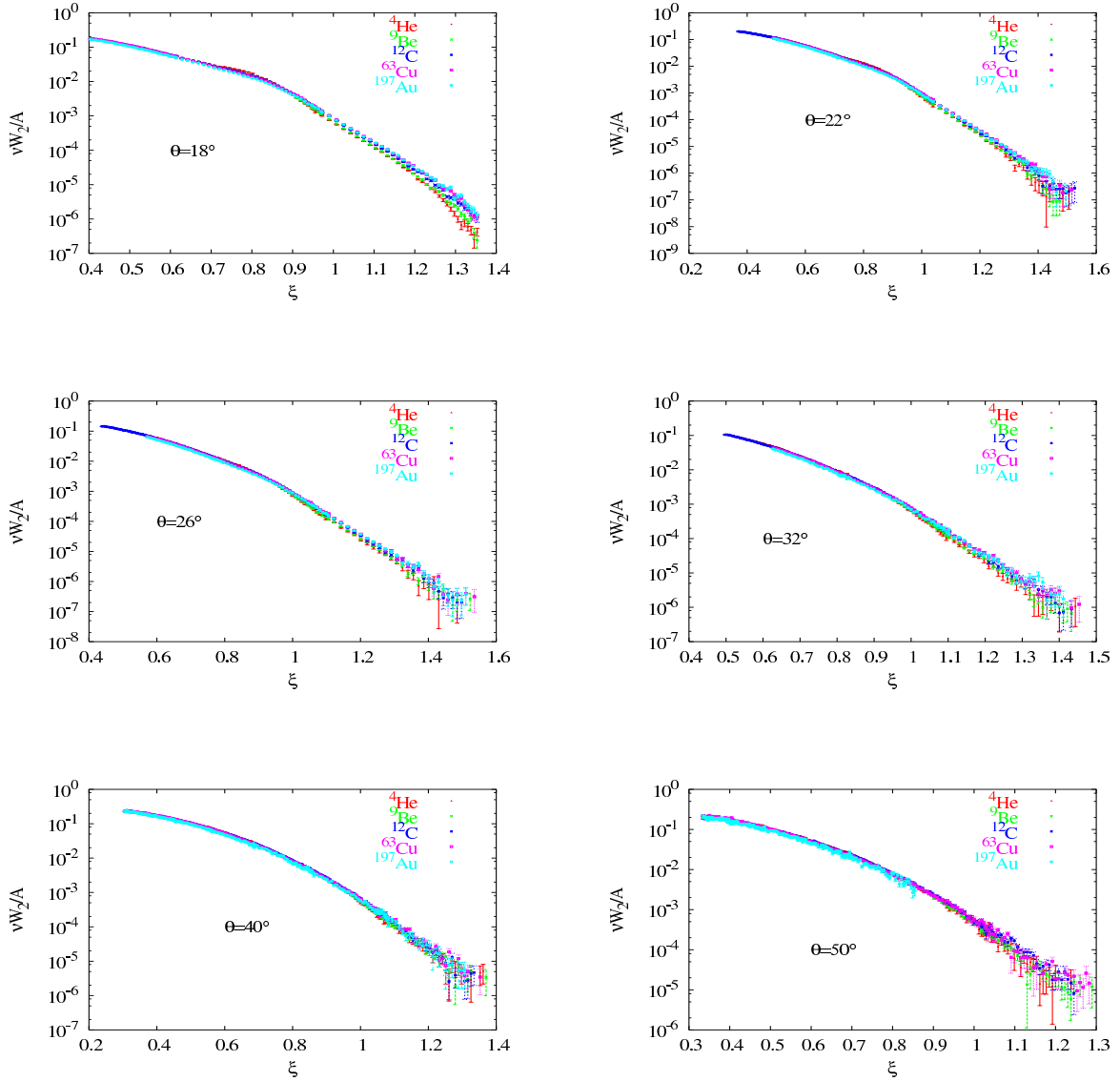


Figure 5.29: F_2 structure function for $A > 3$ as a function of ξ for all kinematic settings. While there's some target-dependence in the structure function at very high ξ for the low angles (low Q^2), it is confined to light nuclei, and it goes away at larger angles (higher Q^2).

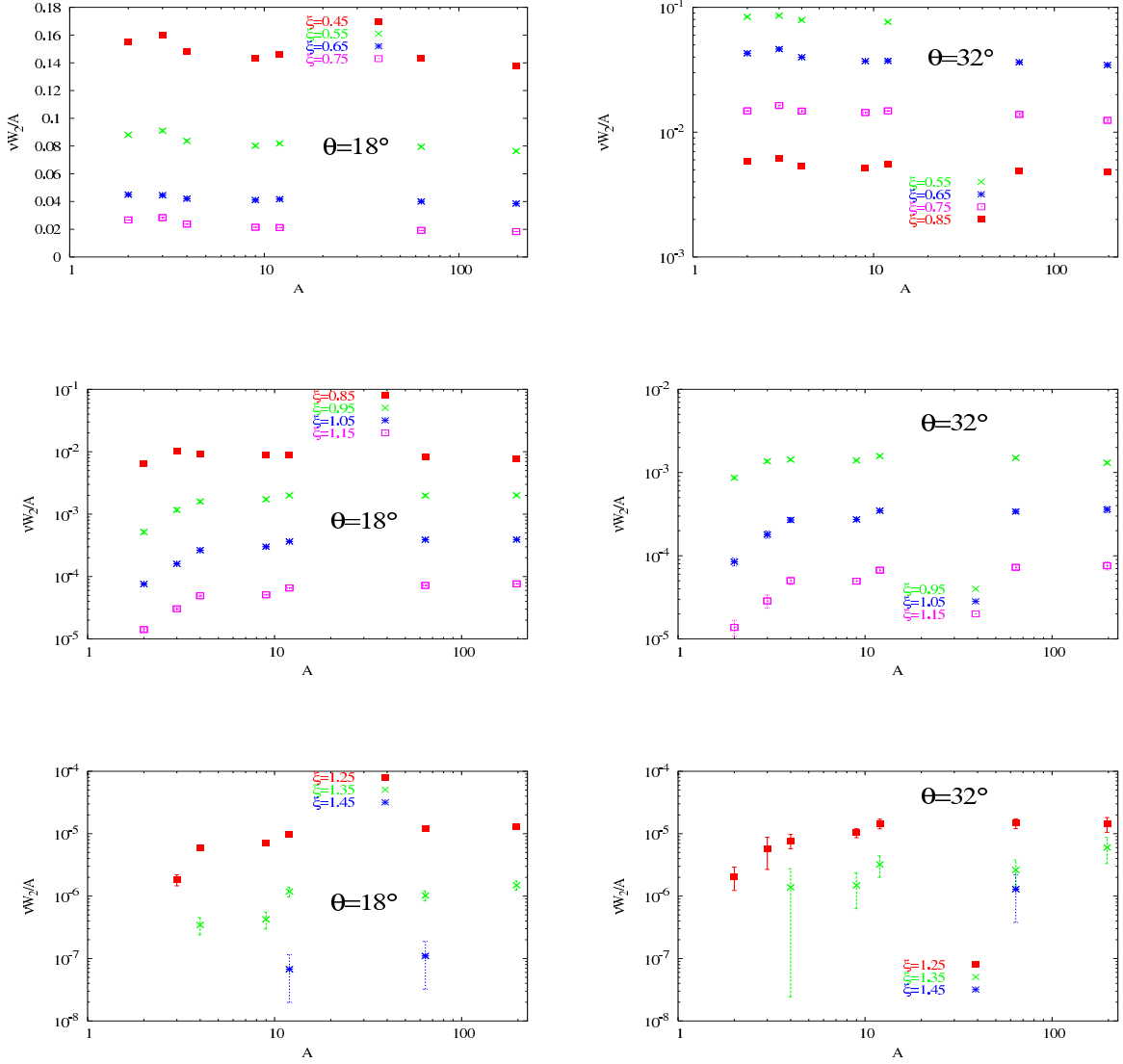


Figure 5.30: F_2 structure function as a function of A for fixed values of ξ at 18° (left) and 32° (right). Note that there is little A -dependence for the lowest values of ξ for all nuclei and the observed A -dependence at higher values of ξ occurs for light nuclei only.

5.8 Systematic Uncertainties

The extracted cross sections were corrected for many effects, such as the detector efficiencies, target densities, and radiative effects. Table 5.4 lists the systematic uncertainties associated with each of the corrections. Those that quote a range in uncertainty, such as the uncertainty due to the subtraction of the charge symmetric background, varied with kinematics and were either parametrized or calculated at each data point using the cross section model.

5.8.1 Kinematic Uncertainties

The uncertainties in the measured kinematic quantities (beam energy, HMS momentum, and HMS angle) are determined based on the reproducibility of those quantities. These uncertainties do not enter into the cross section measurement as directly as, for example, a detector efficiency. Instead, the effect varies with kinematics. The point-to-point uncertainties were determined by evaluating the cross section model at shifted kinematics. The shifts were 0.02%, 0.01%, and 0.2mr for beam, HMS momentum, and HMS angle, respectively. The effect of these shifts on the model cross section gives the size of the point-to-point uncertainty in the measured cross section.

The scale uncertainty was similarly determined. Here, the fact that the HMS momentum is coupled to the beam energy was taken into effect as a correlation between the two uncertainties. This time, both the energy and momentum inputs into the cross section model were scaled at the same time, by 0.05% and 0.03%,

respectively. For the scale uncertainty on the angle, a shift of 0.5mr was applied to the model.

Table 5.4: Systematic Uncertainties. They are discussed in detail in the sections indicated. When a range is quoted on the scale uncertainties, it is to reflect the target-dependence of the quantity. The (*) next to the uncertainties in the kinematic quantities denotes the maximum effect from the uncertainty at the most extreme kinematics, rather than the typical uncertainty. The range of the total uncertainties is a result of combining the individual uncertainties in quadrature for best and worst case scenarios.

Source	Scale	Relative	$\Delta\sigma/\sigma$	Details
Trigger Efficiency	-	0.1%	0.1%	Sec. 4.4.5
Tracking Efficiency	0.4%	0.3%	0.5%	Sec. 4.4.6
Pion Contamination	-	0.2%	0.2%	Sec. 4.3.2
Computer Dead Time	0.1%	-	0.1%	Sec. 4.4.4
Calorimeter Efficiency	-	-	-	Sec. 4.4.7
Positron Subtraction	-	0-2%	0-2%	Sec. 4.3.1
Čerenkov Efficiency	0.05	0.3%	0.3%	Sec. 4.4.7
Acceptance Correction	1%	1%	1.4%	Sec. 4.4.9
Charge	0.4%	0.3%	0.5%	Sec. 3.3.3
Target Thickness	0.5-2.4%	-	0.5-2.4%	Secs. 3.4 && 3.4.1
Bin-Centering	-	0.5%	0.5%	Sec. 4.4.10
Radiative Correction	1%	1%	1.4%	Sec. 4.4.11
Coulomb Correction	-	0-2%	0-2%	Sec. 4.4.13
HMS Momentum	0.05%	0.01%	<5%*	Sec. 5.8.1
Beam Energy	0.05%	0.02%	<5%*	Sec. 5.8.1
HMS angle	0.5mr	0.2mr	<6%*	Sec. 5.8.1
Cryo targets only				
Target Boiling	0.45%	0.2%	0.5%	Sec. 4.3.4
Dummy Subtraction	<0.6%	0-1.8%	0.3-2.4%	Sec. 4.3.3
Total	$\approx 1.7\%$	$\approx 2.4\%$	2.4-6.5%	

Chapter 6

Conclusion and Outlook

The results from E02-019 support previous observations and extend their kinematic range. Cross sections were measured for ^2H , ^3He , ^4He , ^9Be , ^{12}C , ^{63}Cu , and ^{197}Au and were compared to calculations, whenever possible. It appears that current theoretical calculations [36] describe the inclusive data very well, including contributions from FSIs and SRCs.

The scaling function $F(|\mathbf{q}|, y)$ was extracted for all nuclei. Scaling was observed for $y < 0$, approached from above, with violations at low Q^2 due to contributions from FSIs. Momenta as high as $-1.2 \text{ GeV}/c$ were observed. It can be argued that the y_{cw} scaling variable is more appropriate for this analysis, but a relativistic definition is needed given the wide kinematic coverage of the data.

The nuclear inelastic structure function F_2 was extracted for all nuclei. No scaling was observed in x , since most data settings do not probe the kinematic regime where

DIS is dominant. However, F_2 shows excellent scaling in ξ for most nuclei. In addition, scaling of F_2 was observed for different nuclei at the same kinematics for the first time, with some violations for light nuclei at low Q^2 .

Cross section ratios of heavy nuclei to light ones were taken in order to study 2N- and 3N- correlations. Further work needs to be done before the ratios in the $x > 2.5$ region can be quoted with confidence. The contribution from the end-caps of the cryogenic target is very large and a careful study of possible sources of errors is underway.

A follow-up experiment, E12-06-105 [98], has been approved to run at Jefferson Lab after the 12 GeV upgrade. This measurement will extend to the coverage to higher values of Q^2 , into a region where the DIS contribution to the cross sections at $x > 1$ is significant.

Bibliography

- [1] E. J. Finn and M. Alonso, *Physics* (Addison-Wesley Publishing Company Inc, 1992).
- [2] A. O. Hanson, L. H. Lanzl, E. M. Lyman, and M. B. Scott, “Measurement of Multiple Scattering of 15.7-MeV Electrons,” *Phys. Rev.* **84**, 634 (Nov 1951).
- [3] D. B. Day, J. S. McCarthy, T. W. Donnelly, and I. Sick, “Scaling in inclusive electron - nucleus scattering,” *Ann. Rev. Nucl. Part. Sci.* **40**, 357 (1990).
- [4] B. Frois and C. N. Papanicolas, “Electron Scattering and Nuclear Structure,” *Annual Review of Nuclear and Particle Science* **37**, 133 (1987).
- [5] S. Galster *et al.*, “Elastic electron - deuteron scattering and the electric neutron form-factor at four momentum transfers $5\text{-fm}^{-2} < q^2 < 14\text{-fm}^{-2}$,” *Nucl. Phys.* **B32**, 221 (1971).
- [6] C. F. Perdrisat, V. Punjabi, and M. Vanderhaeghen, “Nucleon electromagnetic form factors,” *Prog. Part. Nucl. Phys.* **59**, 694 (2007).

- [7] P. A. M. Guichon and M. Vanderhaeghen, “How to reconcile the Rosenbluth and the polarization transfer method in the measurement of the proton form factors,” Phys. Rev. Lett. **91**, 142303 (2003).
- [8] P. G. Blunden, W. Melnitchouk, and J. A. Tjon, “Two-photon exchange and elastic electron proton scattering,” Phys. Rev. Lett. **91**, 142304 (2003).
- [9] M. K. Jones *et al.*, “ G_E^p/G_M^p ratio by polarization transfer in $\vec{e} p \rightarrow e \vec{p}$,” Phys. Rev. Lett. **84**, 1398 (2000).
- [10] O. Gayou *et al.*, “Measurement of G_E^p/G_M^p in $\vec{e} p \rightarrow e \vec{p}$ to $Q^2 = 5.6 \text{ GeV}^2$,” Phys. Rev. Lett. **88**, 092301 (2002).
- [11] R. C. Walker *et al.*, “Measurements of the proton elastic form-factors for $1 \text{ GeV}/c^2 \leq Q^2 \leq 3 \text{ GeV}/c^2$ at SLAC,” Phys. Rev. **D49**, 5671 (1994).
- [12] L. Andivahis *et al.*, “Measurements of the electric and magnetic form-factors of the proton from $Q^2 = 1.75 \text{ GeV}/c^2$ to $8.83 \text{ GeV}/c^2$,” Phys. Rev. **D50**, 5491 (1994).
- [13] J. Arrington, “How well do we know the electromagnetic form factors of the proton?” Phys. Rev. **C68**, 034325 (2003).
- [14] R. P. Feynman, “Very high-energy collisions of hadrons,” Phys. Rev. Lett. **23**, 1415 (1969).
- [15] W. Yao *et al.*, “Review of Particle Physics,” Journal of Physics G **33**, 1+ (2006).

- [16] J. D. Bjorken and E. A. Paschos, “Inelastic electron-proton and γ -proton scattering, and the structure of the nucleon,” Phys. Rev. **185**, 1975 (1969).
- [17] J. I. Friedman *et al.*, “Behavior of the electromagnetic inelastic structure functions of the proton,” Phys. Rev. D **5**, 528 (1971).
- [18] C. G. Callan and D. J. Gross, “High-Energy Electroproduction and the Constitution of the Electric Current,” Phys. Rev. Lett. **22**, 156 (1969).
- [19] F. Foster and G. Hughes, “Electroproduction of Nucleon Resonances,” Rept. Prog. Phys. **46**, 1445 (1983).
- [20] L. W. Whitlow, S. Rock, A. Bodek, E. M. Riordan, and S. Dasu, “A Precise extraction of $R = \sigma_L/\sigma_T$ from a global analysis of the SLAC deep inelastic e-p and e-d scattering cross-sections,” Phys. Lett. **B250**, 193 (1990).
- [21] Y. Liang *et al.*, “Measurement of $R = \sigma_L/\sigma_T$ and the separated longitudinal and transverse structure functions in the nucleon resonance region,” (2004), nucl-ex/0410027.
- [22] C. E. Carlson and J. L. Poor, “Distribution Amplitudes and Electroproduction of the delta and other low lying Resonances,” Phys. Rev. **D38**, 2758 (1988).
- [23] P. Stoler, “Form-factors of excited baryons at high Q^2 and the transition to perturbative QCD,” Phys. Rev. Lett. **66**, 1003 (1991).

- [24] E. D. Bloom and F. J. Gilman, “Scaling, duality, and the behavior of resonances in inelastic electron-proton scattering,” *Phys. Rev. Lett.* **25**, 1140 (1970).
- [25] E. D. Bloom *et al.*, “High-Energy Inelastic e p Scattering at 6-Degrees and 10-Degrees,” *Phys. Rev. Lett.* **23**, 930 (1969).
- [26] J. Ashman *et al.*, “Measurement of the Ratios of Deep Inelastic Muon - Nucleus Cross-Sections on Various Nuclei Compared to Deuterium,” *Phys. Lett.* **B202**, 603 (1988).
- [27] F. E. Close and R. G. Roberts, “A-dependence of shadowing and the small x EMC data,” *Phys. Lett.* **B213**, 91 (1988).
- [28] E. L. Berger and F. Coester, “Nuclear Effects in Deep Inelastic Lepton Scattering,” *Ann. Rev. Nucl. Part. Sci.* **37**, 463 (1987).
- [29] J. Arrington, “A Precise Measurement of the Nuclear Dependence of Structure Functions in Light Nuclei,” (2003), Jefferson Lab Proposal/E03-103.
- [30] O. Benhar, D. Day, and I. Sick, “Inclusive quasi-elastic electron-nucleus scattering,” (2006), nucl-ex/0603029.
- [31] J. Mougey, “Momentum and Energy distributions from (e, e', p) reactions (talk),” (1979), in Mainz 1979, *Proceedings, Nuclear Physics With Electromagnetic Interactions*, 124-137.

- [32] M. Leuschner, J. R. Calarco, F. W. Hersman, E. Jans, G. J. Kramer, L. Lapikás, G. van der Steenhoven, P. K. A. de Witt Huberts, H. P. Blok, N. Kalantar-Nayestanaki, and J. Friedrich, “Quasielastic proton knockout from ^{16}O ,” Phys. Rev. C **49**, 955 (Feb 1994).
- [33] J. Arrington, *Inclusive Electron Scattering From Nuclei at $x > 1$ and High Q^2* , Ph.D. thesis, California Institute of Technology (1998).
- [34] B. W. Filippone *et al.*, “Nuclear structure functions at $x > 1$,” Phys. Rev. C **45**, 1582 (1992).
- [35] T. De Forest, “Nuclear Emission in Electron Scattering,” Ann. of Physics **45**, 365 (1967).
- [36] O. Benhar, “Final state interactions in the electroweak nuclear response,” Nucl. Phys. Proc. Suppl. **159**, 168 (2006).
- [37] O. Benhar and V. R. Pandharipande, “Scattering of GeV electrons by light nuclei,” Phys. Rev. C **47**, 2218 (1993).
- [38] R. B. Feynstone, “Atomic Mass Table,” <http://ie.lbl.gov/toi2003/MassSearch.asp>.
- [39] H. Meier-Hajduk, C. Hajduk, P. U. Sauer, and W. Theis, “Quasielastic electron scattering from He-3,” Nucl. Phys. A **395**, 332 (1983).
- [40] J. Arrington *et al.*, “Inclusive electron nucleus scattering at large momentum transfer,” Phys. Rev. Lett. **82**, 2056 (1999).

- [41] C. Ciofi degli Atti, E. Pace, and G. Salme, “y scaling, binding effects and the nucleon momentum distribution in He-3,” *Phys. Rev.* **C39**, 259 (1989).
- [42] O. Benhar, D. Day, and I. Sick, “An archive for quasi-elastic electron nucleus scattering data,” (2006), *nucl-ex/0603032*.
- [43] C. Ciofi degli Atti, E. Pace, and G. Salme, “Y scaling analysis of quasielastic electron scattering and nucleon momentum distributions in few body systems, complex nuclei and nuclear matter,” *Phys. Rev.* **C43**, 1155 (1991).
- [44] C. Ciofi degli Atti, E. Pace, and G. Salme, “Asymptotic scaling function and nucleon momentum distribution in few nucleon systems,” *Nucl. Phys.* **A508**, 349 (1990).
- [45] T. De Forest, “Off-shell electron nucleon cross-sections. The impulse approximation,” *Nucl. Phys.* **A392**, 232 (1983).
- [46] E. J. Moniz *et al.*, “Nuclear fermi momenta from quasielastic electron scattering,” *Phys. Rev. Lett.* **26**, 445 (1971).
- [47] T. W. Donnelly and I. Sick, “Superscaling of inclusive electron scattering from nuclei,” *Phys. Rev.* **C60**, 065502 (1999).
- [48] C. Maieron, T. W. Donnelly, and I. Sick, “Extended superscaling of electron scattering from nuclei,” *Phys. Rev.* **C65**, 025502 (2002).

- [49] D. Faralli, C. Ciofi degli Atti, and G. B. West, “Inclusive electron scattering from nuclei: y scaling and final state interactions,” (1999), nucl-th/9910065.
- [50] D. S. Koltun, “Total Binding Energies of Nuclei, and Particle-Removal Experiments,” Phys. Rev. Lett. **28**, 182 (1972).
- [51] C. Itzykson and J. B. Zuber, “Quantum Field Theory,” New York, Usa: McGraw-Hill (1980) 705 P. (International Series In Pure and Applied Physics).
- [52] O. Benhar, V. R. Pandharipande, and I. Sick, “Nuclear binding and deep inelastic scattering,” Phys. Lett. **B410**, 79 (1997).
- [53] P. E. Bosted *et al.*, “Measurements of $\nu W(2)$ and $R = \sigma_l/\sigma_T$ from inelastic electron - aluminum scattering near $x = 1$,” Phys. Rev. **C46**, 2505 (1992).
- [54] O. Nachtmann, “Positivity constraints for anomalous dimensions,” Nucl. Phys. **B63**, 237 (1973).
- [55] O. Benhar and S. Liuti, “Accidental ξ scaling as a signature of nuclear effects at $x > 1$,” Phys. Lett. **B358**, 173 (1995).
- [56] A. D. Martin, R. G. Roberts, W. J. Stirling, and R. S. Thorne, “Uncertainties of predictions from parton distributions. I: Experimental errors.” Eur. Phys. J. **C28**, 455 (2003).
- [57] J. Arrington, private communication (2007).

- [58] E. D. Bloom and F. J. Gilman, “Scaling and the behavior of Nucleon Resonances in Inelastic Electron-Nucleon Scattering,” *Phys. Rev.* **D4**, 2901 (1971).
- [59] J. Arrington, R. Ent, C. E. Keppel, J. Mammei, and I. Niculescu, “Low-Q scaling, duality, and the EMC effect,” *Phys. Rev.* **C73**, 035205 (2006).
- [60] D. Day and I. Sick, “Is simultaneous y and ξ scaling in the quasi-elastic region accidental?” *Phys. Rev.* **C69**, 028501 (2004).
- [61] O. Benhar and S. Liuti, “Can a highly virtual nucleon experience final state interactions in electron nucleus scattering?” *Phys. Lett.* **B389**, 649 (1996).
- [62] O. Benhar, private communication (2007).
- [63] L. L. Frankfurt and M. I. Strikman, “High-Energy Phenomena, Short Range Nuclear Structure and QCD,” *Phys. Rept.* **76**, 215 (1981).
- [64] K. S. Egiyan *et al.*, “Measurement of 2- and 3-Nucleon Short Range Correlation Probabilities in Nuclei,” *Phys. Rev. Lett.* **96**, 082501 (2006).
- [65] C. Yan, R. Carlini, and D. Neuffer, “Beam energy measurement using the Hall C beamline,” Prepared for 1993 IEEE Particle Accelerator Conference (PAC 93), Washington, DC, 17-20 May 1993.
- [66] P. Gueye, “Status of the actual beam position monitors in the Hall C beamline,” Jefferson Lab Hall C Internal Report (unpublished).

- [67] K. Unser, “A toroidal DC beam current transformer with high resolution,” IEEE Trans. Nucl. Sci. **28**, 2344 (1981).
- [68] C. S. Armstrong, “Electroproduction of the S(11) meson (1535) resonance at high momentum transfer,” UMI-99-04269.
- [69] C. Yan and R. Carlini, “Hall C beam line instrumentation,” Given at CEBAF 1992 Summer Workshop, Newport News, VA, 15- 19 Jun 1992.
- [70] C. Yan, N. Sinkine, and R. Wojcik, “Linear beam raster for cryogenic targets,” Nucl. Instrum. Meth. **A539**, 1 (2005).
- [71] D. Meekins, “Hall C Target Configuration,” (2004), unpublished.
- [72] R. Gibbons and D. Nathan, “Thermodynamic Data of Helium 3,” Technical report (1967).
- [73] “Thermophysical Properties of Fluid Systems,” <http://webbook.nist.gov/chemistry/fluid/>.
- [74] “CEBAF Conceptual Design Report,” (1995).
- [75] J. Seely, *Precise Measurement of the Nuclear Dependence of Structure Functions in Light Nuclei*, Ph.D. thesis, Massachusetts Institute of Technology (2006).
- [76] J. Arrington, private communication (2006).
- [77] D. Abbot *et al.*, “Proc. of the IEEE Conference on Real-time Computer Application in Nuclear, Particle, and Plasma Physics, 147,” .

- [78] K. Makino and M. Berz, “COSY INFINITY Version 9,” *Nucl. Instrum. Meth. A* **558**, 346 (2006).
- [79] J. Volmer, “The Pion Charge Form Factor via Pion Electroproduction on the Proton,” (2000).
- [80] *HBOOK: Statistical Analysis and Histogramming* (CERN, Geneva, Switzerland), <http://cern.web.cern.ch/paw>.
- [81] W. R. Leo, *Techniques for nuclear and particle physics experiments* (Springer-Verlag Berlin, 1987).
- [82] V. Tsvaskis, *Longitudinal-Transverse Separation of Deep-Inelastic Scattering at low Q^2 on Nucleons and Nuclei*, Ph.D. thesis, Vrije University (2004).
- [83] S. Stein *et al.*, “Electron scattering at 4 degrees with energies of 4.5 GeV - 20 GeV,” *Phys. Rev. D* **12**, 1884 (1975).
- [84] L. W. Mo and Y.-S. Tsai, “Radiative Corrections to Elastic and Inelastic $e - p$ and $\mu - p$ Scattering,” *Rev. Mod. Phys.* **41**, 205 (1969).
- [85] S. R. Dasu, *Precision Measurement of x , Q^2 , and A-dependence or $R = \sigma_L/\sigma_T$ and F_2 in deep inelastic scattering*, Ph.D. thesis, University of Rochester (1988).
- [86] A. A. Akhundov, D. Y. Bardin, and N. M. Shumeiko, “Electromagnetic corrections to the deep inelastic $\mu - p$ scattering at high energies,” *Sov. J. Nucl. Phys.* **26**, 660 (1977).

- [87] K. S. Kim, L. E. Wright, Y. Jin, and D. W. Kosik, “Approximate treatment of electron Coulomb distortion in quasielastic (e,e') reactions,” *Phys. Rev.* **C54**, 2515 (1996).
- [88] A. Aste, C. von Arx, and D. Trautmann, “Coulomb distortion of relativistic electrons in the nuclear electrostatic field,” *Eur. Phys. J.* **A26**, 167 (2005).
- [89] D. C. Morton, Q. Wu, and G. W. F. Drake, “Nuclear charge radius for ${}^3\text{He}$,” *Physical Review A (Atomic, Molecular, and Optical Physics)* **73**, 034502 (2006).
- [90] A. Aste, private communication (2006).
- [91] C. Ciofi degli Atti and G. B. West, “Old and new facets of y-scaling: The universal features of nuclear structure functions and nucleon momentum distributions,” (1997), *nucl-th/9702009*.
- [92] P. Bosted, private communication (2006).
- [93] O. Benhar *et al.*, “Scattering of GeV electrons by nuclear matter,” *Phys. Rev.* **C44**, 2328 (1991).
- [94] O. Benhar, A. Fabrocini, S. Fantoni, and I. Sick, “Spectral function of finite nuclei and scattering of GeV electrons,” *Nucl. Phys.* **A579**, 493 (1994).
- [95] A. N. Antonov, M. K. Gaidarov, M. V. Ivanov, D. N. Kadrev, and P. E. Hodgson, “Nucleon momentum distribution in deuteron and other nuclei within light-front dynamics method,” *Phys. Rev.* **C65**, 024306 (2002).

- [96] A. Antonov, private communication (2007).
- [97] K. S. Egiyan *et al.*, “Observation of Nuclear Scaling in the $A(e, e')$ Reaction at $x_B > 1$,” Phys. Rev. **C68**, 014313 (2003).
- [98] J. Arrington and D. Day, “Inclusive Scattering from Nuclei at $x > 1$ in the quasielastic and deeply inelastic regimes,” (2006), Jefferson Lab Proposal/E12-06-105.